國 立 交 通 大 學

材料科學與工程研究所

博 士 論 文

有機材料及無機奈米粒子之氫鍵超分子作用

於光電材料之應用

H-Bonded Supramolecular Interactions of Organic Materials and Inorganic Nanoparticles for Applications of Electro-Optical Materials

研 究 生：方曉萍
指導教授：林宏洲 博士

中華民國一ｏ二年 一 月

有機材料及無機奈米粒子之氫鍵超分子作用

於光電材料之應用

H-Bonded Supramolecular Interactions of Organic Materials and Inorganic Nanoparticles for Applications of Electro-Optical Materials

研 究 生 ： 方曉萍　　Student: Hsiao-Ping Fang

指導教授 ： 林宏洲　　Advisor: Prof. Hong-Cheu Lin

國立交通大學

材料科學與工程學系

博士論文

A Thesis
Submitted to Department of Materials Science and Engineering
College of Engineering
National Chiao Tung University
In Partial Fulfillment of the Requirement
for the Degree of Doctor of Philosophy of Science
In Materials Science and Engineering
January 2013
Hsinchu, Taiwan

中華民國一ｏ二年 一月

H-Bonded Supramolecular Interactions of Organic Materials and Inorganic Nanoparticles for Applications of Electro-Optical Materials

Student: Hsiao-Ping Fang Advisor: Prof. Hong-Cheu Lin

Department of Materials Science and Engineering National Chiao Tung University

Abstract

First, Two kinds of novel conjugated polymers containing 2,7-carbazole, thiophene, and fused-dithienothiophene rings as backbones bearing acid-protected and benzoic acid pendants (**PCA** and **PCB**, respectively) were utilized for organic solar cell applications. The absorption spectra of these polymers (in both solutions and solid films) showed an absorption range at 300–580 nm. Furthermore, ZnO nanoparticles were synthesized and surface-modified with pyridyl surfactants (**ZnOpy**) to be ca. 3–4 nm. The pyridyl surfactants of **ZnOpy** nanoparticles (as electron acceptors to partially replace expensive electron acceptor PCBM) not only induce supramolecular interactions with benzoic acid pendants of polymer **PCB** via H-bonds, but also enhance the homogeneous dispersions of **ZnOpy** nanoparticles in polymer **PCB**. Thus, the ternary systems of **PCA**,**PCB**/**ZnOpy**/PCBM in weight ratios of 1:0.05:1 and 1:0.1:1 were investigated in bulk heterojunction polymer solar cells (PSCs). Under the

standard illumination of AM 1.5, 100 mW/cm^2, the best power conversion efficiency (PCE) of the PSC cell containing a polymer blend of **PCB**/**ZnOpy**/PCBM=1:0.05:1 reached PCE=0.55%, with J_{sc}=2.11 mA/cm^2, V_{oc}=0.88 V, and FF=29.4%.

Second, Three kinds of dithienothiophene/carbazole-based conjugated polymers (**PCA**, **PCB**, **PCC**), which bear acid-protected and benzoic acid pendants in **PCA** and **PCB**, respectively, were synthesized via Suzuki coupling reaction. Interestingly, **PCA**, **PCB**, and **PCC** exhibited reversible electrochromism during the oxidation processes of cyclic voltammogram studies, and **PCB** (with H-bonds) revealed the best electrochromic property with the most noticeable color change. According to powder X-ray diffraction (XRD) analysis, these polymers exhibited obvious diffraction features indicating bilayered packings between polymer backbones and π - π stacking between layers in the solid state. Compared with the XRD data of **PCA** (without H-bands), H-bonds of **PCB** induced a higher crystallinity in the small-angle region (corresponding to a higher ordered bilayered packings between polymer backbones), but with a similar crystallinity in the wide angle region indicating a comparable π - π stacking distance between layers. Moreover, based on the preliminary photovoltaic properties of PSC devices (**PCA**, **PCB**, and **PCC** blended individually with PCBM acceptor in the weight ratio of 1:1), **PCB** (with H-bonds) possessed the highest power conversion efficiency of 0.61% (with J_{sc} = 2.26 mA/cm^2, FF = 29.8%, and V_{oc} = 0.9 V). In contrast to **PCA** (without H-bands), the thermal stability, crystallinity, and electrochromic along with photovoltaic properties of **PCB** were generally enhanced due to its H-bonded effects.

Third, Four novel metallo-polymers (**P1-P4**) containing aryl-imidazo-phenanthrolines (AIP) ligands (incorporated with phenyl and fused-thiophene cores) were synthesized and characterized. Interestingly, **P1-P4** exhibited electrochromism during the

oxidation processes of cyclic voltammogram studies. In addition, **P1**-**P4** were blended with surface-modified pyridyl-ZnO nanoparticles (**ZnOpy** as proton acceptors) to form nanocomposites, where **P3**-**P4** were functionalized with carboxylic acid pendants (as proton donors) on the polymer backbones to study for the H-bonded effects on surface-modified **ZnOpy** nanoparticles. In order to investigate the nanocomposites containing metallo-polymers **P1**-**P4** and surface-modified **ZnOpy** nanoparticles, nanocomposites **P1**-**P4**/**ZnOpy** were characterized by UV-visible (UV) absorption spectra, Fourier transform infrared (FTIR), photoluminescence (PL) spectra, time-resolved photoluminescence decays, X-ray diffraction (XRD) measurements, and transmission electron microscopy (TEM) analyses. In contrast to nanocomposites **P1**/**ZnOpy** and **P2**/**ZnOpy**, higher crystallinities with a distinct layered-structure of H-bonded nanocomposites **P3**/**ZnOpy** and **P4**/**ZnOpy** in XRD measurements were induced by the introduction of surface-modified **ZnOpy** nanoparticles to metallo-polymers **P3** and **P4**, correspondingly. Furthermore, due to the supramolecular interactions of surface-modified **ZnOpy** nanoparticles with metallo-polymers **P3**-**P4**, TEM images verified that **ZnOpy** nanoparticles were more homogeneously distributed in nanocomposites **P3**-**P4**/**ZnOpy** (with H-bonds) than those in **P1**-**P2**/**ZnOpy** (without H-bonds), respectively.

Finally, In this study we synthesized three metal-free organic dyes (**Cpd11**, **Cpd16**, and **Cpd22**) featuring 3,4,5-tris(dodecyloxy)phenyl and cyanoacrylic acid moieties as electron-donor and electron-acceptor/anchoring units, respectively, linked through various dithienothiophenyl conjugated spacers. **Cpd16** exhibits mesomorphic properties, confirmed through polarizing optical microscopy, differential scanning calorimetry, and X-ray diffraction (XRD), due to the appropriate ratio of the lengths of its flexible chain to its rigid core. Molecular modeling of **Cpd16**, and its *d*-spacing

determined from XRD data, verified the existence of a tilt angle in the SmC phase. Among these metal-free organic dyes, a dye-sensitized solar cell incorporating **Cpd16** exhibited the best performance, presumably because of its better packing and its mesomorphic properties; the power conversion efficiency was 3.72% (V_{oc} = 0.58 V; J_{sc} = 9.98 mA cm^{-2}; FF = 0.65) under simulated AM 1.5 irradiation (100 mW cm^{-2}).

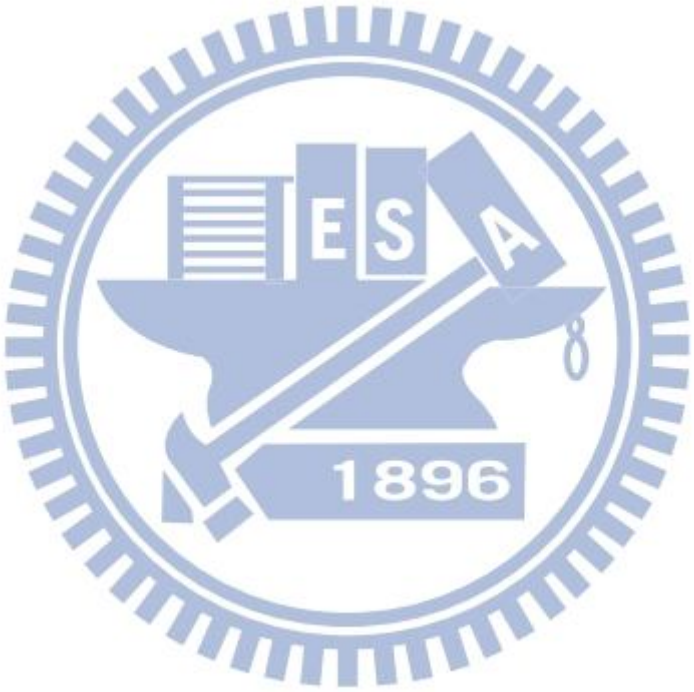

摘 要

本論文研究方向為探討一系列包含有機材料及無機奈米粒子之氫鍵超分子作用在有機光電材料為研究主軸。

第一部分，兩種主鏈包含 2,7-carbazole 和 fused-dithienothiophene 環的共軛高分子在側邊懸掛 acid-protected 和 benzoic acid 官能基（**PCA** 和 **PCB**），此系列高分子的吸收範圍約在 300 nm-580 nm， 以作為太陽能電池的應用。此外也合成氧化鋅奈米粒子，和表面改質含有吡啶官能基(**ZnOpy**)，大小約 3-4 奈米。**ZnOpy** 奈米粒子當電子接受者取代部分 PCBM，不但透過氫鍵與高分子 **PCB** 的 benzoic acid 產生超分子作用力，而且增加 **ZnOpy** 奈米粒子在高分子 **PCB** 均勻的分散性。因此，在複合系統中， **PCB**/ **ZnOpy**/**PCBM** 在重量 1:0.05:1 混摻時，在 AM 1.5 的標準太陽光照射下，最佳元件效率可達到 0.55%，J_{sc}=2.11 mA/cm^2，V_{oc}=0.88 V，FF=29.4 %。

第二部分，我們利用 Suzuki coupling reaction 合成了以 2,7-carbazole 及 fused dithienothiophene 單元為分子主鏈的共軛型高分子(**PCA**, **PCB**, 和 **PCC** ），此系列高分子的吸收範圍約在 300 nm-550 nm。其中 **PCB** 主鏈側邊修飾有酸的保護基, 而 **PCB** 的主鏈側邊修飾有酸的官能基, 相互作為研究氫鍵效應的對照組, 而且 **PCA**, **PCB**, 和 **PCC** 在電化學實驗氧化過程中有電致變色的性質，**PCB** 有明顯的顏色變化(由橘變黑)， X 光繞射光譜儀(XRD)也可觀察到 **PCB** 的氫鍵結構有較高的結晶度，在小角度繞射區段可觀察到高分子主鏈層的層間距。且當與 PCBM 重量比 1：1 混摻時，在 AM 1.5 的標準太陽光照射下，最佳元件效率可達到 0.61%，J_{sc}= 2.26 mA/cm^2，V_{oc}=0.9 V，FF=29.8%。相較於高分子 **PCA** 無氫鍵形成， **PCB** 含有氫鍵結構其熱穩定性，結晶度，電致變色及太陽能電池轉化效率都因為 **PCB** 含有氫鍵結構而提高其性質。

第三部分, 合成鑑定四個高分子(**P1-P4**)包含aryl-imidazo-phenanthrolines (AIP) 敖合基，其中修飾含有phenyl 和 fused-thiophene。高分子(**P1-P4**)在電化學氧化過程中顯示有電致變色的性質，另外，四個高分子(**P1-P4**) ，其中**P3-P4**高分子側邊修飾含有carboxylic acid的官能基和表面改質吡啶的氧化鋅奈米粒子混摻以

形成奈米複合材料加以討論氫鍵效應。利用紫外光光譜儀(UV），螢光光譜儀(PL)， 時間解析光激螢光光譜儀(TRPL)， X光繞射光譜儀(XRD)， 穿透式電子顯微鏡(TEM)加以分析氫鍵的效應。**P3**/**ZnOpy**, **P4**/**ZnOpy** 奈米複合材料因為氫鍵結構顯示有較高的結晶度，此外，由於氧化鋅和高分子的超分子作用力，從TEM圖可得知含有氫鍵的奈米複合材料(**P3**/**ZnOpy**, **P4**/**ZnOpy**)其分散性較好。

最後一個部份，本研究中擬開發新的非金屬系(metal-free)有機光敏化染料，所設計的染料分子是以 tris-dodecyloxyphenyl-與 cyanoacrylic acid 為電子予體與受體，而主要是合成修飾不同的電子予體或電子予體與電子受體間之共軛橋樑(conjugated spacer)。在共軛橋樑設計上，主結構是以 dithieno[3,3-b:2',3'-d] thiophene，其中再分別含有 dithiophene 以及 bithiazole 來延長共軛系統長度，以提升電荷轉移的能力和加強吸收光譜的強度和範圍。由於含有液晶性質的分子，具有較良好的分子排列性，藉由引入一般運用在液晶上的片段液晶分子結構 trioxyphenyl-，加上共平面性較好的融合環 dithieno[3,3-b:2',3'-d] thiophene，來探討所設計的分子在染料敏化型太陽能電池上的應用與特性。其中所設計的染料分子化合物 **16** 其光轉換效率為 3.72% (V_{oc}= 0.58V, J_{sc}=9.98 mA/cm^2, FF =0.65)，在相同條件下，已可達 N719 效率(7.04%)的 53%，雖然效率不及以往文獻 triarylamine 為電子予體的效率，但成功的開發出新一系列不同於以往的電子予體染料分子，未來可在分子的設計上，對於電子予體上做取代基的轉換，以利於光轉換效率的提升。

ACKNOWLEDGEMENTS

本論文首先感謝林宏洲老師這些年來對我的照顧及鼓勵，老師對於研究上的辛苦用心及待人處世的教導，使我一路成長，如今順利完成博士學業，老師指導的恩惠，學生將永記於心。感謝韋光華老師、韓建中老師、林建村老師、徐新光、許千樹老師於百忙之中審核論文並給予寶貴的建議及指正。

博士班近五年半的時光使我獲益良多，很幸運也很快樂地在這實驗室度過這些日子，在此特別感謝實驗室的學長們在實驗上的教導與幫助，並感謝實驗室的眾多的同學及學弟妹在實驗上的協助，使我的實驗得以順利完成，還有張立實驗室、呂志鵬實驗室以及許許多多材料所的學長、同學、學弟妹們在這些日子的陪伴，使我的交大生活更增添的許多歡樂。謝謝所有真心愛我、支持我的人，我會努力成為更好的人，以達謝大家對我的支持與愛護。

最後要特別由衷地感謝一直栽培我的父母親、支持我的老公、妹妹、弟弟和所有家人，謝謝你們一路上的支持與鼓勵，讓我能在無後顧之憂下求學並完成博士學位。

Table of Contents

Table Lists

Figure Lists

Chapter 1

Introduction

The need to develop inexpensive renewable energy sources stimulates scientific research for efficient, low-cost photovoltaic devices. The organic polymer-based photovoltaic elements have introduced at least the potential of obtaining cheap and easy methods to produce energy from light. The possibility of chemically manipulating the material properties of polymers (plastics) combined with a variety of easy and cheap processing techniques has made polymer-based materials present in almost every aspect of modern society. Organic semiconductors have several advantages: (a) low cost synthesis, and (b) easy manufacture of thin film devices by vacuum evaporation/sublimation or solution cast or printing technologies.[1]

1.1 Polymeric Solar Cells (PSCs)

Novel materials are developed for organic optoelectronic devices, such as polymeric solar cells (PSCs), which is a popular research topic in recent decades, because they are low cost and green materials for sustainable resources to reduce consumptions of fossil energy and nuclear power.[2] In particularly, bulk heterojunction (BHJ) solar cells consisting of electron-donating conjugated polymers blended with electron-accepting fullerenes are fabricated in solid thin

films.[3] Up to now, regio-regular poly[2-methoxy-5-(3',7'-dimethyloctyloxy)-p-phenylenevinylene] (MDMO-PPV)[4] and poly(3-hexylthiophene) (P3HT)[5] as electron donors blended with [6,6]-phenyl-C61-butyric acid methyl ester (PCBM) as an electron acceptor approached high power conversion efficiency (PCE) values of 5.0% in PSCs. More recently, the PCE values of BHJ solar cells using new low-band gap conjugated polymers have reached 6 to 8%.[6,7] The PCE values of BHJ solar cells were affected by, for example, the energy band gaps of polymers, which is related to the chemical structure of the conjugated polymers.

1.2 Hybrid Polymer-Inorganic Solar Cells

These hybrid polymer-inorganic solar cells utilize the high electron mobility of the inorganic phase to overcome charge-transport limitations associatedwith organic materials. The efficient BHJ solar cells made of ZnO nanoparticles and a conjugated polymer have been reported previously.[8] The ZnO nanoparticles were blended with poly[2-methoxy-5-(3′,7′-dimethyloctyloxy)-p-phenylenevinylene] (MDMOPPV) to possess a highest power conversion efficiency (PCE) approaching 1.6% in PSCs.[9] Hybrid solar cells based on CdSe nanoparticles and a PPV-type polymer containing fluorene and thiophene units (PFT) were investigated. The CdSe/PFT devices showed

very low photocurrent and fill factor values, which were attributed to the poor charge transport in the trioctylphosphine oxide (TOPO)-capped CdSe nanoparticle phase. Thus, ternary systems based on mixtures of PFT/CdSe and the fullerene derivative [6,6]-phenyl C61 butyric acid methyl ester (PCBM) were investigated. It was observed that for the optimized composition of 20 wt.% PFT+40 wt.% CdSe+40 wt.% PCBM the devices presented higher photocurrents and efficiencies.(Figure 1.2.1) The use of inorganic nanoparticles, such as TiO_2, ZnO, $CuInS_2$, PbSe, CdSe, and CdTe, have some advantages, related to the versatility of these materials, which often can be easily synthesized in a great variety of sizes and shapes, according to the desired properties.[10]

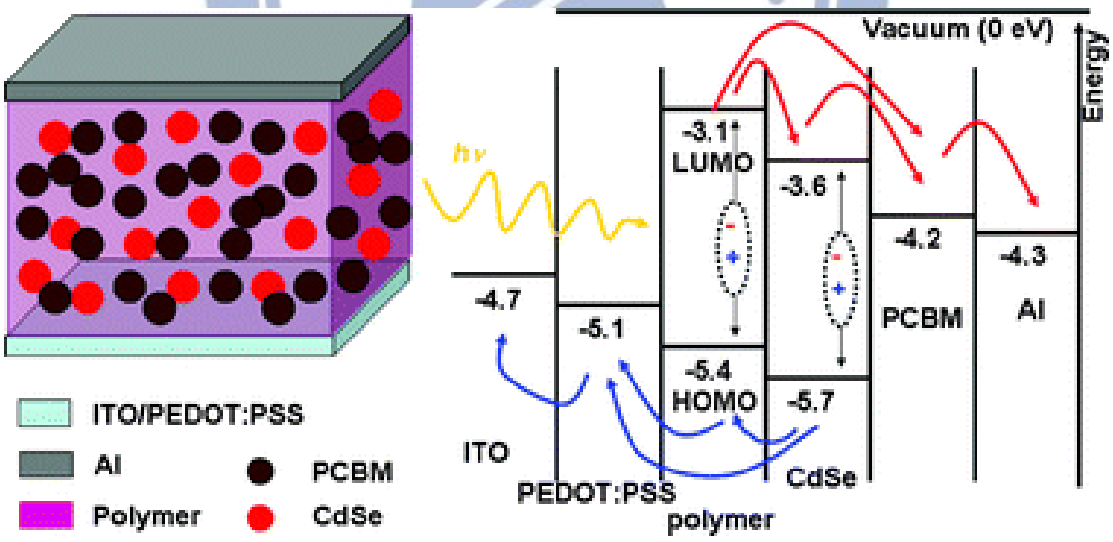

Figure 1.2.1 The energy levels of in the ternary system solar cell showing the HOMO and LUMO levels of the materials and work function of the electrodes. The arrows indicate the expected charge transfer and charge transport processes.

1.3 Supramolecular H-bond Polymers for Organic Solar Cells

Nanostructured materials with tailor-made properties and functions can be developed by exploiting the supramolecular approach through molecular recognition. In fact, the hierarchical self-assembly of multivalent molecular modules through the concerted action of multiple noncovalent interactions represents a very powerful approach as it makes possible the simultaneous organization of various molecular systems into intrinsically defect-free 2D architecture featuring a long-range order.[11]

Hydrogen bonds (H-bonds) are ideal noncovalent interactions to form self-assembled architectures due to their selectivity and directionality. A numerous advantages of H-bonded polymers, such as stronger light absorptions, lower HOMO levels, higher V_{oc} values, higher hole mobilities, and higher crystallinities, were utilized for organic solar cells.[12] Therefore, great efforts have been taken toward the preparation and characterization of photo- and electroactive noncovalent assemblies based on hydrogen bonds (H-bonds). Wurthner,[12(a,b)] El-ghayoury et al., and Jonkheijm et al.[12(c,d)] reported H-bonded assemblies of perylene bisimide and melamine derivatives. In addition, El-ghayoury et al. reported a PCE value of 0.39% for PSCs by utilizing a H-bonded polymer containing oligo(p-phenylene vinyene) and ureido-pyrimidinone units.[12(c)] Because of several advantages in polymers, including low cost, easy processing, and tunable chemical properties, the conjugated polymers consisting of different heteroaromatic rings, such as thiophene and carbazole, exhibit an

electrochromic behavior as well as photovoltaic properties.

Moreover, connecting the electrooptical properties in organic devices have been established through the supramolecular interactions, e.g. H-bonds, in organic, dendritic, and polymeric H-bonded complex systems. This was illustrated by a recent report on a triple hydrogen-bonded triad consisting of a central perylene that was connected to two C_{60} chromophores (Figure 1.3.1).[13]

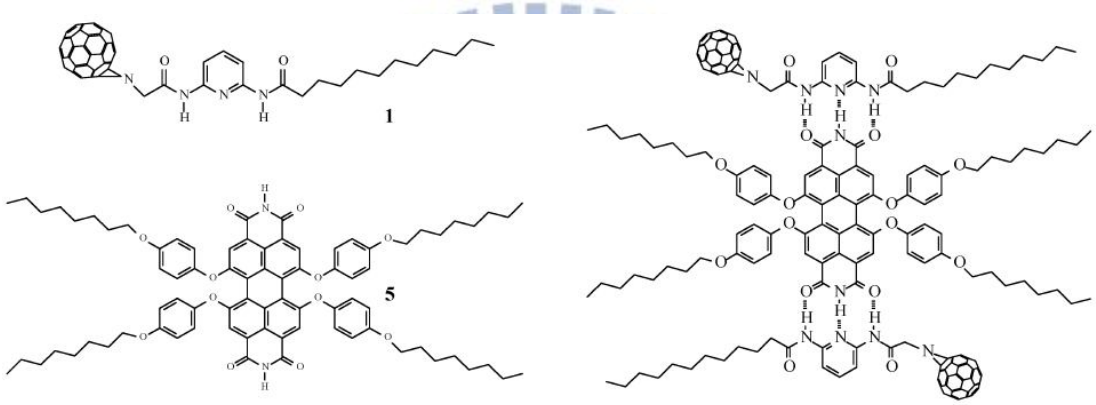

Figure 1.3.1 Superstructure of self-assembly of [60]fullerene derivative **1** with perylene bisimide **5** by H-bonding.

1.4 Dye-Sensitized Solar Cells (DSSCs)[14]

Dye-sensitized solar cells (DSSC) have attracted considerable attention in recent years as they offer the possibility of low-cost conversion of photovoltaic energy. In this context, dye-sensitized solar cells (DSSC) have attracted considerable attention in recent years. Efforts in the synthesis of sensitizers for DSSCs can be grouped into two broad areas: 1) Functional ruthenium(II)–polypyridyl complexes such as N3,[15] N719, Z907, and black dye; and 2) metal-free organic donor–acceptor (D–A) dyes. The

former class of compounds contains expensive ruthenium metal and requires careful synthesis and tricky purification steps. On the other hand, the second class can be prepared rather inexpensively by following established design strategies. Conventional DSSCs typically contain five components: 1) a photoanode, 2) a mesoporous semiconductor metal oxide film, 3) a sensitizer (dye), 4) an electrolyte/hole transporter, and 5) a counter electrode. In DSSCs, the incoming light is absorbed by the sensitizer, which is anchored to the surface of semiconducting TiO_2 nanocrystals. Charge separation takes place at the interface through photoinduced electron injection from the excited dye into the conduction band of the TiO_2. Holes are created at the dye ground state, which is further regenerated through reduction by the hole-transport material (HTM), which itself is regenerated at the counterelectrode by electrons through an external circuit. In principle, for efficient DSSCs the regeneration of the sensitizer by a hole transporter should be much faster than the recombination of the conduction band electrons with the oxidized sensitizer. Additionally, the highest occupied molecular orbital (HOMO) of the dye should lie below the energy level of the hole transporter, so that the oxidized dyes formed after electron injection into the conduction band of TiO_2 can be effectively regenerated by accepting electrons from the HTM. The general operating principle of a dye-sensitized solar cell is depicted in Figure 1.4.1. The research area dealing with

DSSCs is expanding very rapidly and attracting scientist from different disciplines: 1) Chemists to design and synthesize suitable donor–acceptor dyes and study structure–property relationships; 2) physicists to build solar cell devices with the novel materials, to characterize and optimize their performances, and to understand the fundamental photophysical processes; and 3) engineers to develop new device architectures. The synergy between all the disciplines will play a major role for future advancements in this area.

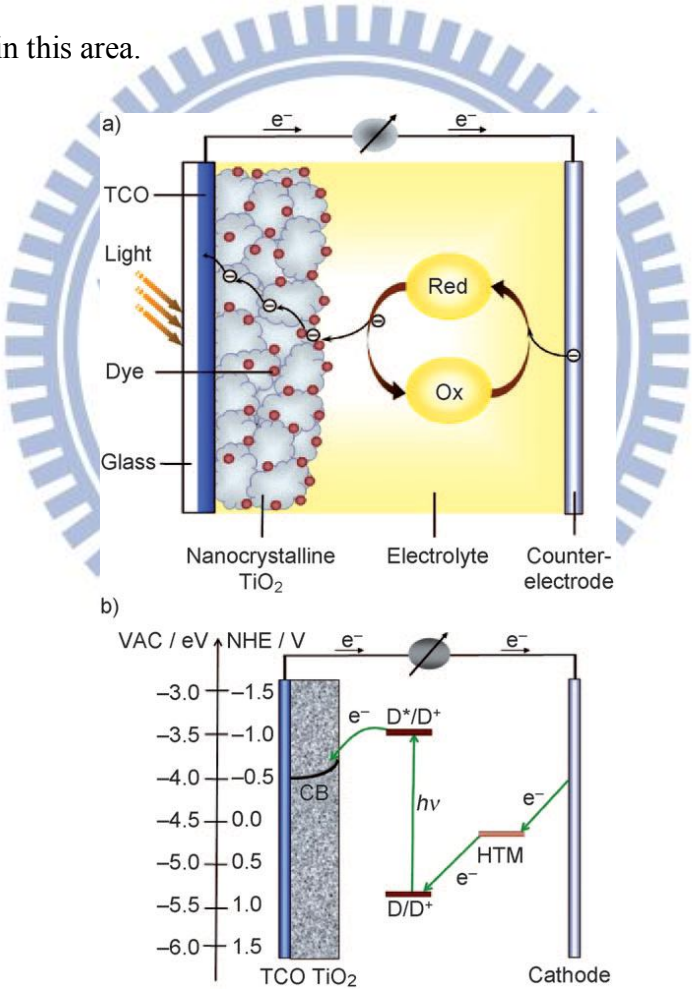

Figure 1.4.1 a) Fundamental processes in a dye-sensitized solar cell. b) Energy-level diagram of a DSSC. TCO=transparent conducting oxide.[14]

1.4.1 Metal-Free Organic Dyes in DSSCs

The development of novel materials for use in organic optoelectronic devices, such as dye-sensitized solar cells (DSSCs),[16] has become a popular research topic in the quest for low-cost, green materials for sustainable use and a decrease in demand for fossil fuels and nuclear power. DSSCs based on Ru-photosensitizers,[17-18] such as cis-bis(isothiocyanato)bis(2,2′-bipyridyl-4,4′-dicarboxylato)-ruthenium(II) (N3)[15]and related derivatives, have been applied very successfully with high power conversion efficiencies (PCEs) of 9–12%.[15,19-23] Recently, it has been demonstrated that DSSCs can also be constructed from metal-free organic dyes.[14] Because of the high cost of rare Ru metal and the relatively low molar extinction coefficients and tedious purification of Ru-photosensitizes,[19] metal-free organic sensitizers have become increasingly attractive and widely developed.[24,25] Nevertheless, the ability to reach higher efficiencies when using metal-free organic dyes remains a challenge, although great progress has been made in this field.[26-29] The key characteristics for a dye to be used in a DSSC are high absorption over a wide range of the solar spectrum with high molar extinction coefficients, efficient charge separation, redox stability, andsuitable functional groups to interact with the electron sink (TiO_2). Metal-free organic dyes featuring a donor/acceptor structural design were synthesized have particularly wide absorption ranges for DSSC applications.[24-32]

Some general principles to construct an efficient dye and efficient DSSCs are as follows: 1) The absorption range of the dye should cover the whole visible and some of the near-infrared region, and its molar extinction coefficient must be as high as possible to enable efficient light harvesting with thinner TiO_2 layers (panchromatic absorption). 2) For efficient electron injection into the anode, the lowest unoccupied molecular orbital (LUMO) of the dye should be localized near the anchoring group (usually a carboxylic or phosphonic acid) and above the conduction band edge of the semiconductor electrode (typically TiO_2). 3) The HOMO of the dye should lie below the energy level of the redox mediator to allow efficient regeneration of the oxidized dye. 4) To minimize charge recombination between the injected electrons and the resulting oxidized dye, the positive charge resulting after electron injection should be localized on the donor part, which is further away from the TiO_2 surface. 5) The periphery of the dye should be hydrophobic to minimize direct contact between the electrolyte and the anode to prevent water-induced desorption of the dye from the TiO_2 surface and consequently enhance the longterm stability. 6) The dye should not aggregate on the surface to avoid nonradiative decay of the excited state to the ground state, which often occurs with thicker films.

1.5 Metalloplymer[33]

The rapid growth of supramolecular chemistry since the 1970s has led to many new opportunities to take advantage of reversible interactions. A major contribution to the diversity of the field of metal-containing polymers has involved the development of metallosupramolecular polymers, in which the metal ions are bound by non-covalent coordination interactions that allow for reversible, 'dynamic', binding analogous to hydrogen bonding (figure panel b).[34-35] The recent developments are illustrated by the formation of metallosupramolecular polymers that involve labile multidentate ligation and metallophilic interactions. As another key contributor to structural diversity, metal containing polymers can contain a variety of metal centres, from transition-metal ions and main-group metals through to lanthanides and actinides. In addition, the metal centres can be located either in the polymer main chain or in the side-chain structure (figure panels c and d) (Figure 1.5.1). As examples of further subdivisions, metallopolymers can be linear, star-shaped, highly branched or dendritic[36-42] (figure panels e, f and g) (Figure 1.5.1). Significantly, with all of these materials the typical classical polymer processing possibilities, such as spin coating, inkjet printing, extrusion, compounding and film blowing, are maintained.

Metal-ligand coordination seems to be particularly attractive in past few decades because of searching for new smart materials.[40-42] In recent years, the researches on

supramolecular metallo-polymers applied to electro-optical materials have been commonly conducted, because the advantages of these materials, such as easy processability, cheap fabrication, rapid coordination, and tunability of the optical band gap, can promote long-range electrons or energy transfers.[43] Supramolecular metallo-architecture is formed with coordination ability of transition metal ions and chelating ligands because of their self-recognition and self-assembly.[44-46] Moreover, metal-ligand complexes realized ideal conditions from self-assembly to form the kinetically labile but nevertheless thermodynamically stable bonds.[47] In the meanwhile, metallo-polymers are also good candidates to study for their electrochromic properties during the redox processes.[48-49] 2,2':6',2''-Terpyridine(terpy) and bipyrdine (bpy) derivatives have been utilized recently for multinuclear supramolecular interactions.[50-52] The transport of energy and electrons within nanoscale ordered materials is significant to optoelectronics. It needs to control over both of their physical and chemical properties in the self-assembled organization.

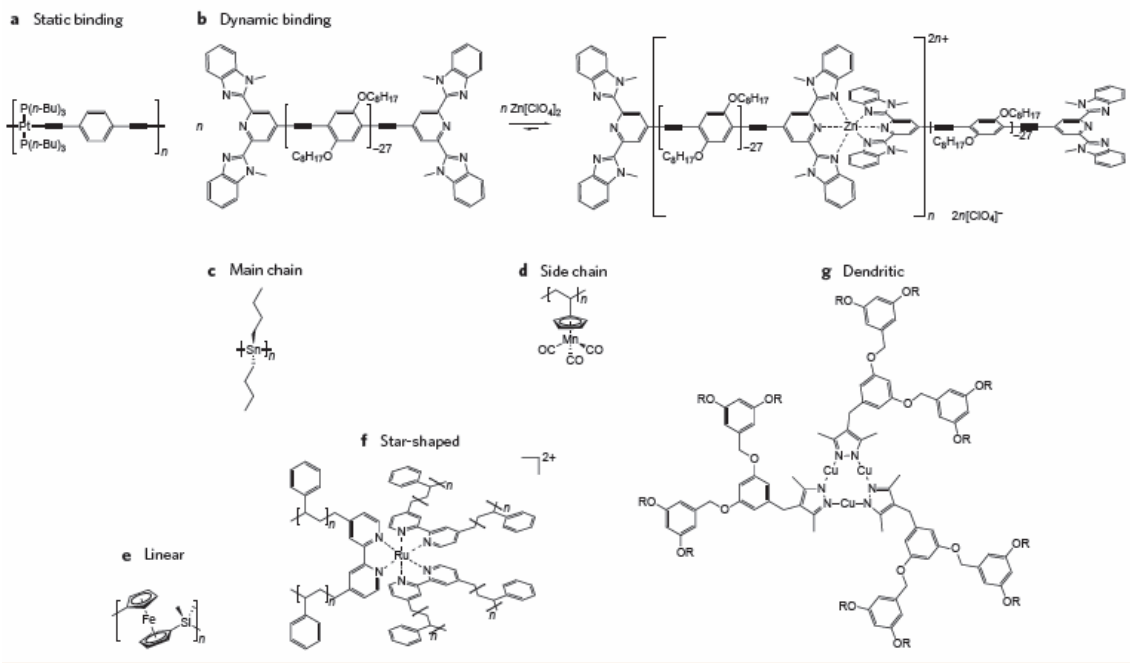

Figure 1.5.1 Structural diversity of metal-containing polymers.

1.5.1 Nanocomposite Systems Base on Metallopolymer and Nanoparticles

Nanocomposite systems are that combine the favorable features of, for example, fullerenes and porphyrins as electron acceptors and donors, respectively.[49] They have received interest in the areas of light-induced electron-transfer chemistry and solar energy conversion.[53] Common electron donor-acceptor systems are based on covalent linkages. However, much less is, known about noncovalent electron donor-acceptor nanocomposites and the function of the intervening spacers.[54] Compared with other intermolecular forces, such as van der Waals, π-π stacking, or Coulombic interactions, hydrogen bonds are particularly attractive as they are directional and do not possess electronic energy levels that interfere with those in materials for organic electro-optical applications.[55-56] Therefore, that great efforts have been expended toward the preparation and characterization of photo- and electro-active noncovalent assemblies based on hydrogen bonds (H-bonds). (Figure 1.5.2)

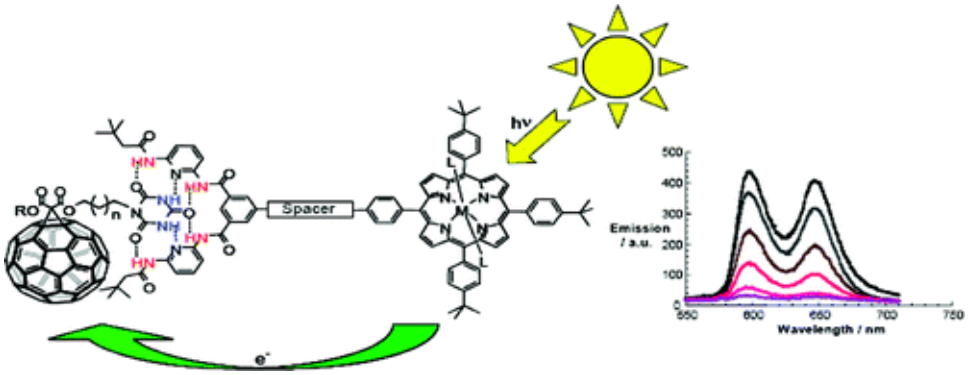

Figure 1.5.2 Characterization of photo- and electro-active noncovalent assemblies based on hydrogen bond.

Chapter 2

Applications of novel dithienothiophene- and 2,7-carbazole-based conjugated polymers with surface-modified ZnO nanoparticles for organic photovoltaic cells

*Two kinds of novel conjugated polymers containing 2,7-carbazole, thiophene, and fused-dithienothiophene rings as backbones bearing acid-protected and benzoic acid pendants (**PCA** and **PCB**, respectively) were utilized for organic solar cell applications. The absorption spectra of these polymers (in both solutions and solid films) showed an absorption range at 300 – 580 nm. Furthermore, ZnO nanoparticles were synthesized and surface-modified with pyridyl surfactants (**ZnOpy**) to be ca. 3 – 4 nm. The pyridyl surfactants of **ZnOpy** nanoparticles (as electron acceptors to partially replace expensive electron acceptor PCBM) not only induce supramolecular interactions with benzoic acid pendants of polymer **PCB** via H-bonds, but also enhance the homogeneous dispersions of **ZnOpy** nanoparticles in polymer **PCB**. Thus, the ternary systems of **PCA**,**PCB**/**ZnOpy**/PCBM in weight ratios of 1:0.05:1 and 1:0.1:1 were investigated in bulk heterojunction polymer solar cells (PSCs). Under the standard illumination of AM 1.5, 100 mW/cm^2, the best power conversion efficiency (PCE) of the PSC cell containing a polymer blend of*

PCB/ZnOpy*/PCBM=1:0.05:1 reached PCE=0.55%, with Jsc=2.11 mA/cm*^{2}*, Voc=0.88 V, and FF=29.4%.*

2.1 Introduction

The developments of new materials to be used in organic optoelectronic devices such as polymeric solar cells (PSCs) have become dramatically attractive because they represent a green and renewable energy alternative to fossil energy and nuclear power. In particular, the so-called bulk heterojunction (BHJ) concept[2] has been established in thin films of organic solar cell devices utilizing electron-donating conjugated polymers blended with electron-accepting species, such as fullerenes,[3] dicyano-based polymers,[4,57] or n-type nanoparticles.[58] These hybrid polymer-inorganic solar cells utilize the high electron mobility of the inorganic phase to overcome charge-transport limitations associated with organic materials. The efficient BHJ solar cells made of ZnO nanoparticles and a conjugated polymer have been reported previously.[8] The ZnO nanoparticles were blended with poly[2-methoxy-5-(3′,7′-dimethyloctyloxy)-p-phenylenevinylene] (MDMOPPV) to possess a highest power conversion efficiency (PCE) approaching 1.6% in PSCs.[9] Hybrid solar cells based on CdSe nanoparticles and a PPV-type polymer containing fluorene and thiophene units (PFT) were investigated. The CdSe/PFT devices showed very low photocurrent and fill factor values, which were attributed to the poor charge transport

in the trioctylphosphine oxide (TOPO)-capped CdSe nanoparticle phase. Thus, ternary systems based on mixtures of PFT/CdSe and the fullerene derivative [6,6]-phenyl C61 butyric acid methyl ester (PCBM) were investigated. It was observed that for the optimized composition of 20 wt.% PFT+40 wt.% CdSe+40 wt.% PCBM the devices presented higher photocurrents and efficiencies. The use of inorganic nanoparticles, such as TiO_2, ZnO, $CuInS_2$, PbSe, CdSe, and CdTe, have some advantages, related to the versatility of these materials, which often can be easily synthesized in a great variety of sizes and shapes, according to the desired properties.[10] In parallel, oligo- and poly(2,7-carbazole)[61] derivatives have been successfully used in polymer light emitting diodes (PLEDs)[62] and organic field-effect transistors (OFETs)[62-63], demonstrating good p-type transport properties.[60] Recently, Müllen and co-workers[61] have reported solar cells consisting of poly(N-alkyl-2,7-carbazole)with a PCE value of 0.6%. Moreover, in contrast to the fluorene unit the carbazole moiety is fully aromatic, providing a better chemical and environmental stability. Taking all of these results into account, the development of new copolymers based on carbazoles should therefore lead to interesting features for photovoltaic applications. A class of polymers that have to date received little attention as p-type materials for use in solar cells is polycarbazoles. Carbazole is a well-known electron-donating unit, and thus poly(2,7-carbazole)s are attractive

candidates as p-type materials for solar cells.[64] Dithieno[3,2-b:2′,3′-d]thiophene (DTT) is a sulfur rich (three-S atoms) and electron rich segment, and serves as an important building block of a wide variety of materials for electronic and optical applications, such as electroluminescence, two photon absorptions, nonlinear optics, photochromism, OFETs, and OPVs.[65] Besides, the fused aromatic rings can make the polymer backbones more rigid and coplanar, therefore enhancing effective π-conjugation lengths, lowering band gaps, and extending absorption lengths. Powder X-ray diffraction (XRD) analyses suggested that these copolymers formed self-assembled π–π stacking and pseudo-bilayered structures.[66] Molecules containing fused ring systems intend to maximize the π-orbital overlaps by restricting intramolecular rotation in these systems and possibly to induce face-to-face π–π stackings, facilitating intermolecular hoppings and charge transports.[65] In order to increase the solubility in poly(DTT) without causing any additional twisting of the repeating units in the resulting polymers, alkylsubstituted thiophene units were incorporated into the polymer backbones as copolymers to fabricate OPVs[12] and OFETs.[67] Based on this concept, two different moieties, i.e., fused dithienothiophene and carbazole, were utilized as donor monomers to synthesize fused dithienothiophene-based polymers **PCA** and **PCB** (see Figure 2.1). In order to integrate electron donor polymers (**PCA** and **PCB**) with electron acceptors,

pyridyl-surface-modified ZnO nanoparticles (**ZnOpy**) were synthesized according to Scheme 2.1. Compared with those reported fused dithienothiophene-based polymers, polymers **PCA** and **PCB** showed much improved open circuit voltage (V_{oc}) values with a highest open-circuit voltage of up to 0.88 V (in **PCB**) as well as suitable electronic energy levels and good processabilities for PSC applications. So far, the preliminary PSC performance of these structurally related copolymers showed the best PCE value of up to 0.55% while blended with **ZnOpy** and PCBM in a weight ratio of 1:0.05:1, with a short circuit current density (I_{sc}) of 2.11 mA/cm^2, an open circuit voltage (V_{oc}) of 0.88 V, and a fill factor (FF) of 0.29 under the solar simulator adjusted to give 100 mW/cm^2 of AM 1.5 G irradiation. Although the results for the PCE values of these nonoptimized PSCs are not sufficiently high enough, this research affords a new concept to incorporate electron donor polymers and electron acceptor surface-modified ZnO nanoparticles to the nanocomposite design.

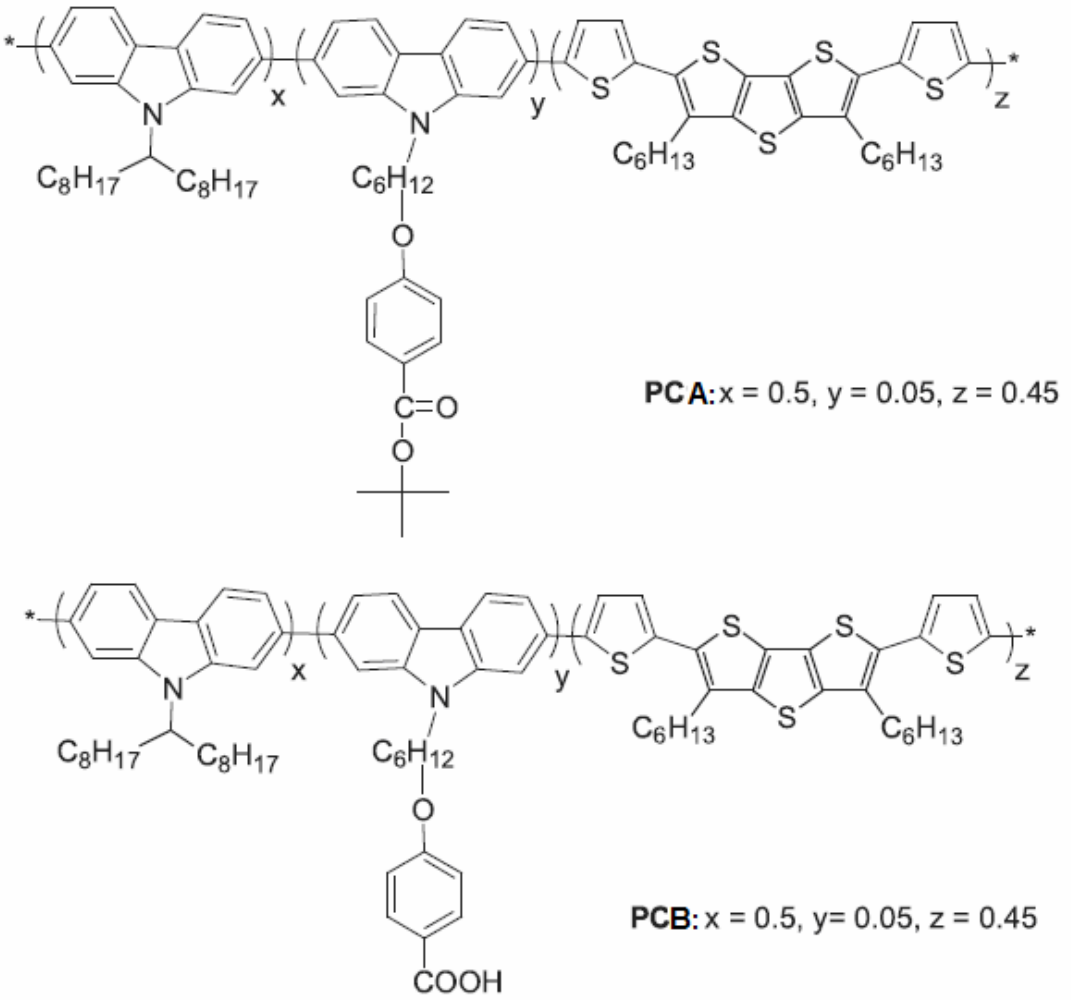

Figure 2.1 Chemical structures of polymers **PCA** and **PCB**.

2.2 Experimental

2.2.1 Materials

All chemicals and solvents were used as received. 2,7-dibromo-9-(heptadecan-9-yl)-9H-carbazole,[60] 2,7-dibromo-carbazole,[60] and 3,5-didecanyldithieno[3,2-b:2′3′-d]thiophene)[68-69] were synthesized according to the literature procedures. The detailed synthetic routes of polymers **PCA** and **PCB** will be published somewhere later. The synthetic routes of surface-modified ZnO nanoparticles (**ZnOpy**) are shown in Scheme 1. ZnO nanoparticles were synthesized by following the literature procedures.[70] Chemicals and solvents were reagent grades and purchased from Aldrich, ACROS, TCI, and Lancaster Chemical Co. Toluene, tetrahydrofuran, and diethyl ether were distilled to keep anhydrous before use.

2.2.2 Measurements and characterization

1H NMR spectra were recorded on a Varian Unity 300 MHz spectrometer using $CDCl_3$ solvents. Elemental analyseswere performed on a HERAEUS CHN-OS RAPID elemental analyzer. Transition temperature were determined by differential scanning calorimetry (DSC, Perkin-Elmer Pyris 7) with a heating and cooling rate of 10 °C/min. Thermogravimetric analyses (TGA) were conducted with a TA instrument Q500 at a heating rate of 10 °C/min under nitrogen. Gel permeation chromatography (GPC) analyses were conducted on a Waters 1515 separation module using

polystyrene as a standard and THF as an eluent. UV–visible absorption and photoluminescence (PL) spectrawere recorded in dilute chlorobenzene solutions (10^{-6} M) on a HP G1103A and Hitachi F-4500 spectrophotometer, respectively. Solid films of UV–vis and PL measurements were spin-coated on quartz substrates from chlorobenzene solutions with a concentration of 10 mg/mL. Cyclic voltammetry (CV) measurements were performed using a BAS 100 electrochemical analyzer with a standard threeelectrode electrochemical cell in a 0.1M tetrabutylammonium hexafluorophosphate ($TBAPF_6$) solution (in chorobenzene) at room temperature with a scanning rate of 50mV/s. In each case, a carbon working electrode coated with a thin layer of these copolymers, a platinum wire as the counter electrode, and a silver wire as the quasireference electrode were used. Ag/AgCl (3MKCl) electrode was served as a reference electrode for all potentials quoted herein. During the CV measurements, the solutions were purged with nitrogen for 30 s, and the redox couple ferrocene/ferrocenium ion (Fc/Fc^+) was used as an external standard. The corresponding HOMO and LUMO levels in copolymer films of **PCA**, **PCB** and **ZnOpy** were calculated from Eox/onset and Ered/onset values of the electrochemical experiments. The LUMO value of PCBM[69] was in accordance with the literature data. Each onset potential in the CV measurements was defined by the intersection of two tangents drawn at the rising current and background current. Film thickness and

morphology were determined using a Veeco Nanoscope DI 3100 AFM microscope operating in the tapping mode. The actual resolution of AFM measurements is 50 nm.

2.2.3 Device fabrication and characterization of polymer solar cells

The photovoltaic cell (PVC) device structure used in this study was a sandwich configuration of ITO/PEDOT:PSS/active layer/Ca/Al, where the active layer was made of electron donor polymers **PCA** and **PCB** mixed with both electron acceptors **ZnOpy** and [6,6]-phenyl C61 butyric acid methyl ester (PCBM) in the weight ratios of polymer:**ZnOpy**:PCBM=1:0.05:1 and 1:0.1:1. The PVC devices were fabricated according to the procedures similar to those of EL devices. The ITO coated glass substrates were pre-cleaned and treated with oxygen plasma prior to use. A thin layer (~50 nm) of PEDOT:PSS was spincoated on an ITO substrate and heated at 130 °C for 1 h. Subsequently, the preliminary active layer was prepared by spin coating from composite solutions of **PCA**, **PCB**:**ZnOpy**:PCBM in chlorobenzene (10 mg/mL) on the top of PEDOT:PSS layer. The spin rate was about 800 rpm, and the thickness of the active layer was typically ranged at 100–160 nm, unless the detailed thickness is specified. The PVC devices were completed by deposition with 1 nm of Ca and 120 nm of Al. The film thicknesses were measured by a profilometer (Dektak3, Veeco/Sloan Instruments Inc., USA). For photovoltaic measurements, I–V curves were recorded under a solar simulator with AM 1.5 irradiation (at 100 mW/cm^2). A

300W xenon lamp (Oriel, #6258) with AM 1.5 filter (Oriel, #81080 kit) was used as the white light source, and the optical power shone on the sample was 100 mW/cm^2 detected by Oriel thermopile 71964. The I-V characteristics were measured using a CHI 650B potentiostat/galvanostat. The external quantum efficiency (EQE) was measured using a CHI 650B coupled with Oriel Cornerstone 260 monochromator. All PVC devices were prepared and measured under ambient conditions.

2.2.4 Synthesis

The synthetic routes of surfactant and pyridyl-modified ZnO (**ZnOpy**) are shown in Scheme 2.1.

(Pyridine-4-yl) methyl-3-(trethoxysily)propylcarbamate

4-Pyridinylmethanol (628 mg, 5.76 mmol) and 3-(triethoxysilyl) propyl isocyanate (2.8 g, 11.48 mmol) were dissolved in dry THF (40 mL) and stirred in a flask. Besides, dibutyltin dilaurate (36 mg, 0.058 mmol) was added dropwise. The mixture was refluxed overnight. Solvent was removed under vacuum, and the crude product was purified by flash column chromatography using hexane/ethyl acetate=1:2, v/v as eluent. Subsequently, the pure compound was obtained as a yellow powder. Yield: 1.84 g (66%). 1H NMR (300 MHz, $CDCl_3$): δ (ppm) 8.68 (dd, 2H), 8.05 (d, 1H), 7.52 (dd, 2H), 5.34 (s, 2H), 3.82 (quart, 6H), 3.18 (m, 2H), 1.87 (quint, 2H), 1.22 (t, 9H), and 0.63 (t, 2H). HRMS (EI): calculation For $C_{16}H_{28}N_2O_5Si$, 356.49; found

356. Element analysis calculation for $C_{16}H_{28}N_2O_5Si$: N, 7.86; C, 53.91; and H, 7.92. Found: N, 7.90; C, 53.94; and H, 7.81.

Synthesis of pyridyl-modified ZnO nanoparticles (ZnOpy)

ZnO nanoparticles[70] were dissolved and stirred in dry toluene (10 mL). Then, (pyridine-4-yl) methyl-3-(trethoxysily)propylcarbamate (1 g, 0.058 mmol) was added dropwise. The mixture was stirred to react overnight at 100 °C. The resulting precipitates were isolated by centrifugation along with decantation, and then were rewashed several times to remove all residues. The resulting product was subsequently collected and dried under vacuum. The amount of pyridyl surface-modifiers attached to ZnO nanoparticle surface can be estimated by TGA analysis and was found ca. 5 wt.% in Figure 2.2. In addition, the sizes of ZnO nanoparticles surface-modified with pyridyl surfactants (**ZnOpy**) were ca. 3-4 nm.

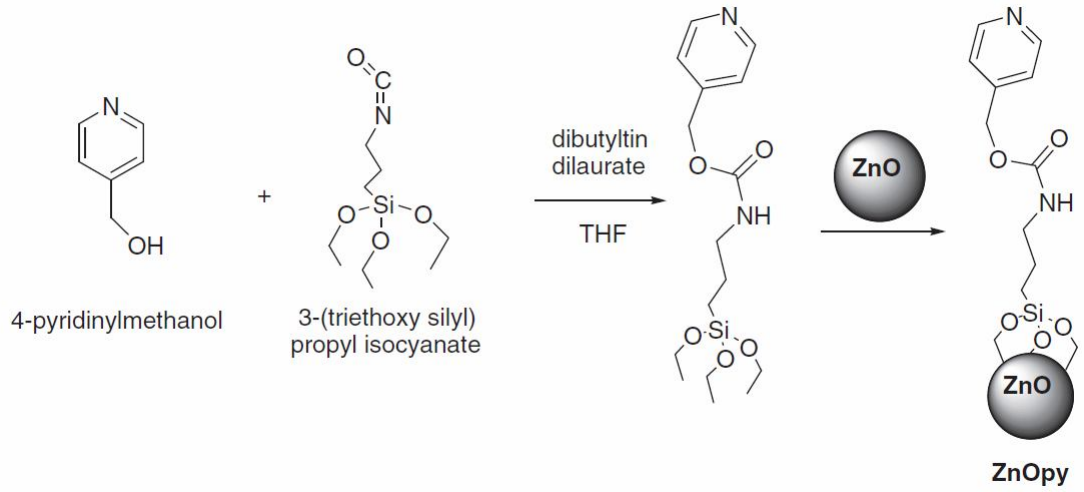

Scheme 2.1 Synthetic routes of surface-modified ZnO (**ZnOpy**).

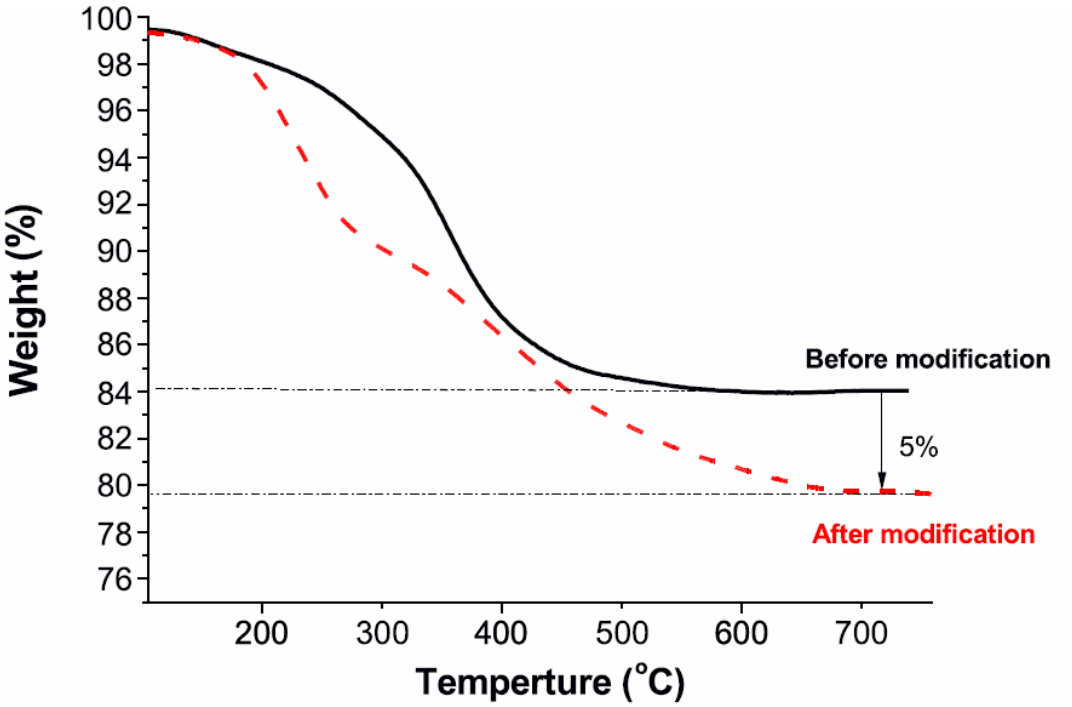

Figure 2.2 Thermogravimetric curves of ZnO nanoparticles before and after pyridyl surface- modification.

2.3 Results and Discussion

2.3.1 Thermal properties

The thermal stabilities and phase transition properties of polymers **PCA** and **PCB** were characterized by thermogravimetric analyses (TGA) and differential scanning calorimetry (DSC) measurements under nitrogen atmosphere, and the thermal decomposition temperatures (T_d) and melting points (T_m) are summarized in Table 2.1. It is apparent that all copolymers exhibited good thermal stabilities, which showed less than 5% weight loss upon heating to 366–408 °C. Regarding DSC experiments, samples (weighted 1-5 mg) sealed in an aluminum pan were operated at 30-250 °C under N_2 atmosphere with a scan rate of 10 °C/min. These polymers showed relatively sharp transitions appearing around 135-143 °C, which were attributed to the

melting of the polymer backbones, and two polymers exhibited the glass transition (T_g) temperatures at 135 °C and 143 °C for **PCA** and **PCB**, respectively. The T_g and T_d values of **PCB** are higher than that of **PCA**, implying that the polymer networks formed by H-bonds (due to acid groups) of **PCB** make the structure more rigid.

Table 2.1
Molecular weights, yields, and thermal data of polymers **PCA** and **PCB**

Polymer	M_n[a]	M_w[b]	PDI[c]	Tg[d] (°C)	T_d[e] (°C)	Yield (%)
PCA	19200	53100	2.7	135	366	79.5
PCB	18200	50100	2.7	143	408	80.0

[a] Number average molecular weight.
[b] Weight average molecular weight.
[c] Polydispersity indices (PDI = Mw/Mn).
[d] Glass transition temperature.
[e] Decomposition temperature at 5% weight loss.

2.3.2 Optical properties

The optical absorption spectra of polymers **PCA** and **PCB** in chlorobenzene solutions (10^{-6} M) and solid films are shown in Figure 2.3, and their photophysical properties are demonstrated in Table 2.2. As can be seen, the absorption spectra of polymers **PCA** and **PCB** covered broad wavelength ranges for both solutions and solid films. Similar maximum absorption wavelengths (442 and 441 nm) of **PCA** and **PCB** in chlorobenzene solutions were observed. These donor polymers (**PCA** and **PCB**) achieved the absorption spectra in the visible range of 350–580 nm (with tailing up to around 650 nm) in solid films. Due to the π–π stacking of these polymer chains in solids, both maximum absorption wavelengths in solid films were red-shifted to ca.

465 nm in polymers **PCA** and **PCB**. In addition, the long tailing around 650 nm in the absorption spectra of **PCA** and **PCB** in both solutions and solid films were observed. As shown in Table 2.2, the optical band gaps (E_g^{opt}) of 2.25 eV in polymers **PCA** and **PCB** can be determined by the cut off of the absorption spectra in solid films. The photoluminescence (PL) spectra of polymers **PCA** and **PCB** in chlorobenzene solutions and solid films excited at incident wavelengths of 465 nm are shown in Figure 2.4, respectively. The PL emission spectra of the polymers in the film were dramatically quenched. Interestingly, in contrast to polymer **PCA** in Figure 2.4, the PL spectra of **PCB** containing acid moieties were completely quenched in solid films. The corresponding optical properties of these copolymers in solid films, including the broad and strong optical absorptions, proposed their potential applications in the photovoltaic cells described below.

Table 2.2
Photophysical data of polymers **PCA** and **PCB** in chloroform solutions and solid films.

Polymer	$\lambda_{abs,sol}$[a] (nm)	$\lambda_{abs,film}$[b] (nm)	$\lambda_{PL,film}$[b] (nm)
PCA	442	465	543
PCB	441	465	–

[a] The absorption spectra were recorded in dilute chlorobenzene solution at room temperature.
[b] The absorption and PL films were spin-coated from 10 mg/1 mL chlorobenzene solution.

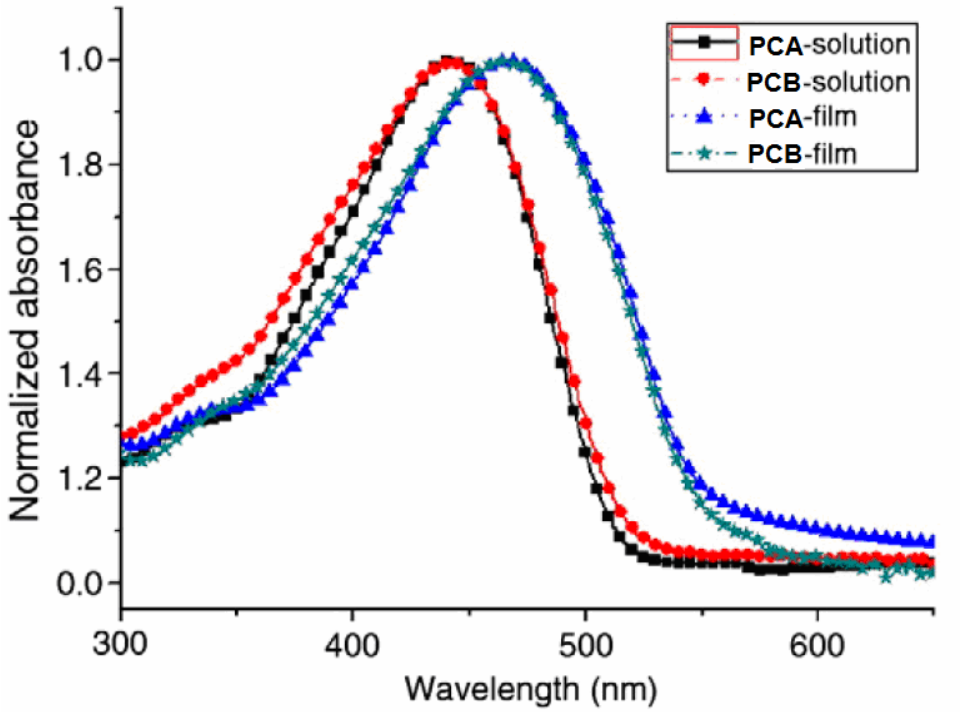

Figure 2.3 Normalized optical absorption spectra of polymers **PCA–PCB** in solutions (chlorobenzene) (10^{-6} M), and solid films (spin-coating from chlorobenzene solutions).

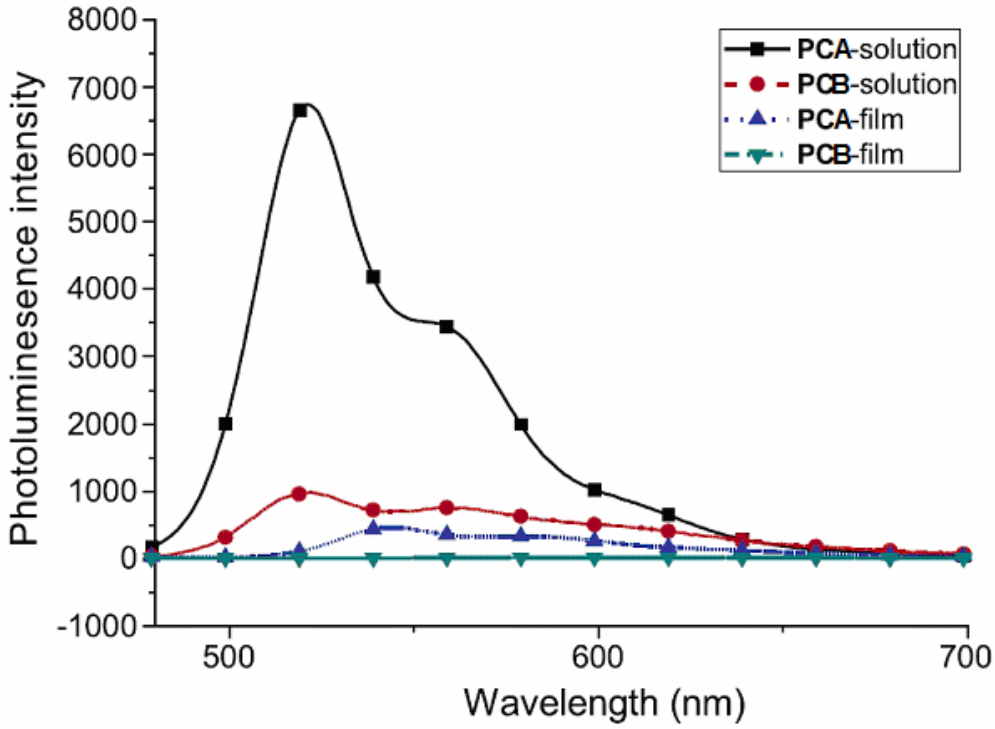

Figure 2.4 Normalized photoluminescence (PL) spectra of polymers **PCA–PCB** in solutions (chlorobenzene) (10^{-6} M), and solid films (spin-coating from chlorobenzene solutions).

2.3.3 Electrochemical characterization

The electronic states, i.e. highest occupied molecular orbital (HOMO) and lowest unoccupied molecular orbital (LUMO) levels, of the polymers were investigated by cyclic voltammetry (CV) in order to understand the charge injection processes in these polymers and their PSC devices. The oxidation and reduction cyclic voltammograms of polymers **PCA** and **PCB** in solid films are displayed in Figure 2.5. In order to obtain the solid films with an equal thickness, the concentrations in the THF solutions and film forming conditions were kept constant (ca. 5 mg/mL). The electrochemical measurements of the formal potentials, onset potentials, and band gaps, along with the estimated positions of the upper edges of the valence band (HOMO levels) and the lower edges of the conduction band (LUMO levels) are summarized in Table 2.3. On the contrary, all polymers **PCA** and **PCB** exhibited one quasi-reversible oxidation peaks as evident from the areas and close proximity of the anodic and cathodic scans in Figure 2.5, which are a good sign for high structural stability in the charged state. As illustrated in Table 2.3, the formal oxidation potentials of these polymers were in the range of 0.7–1.1 V. The moderate onset oxidation potentials of polymers **PCA** and **PCB** occurred between 0.7 and 1.1 V fromwhich the estimated HOMO levels of −5.60 eV and LUMO levels of ca. −3.35 eV were acquired according to the following equation:[72-73] $E_{HOMO/LUMO}=[-(E_{onset\ (vs\ Ag/AgCl)}- E_{onset\ (Fc/Fc+\ vs\ Ag/AgCl)}-4.8]$ eV, where 4.8 eV is the energy level of

ferrocene below the vacuum level and $E_{onset\ (Fc/Fc+\ vs\ Ag/AgCl)}$=0.4 eV. In contrast, the electrochemical reductions of polymers **PCA** and **PCB** showed similar LUMO energy levels at ca. −3.35 eV, which represent to possess high electron affinities and also make these polymers suitable electron donors for electron injection and transporting to **ZnOpy** and PCBM acceptors (with 0.4 eV offsets in LUMO levels regarding PCBM with a LUMO level of −3.75 eV,[70] as shown in Fig. 6 for the polymeric bulk heterojunction solar cell devices.[71] Interestingly, the energy band gaps E_g, measured directly from CV ($E_{g,}$=$E_{ox/onset}$−$E_{red/onset}$, where $E_{g,}$ values are 2.25 eV) are close to the optical band gaps ($E_{g,}^{opt}$ are 2.25 eV) acquired from the absorption spectra.

Table 2.3
Electrochemical potentials, energy levels, and band gap energies of polymers**PCA** and **PCB**[a].

Polymer	$\lambda_{onset,abs}$ (nm)	E_g[a] (eV)	$E_{1/2}$[b] (eV)	HOMO[c] (V)	LUMO[d] (V)
PCA	550	2.25	0.91	−5.60	−3.35
PCB	551	2.25	0.91	−5.60	−3.35

[a] The optical band gap was obtained from the equation $E_g^{opt} = 1240/\lambda_{onset}$.
[b] $E_{1/2}$ was the average value of oxidation and reduction potential.
[c] $E_{HOMO} = [-(E_{1/2} - 0.11) - 4.8]$ eV where 0.11 V is the value for ferrocene vs Ag/Ag^+ and 4.8 eV is the energy level of ferrocene below the vacuum.
[d] LUMO = HOMO − E_g.

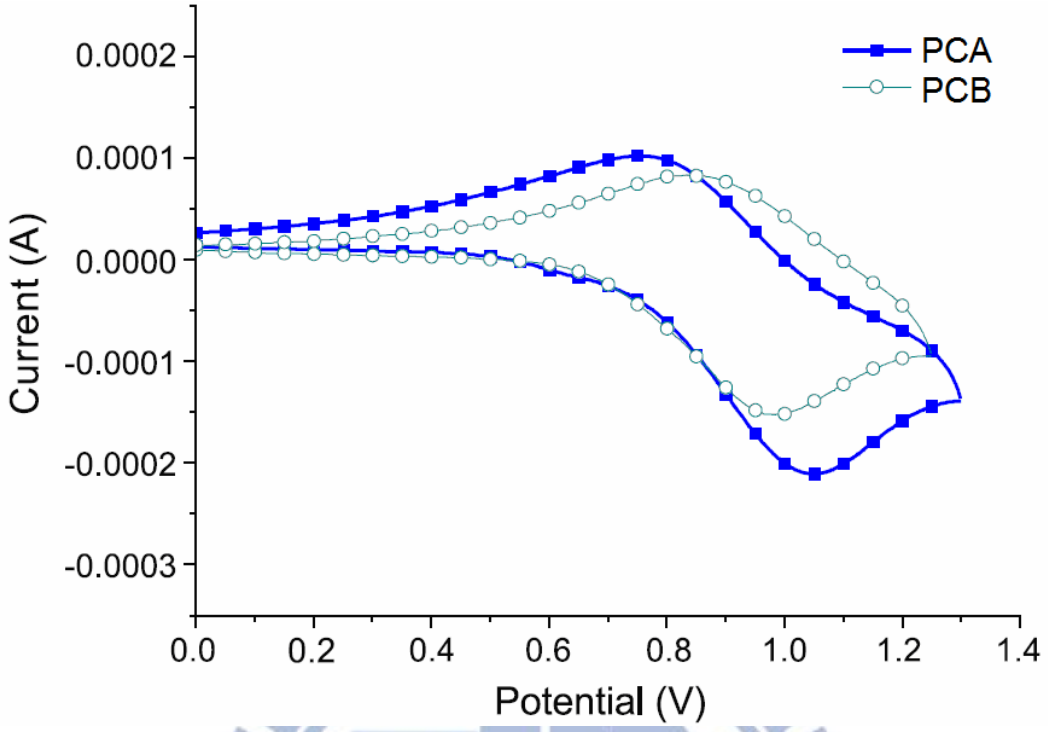

Figure 2.5. Cyclic voltammograms of polymers **PCA** and **PCB** (solid films) at a scan rate of 100 mV/s.

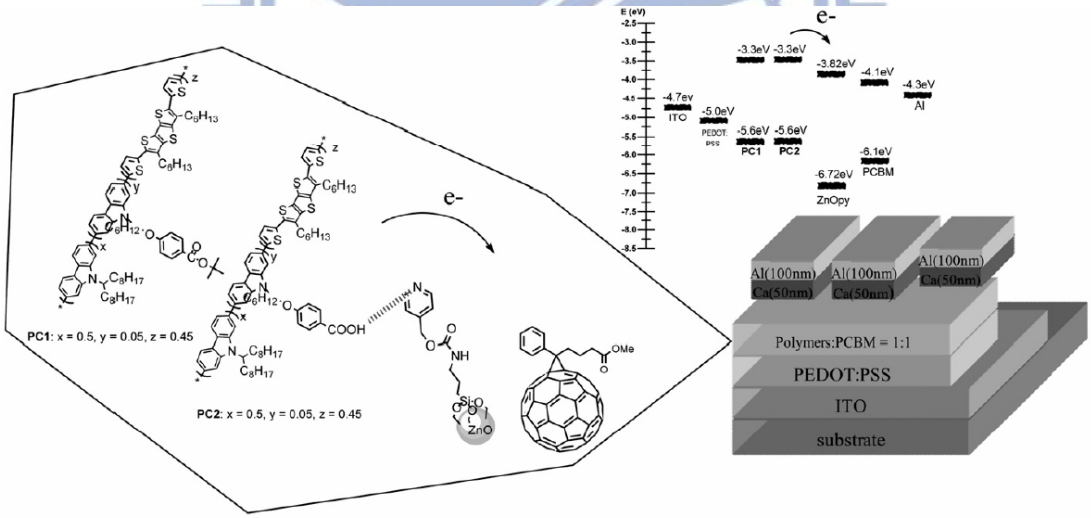

Figure 2.6. Energy band diagram of HOMO/LUMO levels for electron donor polymers **PCA** and **PCB**, electron acceptors **ZnOpy** and PCBM, and the work functions of ITO and Al.

2.3.4 Morphology

The AFM topographies by the tappingmode of polymer blends (**PCA**,**PCB**:**ZnOpy**:PCBM=1:0.05:1 and 1:0.1:1 in wt. ratios) were investigated via casting films of dichlorobenzene solutions as shown in Figure 2.7, where the bumps on the surface views are possibly attributed to the aggregation of ZnOnanoparticles (**ZnOpy**) and polymers (**PCA** and **PCB**). The results show that the morphologies of blends **PCA**/**ZnOpy**/PCBM have larger roughnesses (34 and 19 nmin Figure 2.7(a) and (b), respectively) than those (10 and 11 nmin Figure 2.7(c) and (d), respectively) of blends **PCB**/**ZnOpy**/PCBM. **PCA**/**ZnOpy**/PCBM films exhibited larger roughness variations than **PCB**/ **ZnOpy**/PCBM. The roughness and phase separation must be controlled/ optimized in order to improve the efficiency of devices.[74-76] It is worthy to mention that the solid films of blended **PCA**:**ZnOpy**:PCBM in different ratios of 1:0.05:1 and 1:0.1:1w/w showed rougher surfaces, but the larger values of rms roughnesses (34 and 19 nm, respectively) were contributed from the aggregation of nanoparticles due to no interaction between polymer and nanoparticles, which reduced the interfaces between donor (polymers) and acceptor (**ZnOpy**:PCBM) significantly. Owing to the unfavorable morphologies for charge transport offered by the aggregation of nanoparticles, the PSC devices based on **PCA** gave relatively low current densities (I_{sc}) as shown in Table 2.4.

Table 2.4
Photovoltaic properties of PSC devices containing an active layer of Polymer:**ZnOpy**:PCBM (w/w) with a device configuration of ITO/PEDOT:PSS/Polymer:**ZnOpy**:PCBM/Ca/Al[a].

Active layer (polymer:**ZnOpy**:PCBM)	V_{oc} (V)	J_{sc} (mA/cm2)	FF (%)	PCE (%)
PCA:**ZnOpy**:PCBM = 1:0.05:1	1.79	0.79	0.31	0.44
PCA:**ZnOpy**:PCBM = 1:0.1:1	1.57	0.77	0.29	0.35
PCB:**ZnOpy**:PCBM = 1:0.05:1	2.11	0.88	0.29	0.55
PCB:**ZnOpy**:PCBM = 1:0.1:1	2.14	0.82	0.29	0.51

[a] Measured under AM 1.5 irradiation, 100 mW/cm^2.

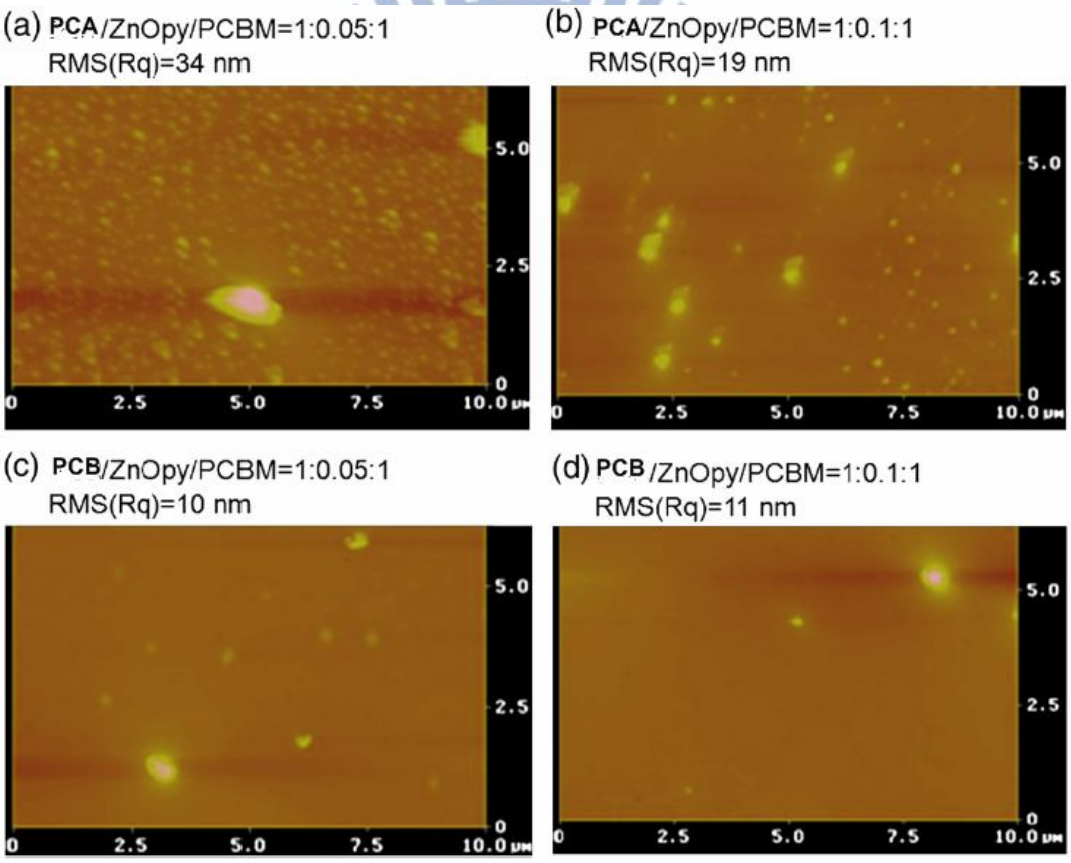

Figure 2.7 The AFM images obtained for films of **PCA**/**ZnOpy**/PCBM and **PCB**/**ZnOpy**/PCBM containing different amounts of nanoparticles and fullerene.

2.3.5 Polymeric photovoltaic cell properties

The motivation for the design and syntheses of the conjugated polymers is to look for new polymers for the application of PSCs. To investigate the potential use of polymers **PCA** and **PCB** in PSCs, bulk heterojunction devices were fabricated from an active layer in which polymers **PCA** and **PCB** were blended with the **ZnOpy** and PCBM. The PSC devices with a configuration of ITO/PEDOT:PSS/**PCA**, **PCB**:**ZnOpy**: PCBM(w/w)/Ca/Al were fabricated by depositing a thin layer (ca. 50 nm) of PEDOT:PSS onto patterned ITO slides. The active layer (ca. 100-160 nm) consisting of **PCA**, **PCB**, **ZnOpy** and PCBM (w/w) was then deposited from a solution (10 mg/mL in dichlorobenzene) by a spin rate of 500 rpm on the PEDOT:PSS film, and followed by the deposition of Ca (ca. 50 nm) and aluminum (100 nm) back electrodes.

The PSC devices were measured under AM 1.5 illuminations for a calibrated solar simulator with an intensity of 100 mW/cm^2. The preliminarily obtained properties are summarized in Table 2.4, and the typical I-V characteristics of all PSC devices are shown in Figure 2.8. The PSC device containing polymer **PCB** blended with **ZnOpy** and PCBM acceptors had the highest PCE value of 0.55% with the values of I_{sc}=2.11 mA/cm^2, FF=29.4%, and V_{oc}=0.88 V.

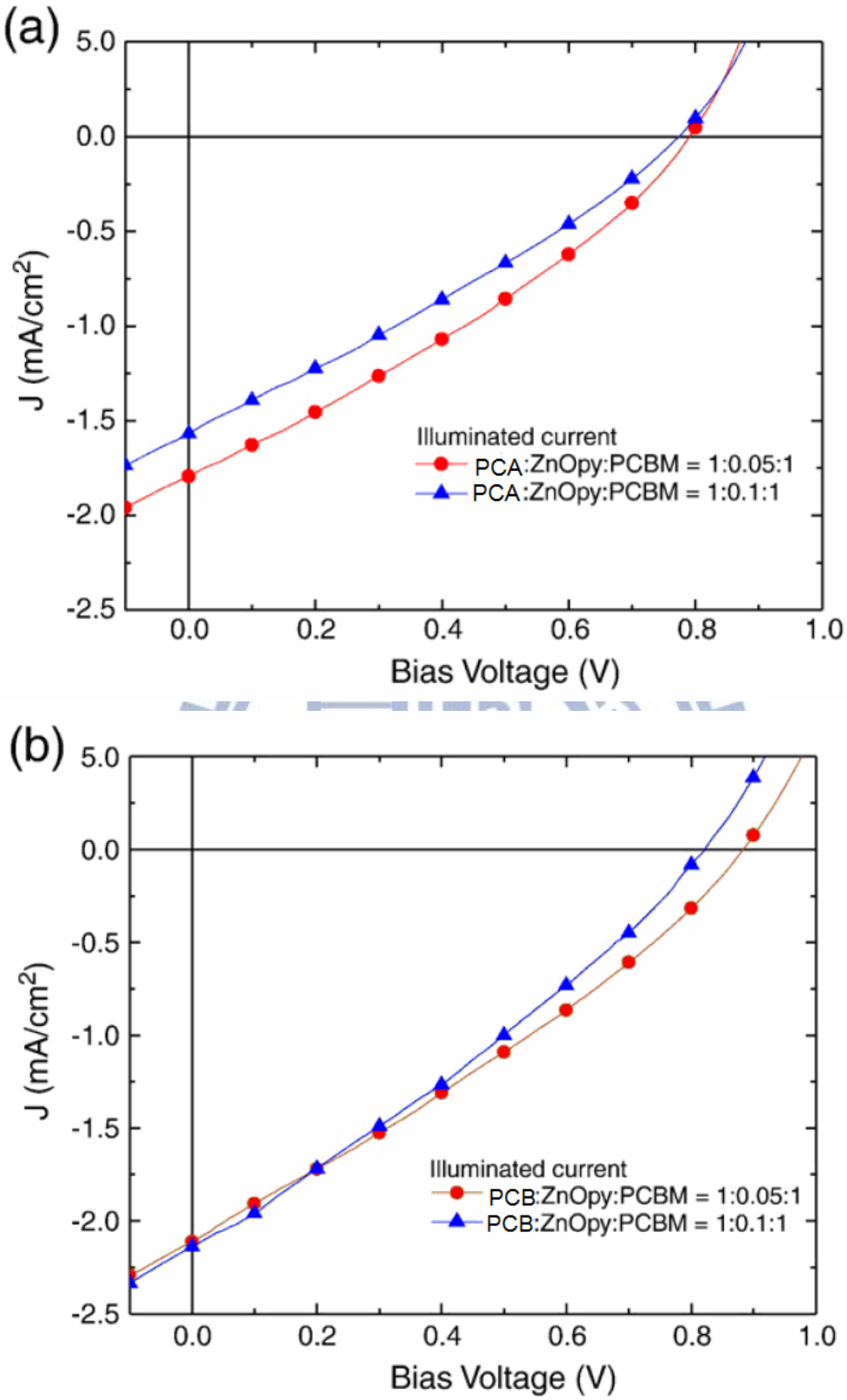

Figure 2.8 I-V curves of solar cells under simulated AM 1.5 solar irradiation with an active layer of (a) **PCA**:**ZnOpy**:PCBM (with different weight ratios of **ZnOpy**) and (b) **PCB**: **ZnOpy**:PCBM (with different weight ratios of **ZnOpy**).

2.4 Conclusions

The concept of supermolecular interactions, such as H-bonds formed between conjugated polymers (**PCA** and **PCB**) and surface-modified nanoparticles ZnO (**ZnOpy**), has been introduced by the syntheses of **ZnOpy** nanoparticles and two fused dithienothiophene/carbazole-based polymers. The band gaps and the HOMO/LUMO energy levels of these resulting copolymers can be finely tuned as demonstrated by the investigation of optical absorption properties and electrochemical studies. The pyridyl surfactants of **ZnOpy** nanoparticles (as electron acceptors to partially replace expensive electron acceptor PCBM) not only induce supramolecular interactions with benzoic acid pendants of polymer **PCB** via H-bonds, but also enhance the homogeneous dispersions of **ZnOpy** nanoparticles in polymer **PCB**. Thus, the PSC device containing ternary components of polymer **PCB** blended with **ZnOpy** and PCBM acceptors (**PCB**:**ZnOpy**:PCBM=1:0.05:1) had the power conversion efficiency of up to 0.55%, which gave the best performance with the values of I_{sc}=2.11mA/cm^2, FF=29.4%, and V_{oc}=0.88 V.

Chapter 3

Synthesis of Novel Dithienothiophene- and 2,7-Carbazole-Based Conjugated Polymers and H-Bonded Effects on Electrochromic and Photovoltaic Properties

*Three kinds of dithienothiophene/carbazole-based conjugated polymers (**PCC**, **PCA** and **PCB**), which bear acid-protected and benzoic acid pendants in **PCA** and **PCB**, respectively, were synthesized via Suzuki coupling reaction. Interestingly, **PCC**, **PCA** and **PCB** exhibited reversible electrochromism during the oxidation processes of cyclic voltammogram studies, and **PCB** (with H-bonds) revealed the best electrochromic property with the most noticeable color change. According to powder X-ray diffraction (XRD) analysis, these polymers exhibited obvious diffraction features indicating bilayered packings between polymer backbones and π–π stacking between layers in the solid state. Compared with the XRD data of **PCA** (without H-bands), H-bonds of **PCB** induced a higher crystallinity in the small-angle region (corresponding to a higher ordered bilayered packings between polymer backbones), butwith a similar crystallinity in the wide angle region indicating a comparable π–π stacking distance between layers. Moreover, based on the preliminary photovoltaic properties of PSC devices*

*(**PCC**, **PCA** and **PCB** blended individually with PCBM acceptor in the weight ratio of 1:1), **PCB** (with H-bonds) possessed the highest power conversion efficiency of 0.61% (with J_{sc} =2.26 mA/cm^2, FF=29.8%, and V_{oc} = 0.9 V). In contrast to **PCA** (without H-bands), the thermal stability, crystallinity, and electrochromic along with photovoltaic properties of **PCB** were generally enhanced due to its H-bonded effects.*

3.1 Introduction

Novel materials are developed for organic optoelectronic devices, such as polymeric solar cells (PSCs), which is a popular research topic in recent decades, because they are low cost and green materials for sustainable resources to reduce consumptions of fossil energy and nuclear power.[2] In particularly, bulk heterojunction (BHJ) solar cells consisting of electron-donating conjugated polymers blended with electron-accepting fullerenes are fabricated in solid thin films.[3] Up to now, regio-regular poly[2-methoxy-5-(3',7'-dimethyloctyloxy)-p-phenylenevinylene] (MDMO-PPV)[4] and poly(3-hexylthiophene) (P3HT)[5] as electron donors blended with [6,6]-phenyl-C61-butyric acid methyl ester (PCBM) as an electron acceptor approached high power conversion efficiency (PCE) values of 5.0% in PSCs. More recently, the PCE values of BHJ solar cells using new low-band gap conjugated polymers have reached 6 to 8%.[6-7] The PCE values of BHJ solar cells were

affected by, for example, the energy band gaps of polymers, which is related to the chemical structure of the conjugated polymers. In order to improve the thermal stabilities of polymers by longer conjugation lengths and more rigid structures, novel heteroaromatic fused-ring derivatives, including fused dithienothiophene and carbazole units, are integrated into the polymer backbones. Carbazole unit, which is well known to be a good electron-donating moiety[77] due to its fully aromatic structure, can improve chemical stability in contrast to fluorene unit, and thus poly(2,7-carbazole)s are attractive candidates for solar cells.[80] New carbazole-based copolymers utilized in BHJ solar cells were also reported to achieve a PCE value of 4.3%.[81] According to all these results, the development of new polymers based on carbazole units should have interesting features for the photovoltaic applications. Dithieno[3,2-b:2',3'-d]thiophene (DTT) unit is a sulfur-rich (three S atoms) and electron-rich building block to make the polymer backbones more rigid and coplanar, and thus to have longer π-conjugation and absorption lengths along with narrower band gaps.[82,83(a)] Due to the limiting intramolecular rotation in the fused-ring structures, such as DTT, the p-orbital overlaps in conjugated molecules could be maximized to enhance intermolecular charge transports.[83(b,c)] In order to improve the solubility of poly(DTT), alkyl-substituted pendants were incorporated into the polymer backbones, which

can be applied to organic solar cells[82-85] and field effect transistors (FETs).[83]

Hydrogen bonds (H-bonds) are ideal noncovalent interactions to form self-assembled architectures due to their selectivity and directionality. A numerous advantages of H-bonded polymers, such as stronger light absorptions, lower HOMO levels, higher Voc values, higher hole mobilities, and higher crystallinities, were utilized for organic solar cells.[12] Therefore, great efforts have been taken toward the preparation and characterization of photo- and electroactive noncovalent assemblies based on hydrogen bonds (H-bonds). Wurthner,[12(a,b)] El-ghayoury et al., and Jonkheijm et al.[12(c,d)] reported H-bonded assemblies of perylene bisimide and melamine derivatives. In addition, El-ghayoury et al. reported a PCE value of 0.39% for PSCs by utilizing a H-bonded polymer containing oligo(p-phenylene vinyene) and ureido-pyrimidinone units.[12(c)] Because of several advantages in polymers, including low cost, easy processing, and tunable chemical properties, the conjugated polymers consisting of different heteroaromatic rings, such as thiophene and carbazole, exhibit an electrochromic behavior as well as photovoltaic properties. Based on this concept, two different moieties, i.e., carbazole (**M1** and **M2**) and fused dithienothiophene (**M3**), were applied into electron-donor monomers to synthesize fused-dithienothiophene-based polymers **PCC**, **PCA** and **PCB**, where **PCC** is a model polymer and the acid pendants of **PCB** are protected in **PCA** to compare the

H-bonded effects on their electrochromic behavior as well as photovoltaic properties.

3.2 Experimental Section

3.2.1 Materials

All chemicals and solvents were used as received; 2,7-dibromo-9-(heptadecan-9-yl)-9H-carbazole (**1**),[79] 2,7-dibromocarbazole (4),[79] and 3,5-didecanyldithieno[3,2-b:2'3'-d] thiophene) (**5**)[68] were synthesized according to the literature procedures. The synthetic routes of monomers 1–3 and polymers **PCC**, **PCA** and **PCB** are shown in Schemes 3.1 and 3.2, and the synthetic procedures of their intermediates were described. Chemicals and solvents were reagent grades and purchased from Aldrich, ACROS, TCI, and Lancaster Chemical Co. Toluene, tetrahydrofuran, and diethyl ether were distilled to keep anhydrous before use.

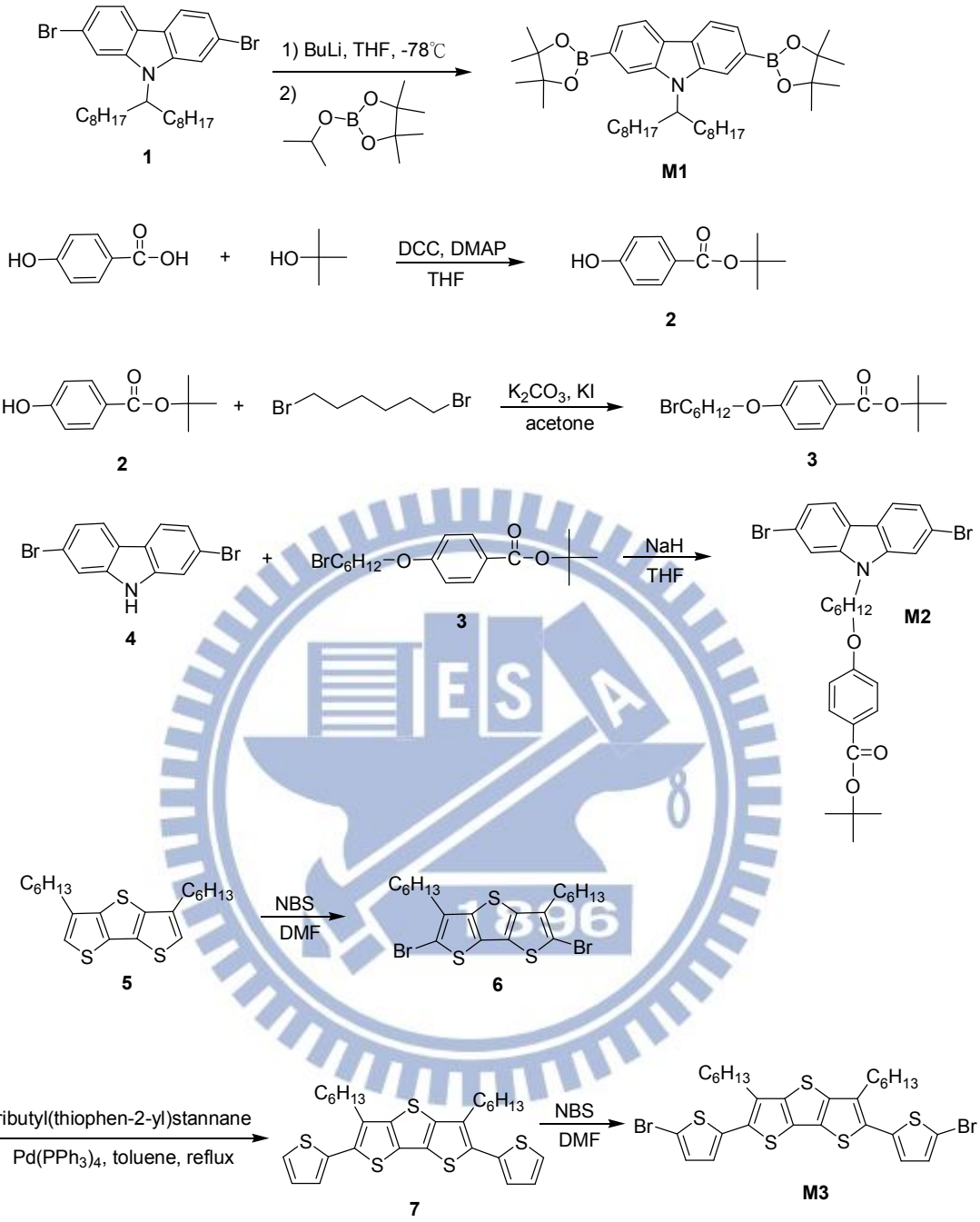

Scheme 3.1 Synthetic routes of monomers **M1**–**M3**.

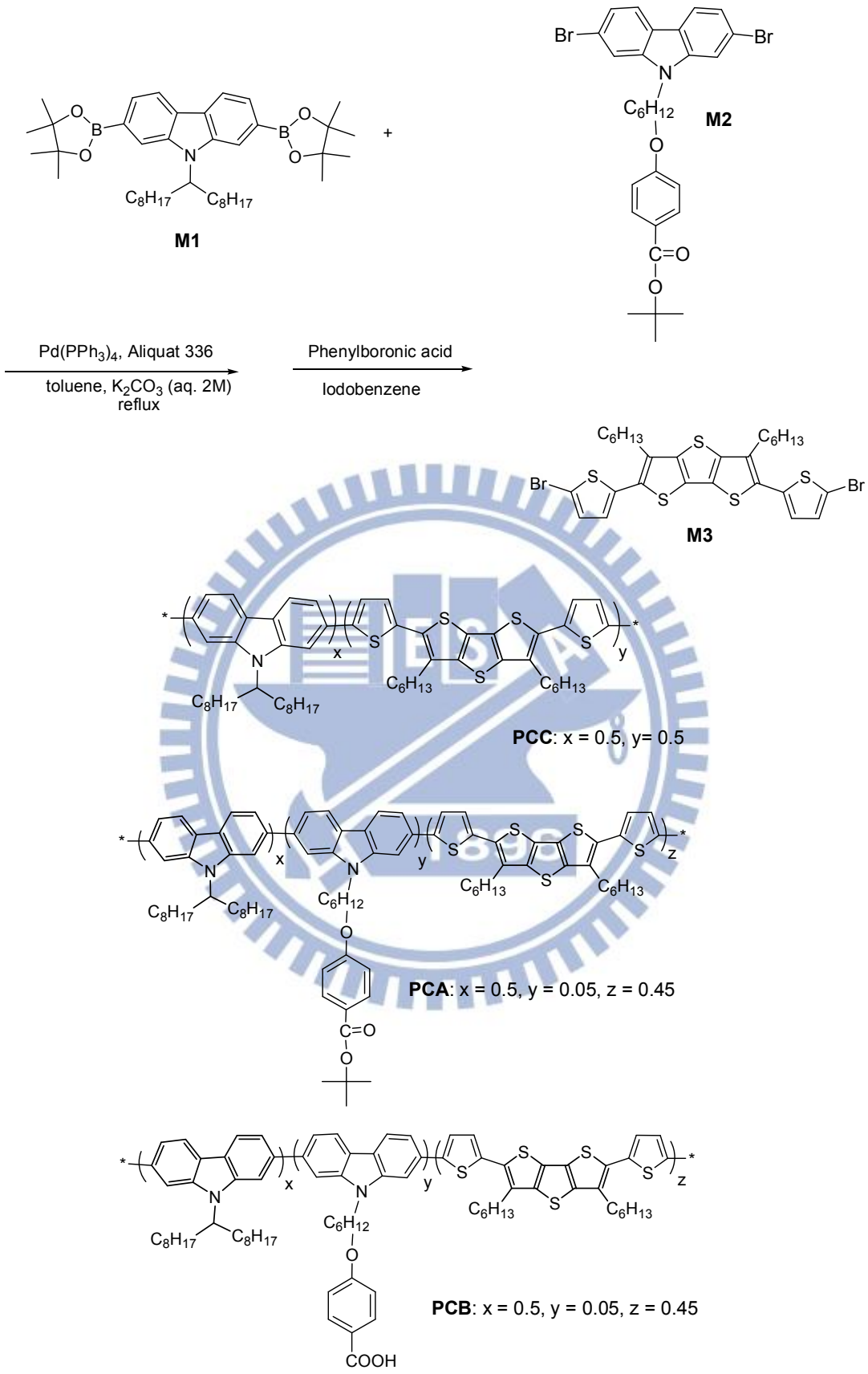

Scheme 3.2 Synthetic routes of polymers **PCC**, **PCA** and **PCB**.

3.2.2 Measurements

1H NMR spectra were recorded on a Varian Unity 300 MHz spectrometer using $CDCl_3$ solvents. Elemental analyses were performed on a HERAEUS CHN-OS RAPID elemental analyzer. Transition temperatures were determined by differential scanning calorimetry (DSC, Perkin-Elmer Pyris 7) with a heating and cooling rate of 10 °C /min. Thermogravimetric analyses (TGA) were conducted with a TA instrument Q500 at a heating rate of 10 °C /min under nitrogen. Gel permeation chromatography (GPC) analyses were conducted on a Waters 1515 separation module using polystyrene as a standard and tetrahydrofuran (THF) as an eluent. UV-Vis absorption and photoluminescence (PL) spectra were recorded in dilute THF solutions (10^{-6} M) on a HP G1103A and Hitachi F-4500 spectrophotometer, respectively. Solid films of UV-Vis and PL measurements were spin-coated on a quartz substrate from THF solutions with a concentration of 10 mg/mL. Cyclic voltammetry (CV) measurements were performed using a BAS 100 electrochemical analyzer with a standard three-electrode electrochemical cell in a 0.1 M tetrabutylammonium hexafluorophosphate ($TBAPF_6$) solution (in dimethylformamide, DMF) at room temperature with a scanning rate of 100 mV/s. In each case, a carbon working electrode coated with a thin layer of these polymers, a platinum wire as the counter electrode, and a silver wire as the quasi-reference

electrode were used. Ag/AgCl (3 M KCl) electrode was served as a reference electrode for all potentials quoted herein. During the CV measurements, the solutions were purged with nitrogen for 30 s, and the redox couple ferrocene/ferrocenium ion (Fc/Fc^{+}) was used as an external standard. The corresponding HOMO levels in polymer solutions of **PCC**, **PCA** and **PCB** could be calculated from $Eo_{x/onset}$ values of the electrochemical experiments (but no reduction curves, i.e., no $E_{red/onset}$ values and LUMO levels, were obtained in the CV measurements). Each onset potential in the CV measurements was defined by the intersection of two tangents drawn at the rising current and background current. The LUMO value of PCBM[41] was in accordance with the literature data. Film thickness and morphology were determined using a Veeco Nanoscope DI 3100 AFM microscope operating in tapping mode. Synchrotron powder X-ray diffraction (XRD) measurements were performed at beamline BL13A of the National Synchrotron Radiation Research Center (NSRRC), Taiwan, where the wavelength of X-ray was 1.026503 A. The photovoltaic cell (PVC) device structure used in this study was a sandwich configuration of ITO/PEDOT:PSS/active layer/Ca/Al, where the active layer was made of electron donor polymers **PCC**, **PCA and PCB** mixed with electron acceptor [6,6]- phenyl C61 butyric acid methyl ester (PCBM) in a weight ratio1:1. The PVC devices were

fabricated according to the procedures similar to those of EL devices. An ITO-coated glass substrate was precleaned and treated with oxygen plasma before use. A thin layer (ca. 50 nm) of PEDOT:PSS was spincoated on an ITO substrate and heated at 130 °C for 1 h. Subsequently, the preliminary active layer (ca. 100–160 nm) was prepared by spin coating from composite solutions of polymer: PCBM (w/w = 1:1) in dichlorobenzene (10 mg/mL) by a spin rate of 500 to 800 rpm on the top of the PEDOT:PSS layer. The PVC devices were completed by deposition with a back electrode consisting of Ca (ca. 50 nm) and aluminum (100 nm). The film thicknesses were measured by a profilometer (Dektak3, Veeco/Sloan Instruments Inc.). For PVC measurements, I–V curves were recorded under a solar simulator with AM 1.5 irradiation (at 100 mW/cm^2). A 300 W xenon lamp (Oriel, #6258) with AM 1.5 filter (Oriel, #81080 kit) was used as the white light source, and the optical power at the sample was 100 mW/cm^2 detected by Oriel thermopile 71964. The I–V characteristics were measured using a CHI 650B potentiostat/galvanostat. The external quantum efficiency (EQE) was measured using a CHI 650B coupled with Oriel Cornerstone 260 monochromator. All PVC devices were prepared and measured under ambient conditions.

3.2.4 Synthesis and Characterization Materials

9-(Heptadecan-9-yl)-2,7-bis(4,4,5,5-tetramethyl-1,3,2-dioxaborolan-2-yl)-9H-carbazole (M1).

To a solution of compound 1 (2,7-dibromo-9-(heptadecan-9-yl)-9H-carbazole)[79] (3.62 g, 6.42 mmol) in 150 mL of dry THF, n-butyllithium (2.5 M solution in hexane, 5.65 mL, 2.2 eq) was added dropwise, and then stirred to react at -78 °C under nitrogen. After reaction for 2 h at -78 °C, 2-isopropoxy-4,4,5,5-tetramethyl-1,3,2-dioxaborolane (3.15 mL, 2.4 eq) was added carefully to the mixture solution at -78 °C and then the mixture was allowed to warm up to react at room temperature overnight. The final solution was acidified with 100 mL of 10% HCl solution and stirred for 45 min at room temperature and the final solution was extracted with diethyl ether. The organic layer was dried over magnesium sulfate, and the solvent was evaporated. The solvent was removed under reduced pressure, and the residue was purified by recrystallization in methanol/acetone (ca. 10:1) to obtain the final product as a white crystal (2.69 g, yield: 64 %). 1H NMR($CDCl_3$, 300 MHz): δ 8.12 (d, J = 8.0 Hz, 2H), 8.02 (s, 1H), 7.89 (s, 1H), 7.66 (d, J = 8.1 Hz, 2H), 4.73–4.66 (m, 1H), 2.35–2.30 (m, 2H), 1.98–1.90 (m, 2H), 1.39–1.12 (m, 48H), 0.82 (t, J = 7.0 Hz, 6H). MS (FAB): m/z [Mt] 657; calcd. m/z [Mt] 657. Anal. Calcd.: C, 74.89; H, 9.96; N, 2.13. Found: C, 74.42; H, 9.68; N, 2.26.

tert-Butyl 4-hydroxybenzoate (2).

Seven grams of 4-hydroxybenzoic acid (50.7 mmol) and 4-dimethylaminopyridine (0.62 g, 0.1 eq) were dissolved in 60 mL of dry THF and stirred in a two-necked flask.

Then, 2-methylpropan-2-ol (60 mL, 2-methylpropan-2-ol) and N,N'-dicyclohexylcarbodiimide (12.6 g, 1.2 eq) were added sequentially. The mixture was purged with nitrogen and vigorously stirred overnight at room temperature. Water was added after reaction, and the reaction mixture was extracted with dichloromethane. Consequently, the organic layer was separated and dried with magnesium sulfate. Solvent was removed under vacuum, and the crude product was purified by chromatography using hexane: ethyl acetate (4:1) as eluent. Subsequently, the pure compound was obtained as a white powder. Yield: 3.95 g (40 %). 1H NMR ($CDCl_3$, 300 MHz): δ 7.87 (d, J =8.7 Hz,2H), 6.84 (d, J = 8.5 Hz, 2H), 6.44 (s, 1H), 1.59 (s, 9H).

tert-Butyl 4-(6-bromohexyloxy) benzoate (3).

tert-Butyl-4-hydroxybenzoate (3.95 g, 20.3 mmol), K_2CO_3 (8.43 g, 3 eq), and KI (0.2 g, 0.06 eq) were dissolved in acetone (150 mL) and stirred in a two-necked flask. The mixture was purged with nitrogen and refluxed overnight. Water was added after reaction, and the reaction mixture was extracted with dichloromethane. Consequently, the organic layer was separated and dried with magnesium sulfate. Solvent was removed under vacuum, and the crude product was purified by chromatography using hexane: ethyl acetate (30:1) as eluent. Subsequently, the pure compound was obtained as a colorless oil. Yield: 6.48 g (89%). 1H NMR($CDCl_3$, 300 MHz): δ 7.89 (d, J = 8.7

Hz, 2H), 6.86 (d, J = 8.5 Hz, 2H), 3.98 (t, J = 6.4 Hz, 2H), 3.40 (t, J = 6.8 Hz, 2H), 1.90–1.77 (m, 4H), 1.56 (s, 9H), 1.51–1.46 (m, 4H).

tert-Butyl 4-(6-(2,7-dibromo-9H-carbazol-9-yl)hexyloxy)-benzoate (M2).

NaH (0.36 g, 1.8 eq) and 2,7-dibromo-carbazole[60] (2.71 g, 8.34 mmol) were dissolved in THF (10 mL) and stirred in a two-necked flask and refluxed for 1 h. The solution of tert-butyl-4-(6-bromohexyloxy)benzoate (3.7 g, 1.3 eq) in THF (10 mL) was added dropwise and refluxed overnight. Water was added after reaction, and the reaction mixture was extracted with dichloromethane. Consequently, the organic layer was separated and dried with magnesium sulfate. Solvent was removed under vacuum, and the crude product was purified by chromatography using hexane: ethyl acetate (1:7) as eluent. Subsequently, the pure compound was obtained as a colorless oil. Yield: 2.90 g (60 %). 1H NMR($CDCl_3$, 300 MHz): δ 7.90 (m, 4H), 7.53 (d, J = 1.2 Hz, 2H), 7.34 (dd, J = 9.0, 1.6 Hz, 2H), 6.84 (d, J = 8.9 Hz, 2H), 4.22 (t, J = 7.2 Hz, 2H), 3.96 (t, J = 6.29 Hz, 2H), 1.91–1.75 (m, 4H), 1.59–1.44 (m, 13H). MS (EI): m/z [Mt] 601; calcd m/z [Mt] 601. Anal. Calcd.: C, 57.92; H, 5.28; N, 2.33. Found: C, 57.78; H, 5.04; N, 2.52.

2,6-Dibromo-3,5-dihexyldithieno[3,2-b:2’3’-d]thiophene (6).

Compound 5 (3,5-dihexyldithieno[3,2-b:2’3’-d]thiophene)17 (1.96 g, 5.38 mmol) and NBS (2.39 g, 2.5 eq) were dissolved in 50 mL of DMF. The resulting solution was

stirred to react overnight at room temperature under nitrogen. Water (50 mL) was then added, and the organic phase was extracted with ethyl acetate (100 mL) twice, washed with water, and dried with magnesium sulfate. After that, the solvent was removed under reduced pressure to obtain the product. The crude product was purified by column chromatography with hexane to obtain a pale yellow oil (2.51 g). Yield: 89 %. 1H NMR($CDCl_3$, 300 MHz): δ 2.72 (t, J = 7.5 Hz, 4H), 1.75–1.65 (m, 4H), 1.42–1.32 (m, 12H), 0.92–0.88 (m, 6H).

2,6-Dithienyl-3,5-dihexyldithieno[3,2-b:2'3'-d]thiophene(7).

Compound 5, 3,5-dihexyldithieno[3,2-b:2'3'-d]thiophene (2.46 g, 4.71 mmol), $Pd(PPh_3)_4$ (0.32 g, 0.06 eq), and tributyl(thiophen-2-yl)stannane (3.29 mL, 2.2 eq) were dissolved in toluene (25 mL) and stirred in a two-necked flask to reflux for 12 h. Solvent was removed under vacuum, and the crude product was purified by chromatography using hexane as eluent. Subsequently, the pure compound was obtained as a yellow powder. Yield: 2.12 g (86 %). 1H NMR ($CDCl_3$, 300 MHz): δ 7.35 (dd, J = 5.1, 1.0 Hz, 2H), 7.18 (t, J = 1.0 Hz, 2H), 7.09 (dd, J = 5.1, 3.6 Hz, 2H), 2.91 (t, J = 8.1 Hz, 4H), 1.67–1.61 (m, 4H), 1.42–1.27 (m, 12H), 0.94–0.89 (m, 6H).

2,6-Bis(2'-bromothien-5'-yl) 3,5-dihexyldithieno[3,2-b:2'3'-d] thiophene (M3).

About 2.12 g of 2,6-dithienyl-3,5-dihexyldithieno[3,2-b:2'3'-d]thiophene (4.01 mmol) and NBS (2.1 g, 2.1 eq) were dissolved in DMF (20 mL) and stirred in a flask. The

mixture was vigorously stirred overnight at room temperature. Water was added after reaction, and the reaction mixture was extracted with ethyl acetate. Consequently, the organic layer was separated and dried with magnesium sulfate. Solvent was removed under vacuum, and the crude product was purified by chromatography using hexane as eluent. Subsequently, the pure compound was obtained as a pale yellow powder. Yield: 2.0 g (73%). 1H NMR($CDCl_3$, 300 MHz): δ 7.04 (d, J = 3.5 Hz, 2H), 6.9 (d, J = 3.5 Hz, 2H), 2.85 (t, J = 7.3 Hz, 4H), 1.75-1.73 (m, 4H), 1.41–1.26 (m, 12H), 0.92–0.89 (m, 6H). MS (EI): m/z [Mt] 685; calcd. m/z [Mt] 685. Anal. Calcd.: C, 48.98; H, 4.40. Found: C, 48.89; H, 4.63.

General Synthetic Procedures of Polymers PCC, PCA and PCB [42]

The synthetic routes of polymers **PCC**, **PCA** and **PCB** are shown in Scheme 3.2. All of the polymerization procedures were carried out through the palladium (0)-catalyzed Suzuki coupling reactions. In a 25 mL two-necked flask, 0.5 eq of **M1** and **M2** with a molar ratio of **M2**:**M3** = 0:0.5(**PCC**) and 0.05:0.45 (**PCA** and **PCB**) were added into 5 mL of anhydrous toluene. The Pd (0) complex, tetrakis(triphenylphosphine)palladium (1 mol %), was transferred into the mixture under dry environment. Then, 2 M aqueous potassium carbonate and a phase transfer catalyst, that is, Aliquat 336 (several drops), were subsequently transferred to the previous mixture via dropping funnel. The reaction mixture was stirred at 90 °C for 2

days, and then both excess amounts of end-cappers (i.e., iodobenzene and phenylboronic acid) were correspondingly dissolved in 1 mL of anhydrous toluene and reacted for 4 h. The reaction mixture was cooled to 40 °C and added slowly into a vigorously stirred mixture of methanol/water (10:1). The polymers were collected by filtration and reprecipitation from methanol. The crude polymers were further purified by washing with acetone for 3 days in a Soxhlet apparatus to remove oligomers and catalyst residues. The chloroform fractions (350–400 mL) were reduced to 40–50 mL under reduced pressure, and precipitated in acetone along with air-dried overnight finally.

PCC

Following the general polymerization procedure, **M1** (0.5 equiv) and **M3** (0.5 equiv) were used in this polymerization to obtain a red powder. Yield: 67%. 1H NMR (ppm, $CDCl_3$): δ 8.06–7.23 (br, 10H), 4.62 (br, 1H), 2.99 (br, 4H), 2.5-0.5 (br). Anal. Calcd.: C, 73.57; H, 7.69; N, 1.51. Found: C, 73.39; H, 7.64; N, 1.35.

PCA

Following the general polymerization procedure, **M1** (0.5 equiv), **M2** (0.05 equiv), and **M3** (0.45 equiv) were used in this polymerization to obtain a red powder. Yield: 67%. 1H NMR (ppm, $CDCl_3$): δ 8.23-7.22 (br, 10H), 4.644 (br, 1H), 3.947 (br, 1H), 3.020 (br, 4H), 2.50–0.66 (br). Anal. Calcd.: C, 75.28; H, 7.49; N, 2.04. Found: C,

75.39; H, 7.44; N, 2.15.

PCB

PCA (200 mg) was dissolved in 20 mL toluene, and excess HCl solution was added slowly. The mixture was vigorously stirred for 2 days at 80 °C. The polymers were collected by following the general polymerization procedure to gain a red powder. Yield: 81%. 1H NMR (ppm, $CDCl_3$): δ 8.23–7.22 (br, 10H), 4.654 (br, 1H), 3.950 (br, 1H), 3.025 (br, 4H), 2.50–0.66 (br). Anal. Calcd.: C, 74.84; H, 7.20; N, 2.13. Found: C, 74.79; H, 7.44; N, 2.15.

3.3 Results and Discussion

3.3.1 Syntheses and Chemical Characterization

As outlined in Scheme 3.1, two monomers **M1** and **M2** based on carbazole moieties were prepared from 2,7-dibromo-9- (heptadecan-9-yl)-9H-carbazole (**1**) and 2,7-dibromo-carbazole (**4**) moieties.[79] In addition, **M3** based on dithienothiophene was prepared from 3,5-didecanyldithieno[3,2-b:2'3'-d]thiophene[68](**5**) using a reduction procedure and followed by dibromination, which were described by Coppo et al.[43] The electron-donating unit of compound 5 was prepared according to the literature procedures. Monomers **M1**–**M3** were satisfactorily characterized by 1H NMR, 13C NMR, MS spectroscopies, and elemental analyses. Polymers **PCC**, **PCA** and **PCB** were prepared successfully via Suzuki coupling, where **PCC** was produced

by **M1** and **M3**; **PCA** was synthesized by the copolymerization of monomer **M1** with **M2** and **M3**; and **PCB** was prepared by the deprotection of acid in **PCA**. The synthetic procedures towards polymers **PCC**, **PCA** and **PCB** are outlined in Scheme 3.2. Most polymers are partly soluble in organic solvents, such as chloroform, THF, and chlorobenzene at room temperature, and completely soluble in high boiling point solvents (e.g., chlorobenzene) at high temperatures. The yields and molecular weights of polymers **PCC**, **PCA** and **PCB** determined by gel permeation chromatography (GPC) against polysty-rene standards in THF are summarized in Table 3.1. These results show that considerable molecular weights with high yields (50–81% after Soxhlet extractions) were obtained in these copolymers, where the weight-average molecular weights (M_w) of 19,700 to 53,100 with polydispersity indices (PDI = M_w/M_n) of 1.2 to 2.7 were obtained. The thermal stabilities and phase transition temperatures of polymers **PCC**, **PCA** and **PCB** were characterized by thermogravimetric analyses (TGA) and differential scanning calorimetry (DSC) measurements under nitrogen atmosphere, and the thermal decomposition temperatures (T_d) and glass transition temperatures (T_g) are summarized in Table 3.1. It is apparent that all polymers exhibited good thermal stabilities, which showed less than 5% weight loss upon heating to 380 to 428 °C. Regarding DSC experiments, samples (weighted 1–5 mg) sealed in an aluminum pan were operated at 30 to 250 °C

under N_2 atmosphere with a scan rate of 10°C /min. These polymers showed glass transition (T_g) temperatures at 130, 138, and 146 °C for **PCC**, **PCA** and **PCB**, respectively. The T_d and T_g values of **PCB** are higher than those of **PCA**, which were attributed to the rigid polymer networks of **PCB** formed by H-bonds (due to its carboxyl group).

Table 3.1 Molecular Weights, Yields, and Thermal Data of Polymers

Polymer	M_n[a]	M_w[b]	PDI[c]	T_g[d] (°C)	T_d[e] (°C)	Yield (%)
PCC	16600	19700	1.2	130	421	71.4
PCA	19200	53100	2.7	138	380	79.5
PCB	18200	50100	2.7	146	428	70.5

[a]number average molecular weight; [b]weight average molecular weight; [c]polydispersity indices (PDI=M_w/M_n); [d]glass transition temperature; [e]decomposition temperature at 5% weight loss.

3.3.2 Optical Properties

The optical absorption spectra of polymers **PCC**, **PCA** and **PCB** in THF solutions (10^{-6} M) and solid films are shown in Figure 3.1, and their photophysical properties are demonstrated in Table 3.2. As can be seen, the absorption spectra of polymers **PCC**, **PCA** and **PCB** covered broad wavelength ranges (300–600 nm) for both solutions and solid films. In addition, **PCC**, **PCA** and **PCB** possessed similar maximum absorption wavelengths of 445 and 465 nm in THF solutions and solid films, respectively. Due to the π–π stacking of these polymer chains in solids, the

maximum absorption wavelength (465 nm) of **PCC**, **PCA** and **PCB** in solid films was red-shifted about 20 nm in contrast to that (445 nm) of theirsolutions. As shown in Table 3.2, the optical band gaps ($E_{g,}^{opt}$) of 2.24 to 2.25 eV in polymers **PCC**, **PCA** and **PCB** could be determined by the cut-offs of the absorption spectra in solid films. The PL emission spectra of the polymers in solutions and solid films were illustrated in Figure 3.2. The photoluminescence (PL) spectra of polymers **PCC**, **PCA** and **PCB** in THF solutions and solid films were excited at incident wavelengths of 445 and 465 nm, respectively. Interestingly, in comparison with polymer **PCA** in Figure 3.2, the PL spectra of **PCB** containing carboxylic acid moieties were almost quenched in solution and completely quenched in solid film [see Figure 3.2(a,b), respectively]. The PL emission of **PCB** containing carboxylic acid moieties (COOH) is quenched because its dimeric H-bonded structure is formed to shorten the distance between chromophores and to result in the stacking phenomena to quench the PL emission. In other words, the PL quenching phenomena of H-bonds in **PCB** induced by the carboxylic groups might stem from the intersystem crossing from the photo-excited singlet state to the triplet one, where both intramolecular (in solutions) and intermolecular (in solid films) energy transfers along the conjugated backbones might occur. The corresponding optical properties of these polymers in solid films, including the broad and strong optical absorptions, proposed their potential

applications in photovoltaic cells described below.

Table 3.2 Photophysical Data in THF Solutions and Solid Films, Optical Band Gaps, Electrochemical Potentials, Energy Levels and Band Gap Energies of Polymers

Polymer	λ_{abs}, sol[a] (nm)	λ_{abs}, film[b] (nm)	λ_{PL}, film[b] (nm)	$E_{1/2}$[d] (ox)	E_{HOMO} (eV)[e]	E_{LUMO} (eV)[f]	$E_{g,opt}$ (eV)[g]
PCC	445	465	546	0.89	-5.58	-3.34	2.24
PCA	445	465	543	0.91	-5.60	-3.35	2.25
PCB	445	465	-[c]	0.91	-5.60	-3.35	2.25

[a] The absorption spectra were recorded in dilute THF solution at room temperature.

[b] The absorption and PL films were spin-coated from 10 mg/1 mL THF solution.

[c] PL peaks were not detectable due to the PL quenching behavior.

[d] $E_{1/2}$ was the average value of oxidation.

[e] E_{HOMO} = [-($E_{1/2}$ - 0.11) - 4.8] eV where 0.11 V is the value for ferrocene vs. Ag/Ag^+ and 4.8 eV is the energy level of ferrocene below the vacuum.

[f] LUMO = HOMO - $E_{g,opt}$.

[g] Optical band gaps were estimated from the absorption spectra in solid films by using the equation of $E_g = 1240/\lambda_{edge}$.

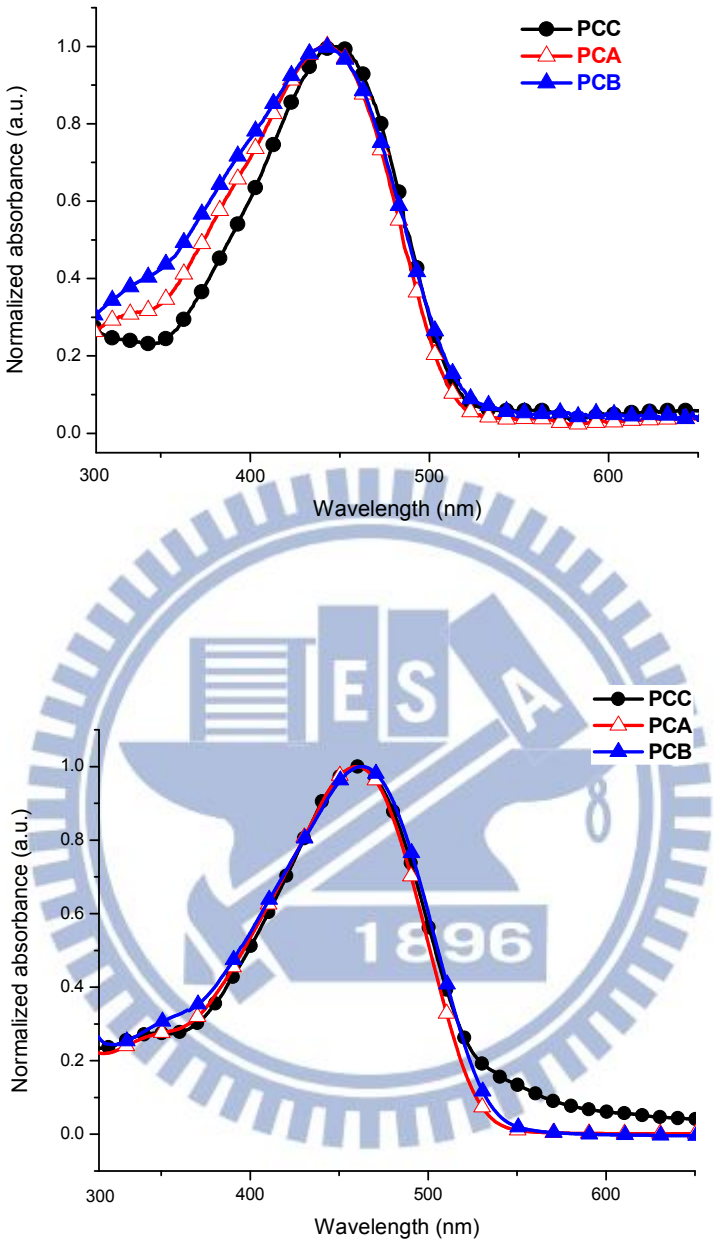

Figure 3.1 Normalized optical absorption spectra of polymers **PCC**, **PCA** and **PCB** in (a) solutions (THF) (10^{-6} M) and (b) solid films (spin-coating from THF solutions).

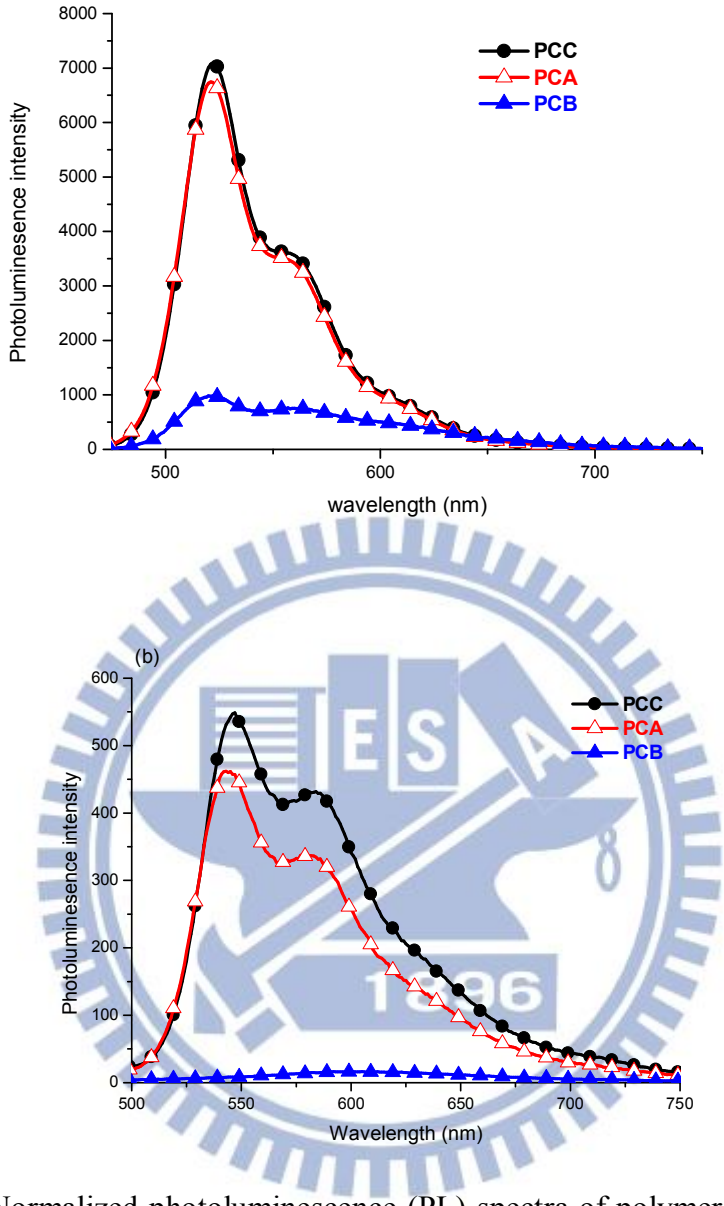

Figure 3.2 Normalized photoluminescence (PL) spectra of polymers in (a) solutions (THF) (10^{-6} M), and (b) solid films (spin-coating from THF solutions).

3.3.3 Electrochemical Properties

The electronic states, that is, highest occupied molecular orbital (HOMO) and lowest unoccupied molecular orbital (LUMO) levels, of the polymers were investigated by cyclic voltammetry (CV) measurements in order to understand the charge injection processes in these polymers and their PSC devices. The oxidation cyclic

voltammograms of **PCC**, **PCA** and **PCB** in solid films and the corresponding electrochromic photos (with a distinct change from orange to black) of are displayed in Figure 3.3(a), where the electrochromic activities in **PCC** and **PCA** were not noticeable to be included due to the lack of H-bonds. The formal potentials and HOMO energy levels (estimated the average oxidation potentials from the electrochemical measurements) are summarized in Table 3.2. As shown in Figure 3.3(a), polymers **PCC**, **PCA** and **PCB** showed one quasi-reversible oxidation process but no detectable reduction behavior. Therefore, the HOMO energy levels of **PCC**, **PCA** and **PCB** can be decided by their quasi-reversible oxidation peaks correspondingly. The moderate onset oxidation potentials of **P1**–**P3** occurred between 0.6 and 1.2 V from which the estimated HOMO levels of -5.58 to -5.60 eV were acquired according to the following equation:[93-94] $E_{HOMO/LUMO}=[-(E_{onset\ (vs\ Ag/AgCl)}-E_{onset\ (Fc/Fc+\ vs\ Ag/AgCl)}-4.8]$ eV, where 4.8 eV is the energy level of ferrocene below the vacuum level and Eonset (Fc/Fc^{+} vs Ag/AgCl) = 0.11 eV. Due to the lack of their reduction peaks, the LUMO energy levels of **PCC**, **PCA** and **PCB** can not be determined, but the LUMO levels can be elucidated by subtracting the optical band gaps ($E_{g,}^{opt}$) from the HOMO energy levels of **PCC**, **PCA** and **PCB**. The electrochemical reductions of polymers **PCC**, **PCA** and **PCB** showed LUMO energy levels at about -3.34 to -3.35 eV, which represent to possess high electron affinities

and also make these polymers suitable donors for electron injection and transporting to PCBM acceptor (with 0.4 eV offsets in LUMO levels regarding PCBM with a LUMO level of -3.75 eV,[95] as shown in Figure 3.4 for the bulk heterojunction polymer solar cell devices.[96] As the potentials of **PCC**, **PCA** and **PCB** were gradually increased to 1.3 to 1.5 V in Figure 3.3(a), due to the higher stability and crystallinity induced by H-bonds, only the electrochromic color of **PCB** changed noticeably from orange (in the neutral state) to black (in the oxidation state) and the color change could be easily detected by naked eye. The absorption spectra (at various applied potentials), and optical feature images along with CIE chromaticity diagram of **PCB** film under neutralization (0.0 V) and oxidation (1.3 V) states are demonstrated in Figure 3.3(b,c), where **PCB** illustrated a hypsochromic absorption and an enhanced absorption in the range of 500 to 800 nm during the oxidation process (from 0.0 to 1.3 V). Therefore, **PCB** is a good candidate for the electrochromic application due to its distinct color change with easy processibility in different solvents (in DCM, THF, and $CHCl_3$).

(a)

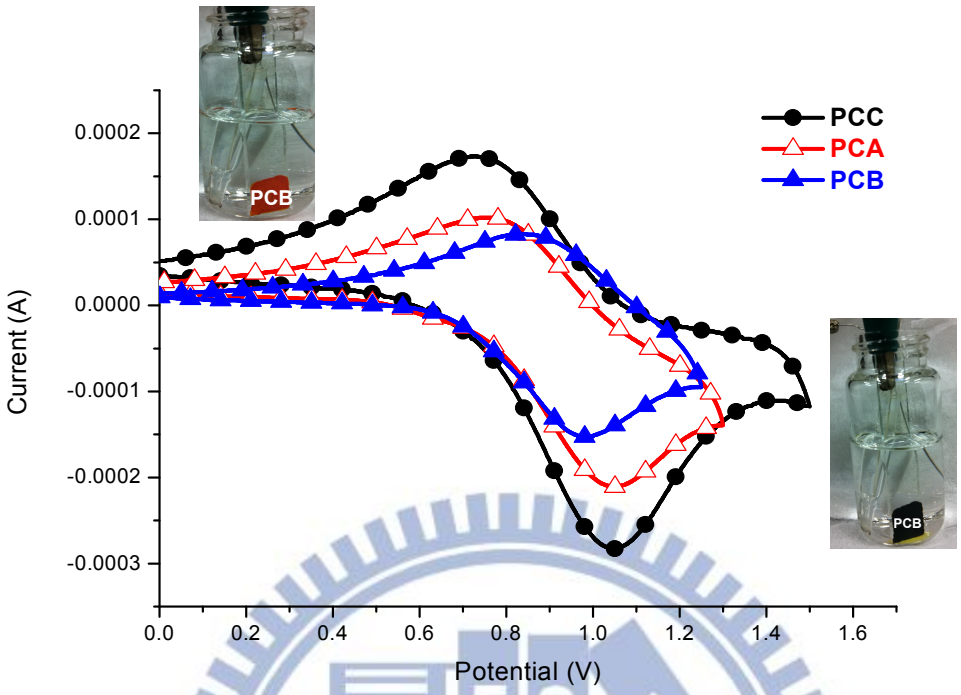
PCC
PCA
PCB
Current (A)
Potential (V)
0.0002
0.0001
0.0000
-0.0001
-0.0002
-0.0003
0.0
0.2
0.4
0.6
0.8
1.0
1.2
1.4
1.6
PCB
PCB

(b)

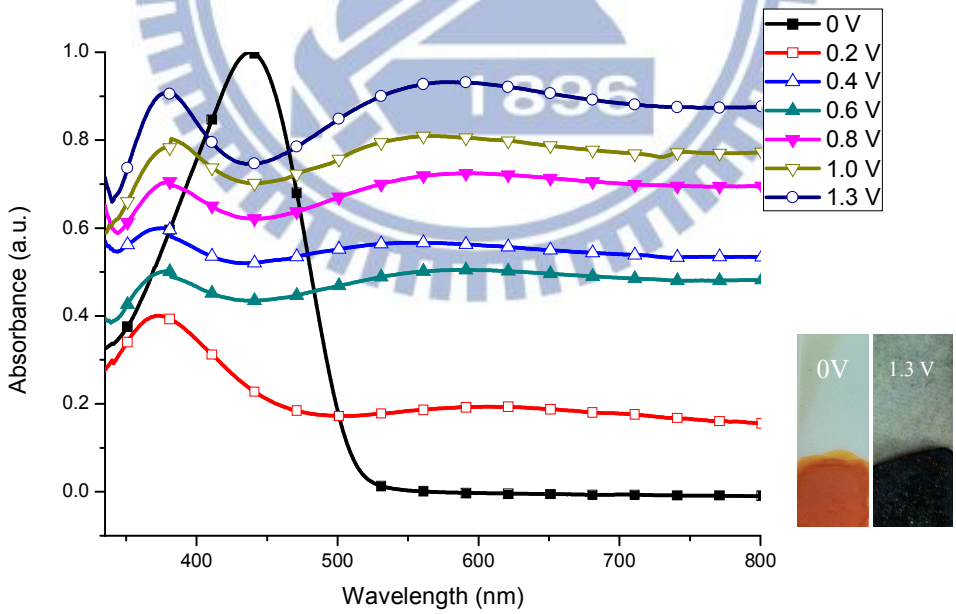
0 V
0.2 V
0.4 V
0.6 V
0.8 V
1.0 V
1.3 V
Absorbance (a.u.)
Wavelength (nm)
1.0
0.8
0.6
0.4
0.2
0.0
400
500
600
700
800
0V
1.3 V

(c)

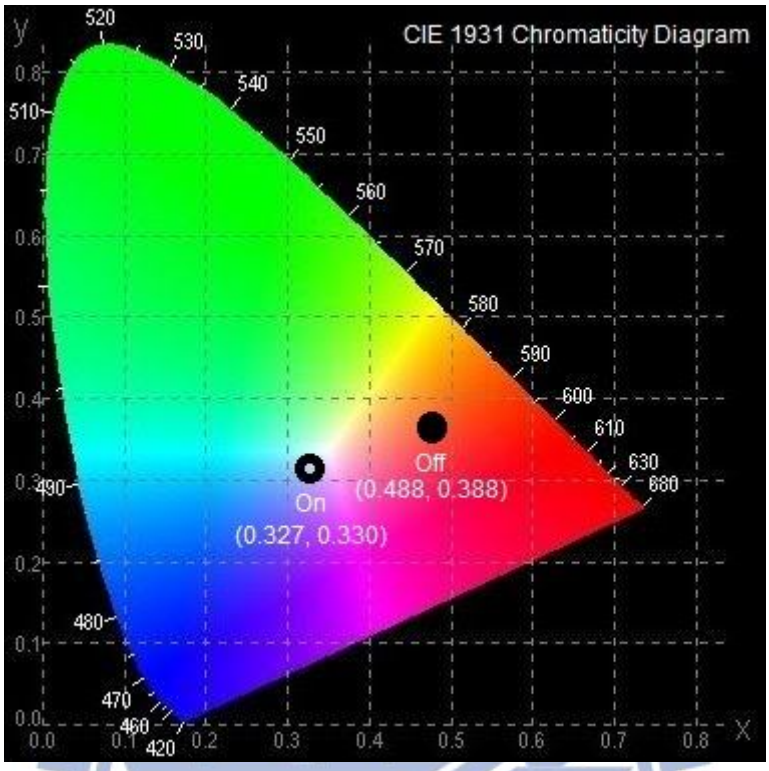

Figure 3.3 (a) Cyclic voltammograms of polymers **PCC**, **PCA** and **PCB** (in solid films) at a scan rate of 100 mV/s, (b) absorption spectra and optical images of **PCB** on ITO at various applied potentials (0 V–1.3 V), (c) CIE chromaticity diagram of **PCB** at ‘‘off’’ (0 V) and ‘‘on’’ (1.3 V) states.

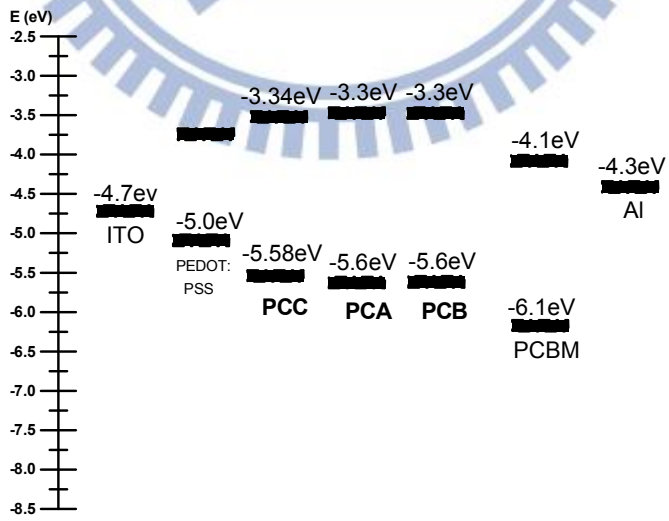

Figure 3.4 Energy band diagram with HOMO/LUMO levels of donor polymers **PCC**, **PCA** and **PCB** in relation to the work functions of ITO and Al.

3.3.4 X-Ray Diffraction (XRD) Analyses

As shown in Figure 3.5(a,b), powder X-ray diffraction (XRD) patterns of polymers **PCC**, **PCA** and **PCB** were acquired to investigate the molecular organization and morphological change. The measurements were proceeded on drop-cast films prepared from 0.5 wt % solutions in THF after the thermal treatment of about 150 °C for 10 min and were then cooled to room temperature. **PCC**, **PCA** and **PCB** after thermal annealing exhibited substantially a primary diffraction feature with a angle at 2θ=2.9Å (corresponding to a large d-spacing value of 20 Å for P1) and 2θ=2.8 Å (corresponding to a large d-spacing value of 21 Å for **PCA** and **PCB**), which were assigned to a distance between the conjugated backbones separated by the long side chains as reported for other similar π-conjugated polymers with long pendants.[97] Moreover, a much stronger (100) XRD characteristic peak of **PCB** (with H-bonds) was observed in contrast to **PCA** (without H-bonds). The XRD data demonstrate that **PCB** possessed a larger crystallinity than **PCA** which was enhanced by the H-bonded interactions. In our previous studies, the crystallinities of the supramolecular polymers were much improved due to the presence of hydrogen bonds, which enhanced the self-assembled behavior and thus to induce higher PCE values of H-bonded polymers.[98 (a)] Moreover, the higher liquid crystalline arrangements of smectic layers can be induced by the formation of supramolecular structures with highly ordered

H-bonds.[98(b,c)] The possible packing motifs of polymers **PCC**, **PCA** and **PCB** in the XRD measurements with three-dimensional layered and π–π stacked arrangements are represented in Figure 3.5(c,d), which show a model that the alkyl side chains stack as bilayered packings within the same layer. On the other hand, the reflections in the wide angle region (corresponding to 3.9–4.5 Å) are related to the π–π stacked distance between the polymer layers,[40,99] which have the similar wide-angle d-spacing values and XRD intensities in all polymers **PCC**, **PCA** and **PCB** to show their almost fixed π–π stacking distances (ca. 3.9–4.5 Å) with comparable crystallinities. The diffraction features of polymers **PCC**, **PCA** and **PCB** were often observed in the XRD patterns of the π-conjugated polymers.[41] Overall, the proposed model can explain the possible structural arrangements of the polymer chains in **PCC**, **PCA** and **PCB**, and the highest crystallinity of **PCB** in the small and large angle regions of XRD pattern (corresponding to the bilayered packings between polymer backbones and the π–π stacked distance between the polymer layers, respectively) was induced by H-bonds.

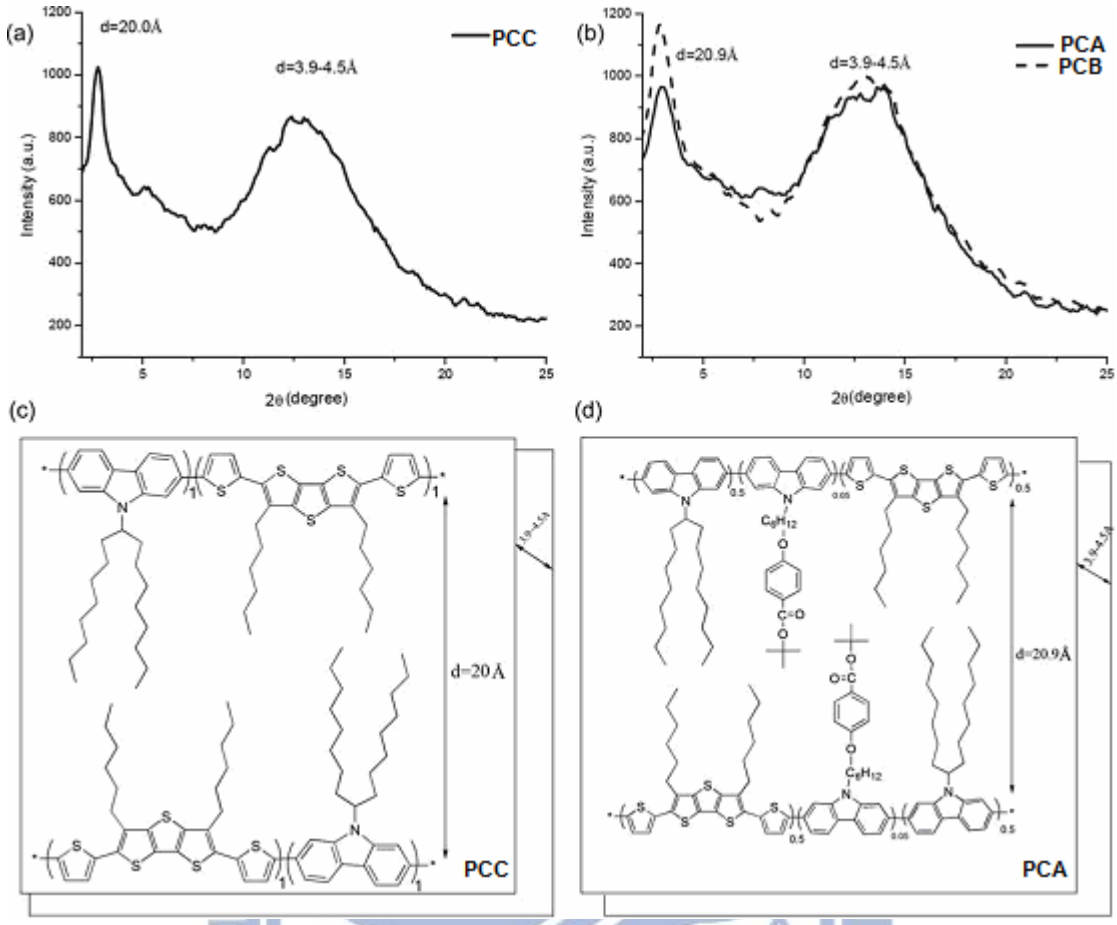

Figure 3.5 Powder X-ray diffraction (XRD) spectra of (a) **PCC** and (b) **PCA** and **Pcb**; and schematic representations of proposed three-dimensional layered and π–π stacked arrangements of (c) **PCC** and (d) **PCA** in their XRD measurements (**PCB** is similar to **PCA**).

3.3.5 Morphology

The AFM topographies of polymer blends (**PCC**, **PCA** and **PCB**: PCBM = 1:1 w/w) were investigated by the casting films of dichloro-benzene solutions as shown in Figure 3.6, where the images were obtained by the tapping mode. Furthermore, the solid films of blended copolymers **PCC** and **PCB** showed a similar surface roughness with moderate root mean square (RMS) values about 18 nm. In comparison with blended polymers **PCC** and **PCB**, blended polymer **PCA** revealed a rather uneven surface with a RMS roughness of 58.6 nm, which was attributed to the aggregation of

polymer chains due to their poor solubilities and lack of H-bonds, and thus to reduce the interface between donor (**PCA**) and acceptor (PCBM) significantly. As shown in Table 3.3, owing to the unfavorable morphology for charge transport offered by poor solubility of **PCA**, the PSC device based on **PCA** gave relatively low current densities (I_{sc}) and thus the lowest PCE value. Therefore, the PCE values of blended polymers (**PCC**, **PCA** and **PCB**: PCBM = 1:1 w/w) are inversely proportional to their RMS roughnesses in AFM. Photovoltaiof 100 mW/cm^2. The preliminarily obtained properties are summarized in Table 3.3, and the typical I–V characteristics of all PSC devices are shown in Figure 3.7. Under monochromatic illumination, the power conversion efficiency (PCE) values of 0.44 to 0.61% were obtained for the PSC devices composedof polymers **PCC**, **PCA** and **PCB** with current density (J_{sc}), open circuit voltage (V_{oc}), and fill factor (FF) in the range of 2.02 to 2.27 mA/cm^2, 0.71 to 0.90 V, and 31 to 33%, respectively. The photovoltaic properties of the PSC devices containing fused dithienothiophene-based polymers **PCC**, **PCA** and **PCB** were dependent on the solubility and film-forming quality of the polymers.

As mentioned in our introductory content, some donor polymers containing dithienothiophene units (designed and prepared by Millefiorini et al.,[84(b)] Gong et al.,[84(a)] and Zhang et al.[87] illustrated lower open circuit voltages (~ 0.8 V) and PCE values (~0.4%) than those of **PCB**, even certain donor acceptor copolymers[83,86]

have worse photovoltaic properties than these developed polymers. Among these PSC devices containing **PCC**, **PCA** and **PCB** in Figure 3.7, polymer **PCB** gave the best performance of PCE = 0.61% with J_{sc} = 2.26 mA/cm^2, V_{oc} = 0.90 V, and FF = 31%. The V_{oc} values are normally related to the HOMO energy levels of the polymers and the LUMO energy levels of the acceptors (e.g., PCBM).[93] Though the HOMO energy levels of **PCC**, **PCA** and **PCB** were similar, the V_{oc} value of **PCB** was noticeably higher than those of **PCC** and **PCA**. Therefore, the highest PCE value of **PCB** is associated with its highest V_{oc} value and highest crystallinity induced by H-bonds.

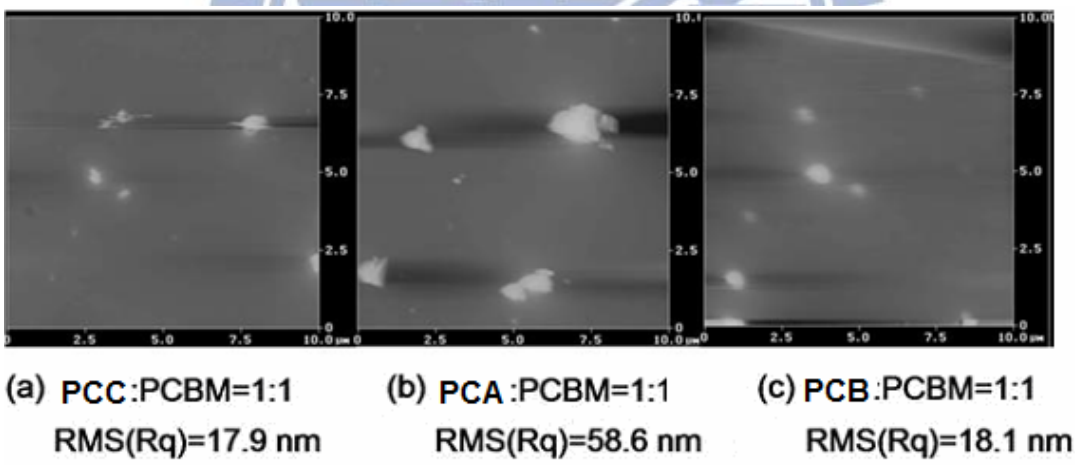

Figure 3.6 AFM images obtained from solid films of Polymer/PCBM (1:1 w/w).

3.4 Conclusions

We have successfully synthesized three dithienothiophene/ carbazole-based conjugated polymers (**PCC**, **PCA** and **PCB**) by Suzuki coupling reaction. Interestingly, **PCC**, **PCA** and **PCB** exhibited reversible electrochromism during the

oxidation processes of cyclic voltammogram studies. Among **PCC**, **PCA** and **PCB**, polymer **PCB** (with H-bonds) revealed the best electrochromic property with the most noticeable color change. In powder X-ray diffraction (XRD) measurements, these polymers exhibited obvious diffraction features indicating distinct bilayered packings between polymer backbones and similar π–π stacking between layers in the solid state. Compared with the XRD data of **PCA** (without H-bands), H-bonds of **PCB** induced a higher crystallinity in the small angle region (corresponding to a higher ordered bilayered packings between polymer backbones), but with a similar crystallinity in the wide angle region indicating a comparable π–π stacking distance between layers. The potential applications of **PCC**, **PCA** and **PCB** in bulk heterojunction photovoltaic solar cells (PSCs) were further investigated, where the PSC device containing **PCB** blended with PCBM (by a weight ratio of 1:1) had the optimum power conversion efficiency (PCE) up to 0.61% (with J_{sc} = 2.26 mA/cm^2, FF = 29.8%, and V_{oc} = 0.90 V). Due to the H-bonded effects, polymer **PCB** possessed higher thermal decomposition temperature (T_d), glass transition temperature (T_g), RMS smoothness, open circuit voltage (V_{oc}), and PCE value than **PCA**. These polymers demonstrate a novel family of conjugated polymers along the path toward achieving the electrochromic and PSC applications.

Chapter 4

Synthesis and Study of Novel Supramolecular Nanocomposites Containing Aryl-Imidazo-Phenanthroline-Based Metallo-Polymers (H-Donors) and Surface-Modified ZnO Nanoparticles (H-Acceptors)

*Four novel metallo-polymers (**P1-P4**) containing aryl-imidazo-phenanthrolines (AIP) ligands (incorporated with phenyl and fused-thiophene cores) were synthesized and characterized. Interestingly, **P1-P4** exhibited electrochromism during the oxidation processes of cyclic voltammogram studies. In addition, **P1-P4** were blended with surface-modified pyridyl-ZnO nanoparticles (**ZnOpy** as proton acceptors) to form nanocomposites, where **P3-P4** were functionalized with carboxylic acid pendants (as proton donors) on the polymer backbones to study for the H-bonded effects on surface-modified **ZnOpy** nanoparticles. In order to investigate the nanocomposites containing metallo-polymers **P1-P4** and surface-modified **ZnOpy** nanoparticles, nanocomposites **P1-P4**/**ZnOpy** were characterized by UV-visible (UV) absorption spectra, Fourier transform infrared (FTIR), photoluminescence (PL) spectra, time-resolved photoluminescence decays, X-ray diffraction (XRD) measurements, and*

transmission electron microscopy (TEM) analyses. In contrast to nanocomposites ***P1/ZnOpy*** *and* ***P2/ZnOpy****, higher crystallinities with a distinct layered-structure of H-bonded nanocomposites* ***P3/ZnOpy*** *and* ***P4/ZnOpy****n in XRD measurements were induced by the introduction of surface-modified* ***ZnOpy*** *nanoparticles to metallo-polymers* ***P3*** *and* ***P4****, correspondingly. Furthermore, due to the supramolecular interactions of surface-modified* ***ZnOpy*** *nanoparticles with metallo-polymers* ***P3-P4****, TEM images verified that* ***ZnOpy*** *nanoparticles were more homogeneously distributed in nanocomposites* ***P3-P4/ZnOpy*** *(with H-bonds) than those in* ***P1-P2/ZnOpy*** *(without H-bonds), respectively.*

4.1 Introduction

Metal-ligand coordination seems to be particularly attractive in past few decades because of searching for new smart materials.[40-42] In recent years, the researches on supramolecular metallo-polymers applied to electro-optical materials have been commonly conducted, because the advantages of these materials, such as easy processability, cheap fabrication, rapid coordination, and tunability of the optical band gap, can promote long-range electrons or energy transfers.[43] Supramolecular metallo-architecture is formed with coordination ability of transition metal ions and chelating ligands because of their self-recognition and self-assembly.[44-46] Moreover,

metal-ligand complexes realized ideal conditions from self-assembly to form the kinetically labile but nevertheless thermodynamically stable bonds.[47] In the meanwhile, metallo-polymers are also good candidates to study for their electrochromic properties during the redox processes.[48-49] 2,2':6',2''-Terpyridine(terpy) and bipyrdine (bpy) derivatives have been utilized recently for multinuclear supramolecular interactions.[50-52,100] In this context, bipyrdine derivatives (i.e., 1H-imidazo[4,5-f][1,10]phenanthrolines)[54] with metal-ligand coordination seem to open an alternative path to produce conjugated polymers, and aryl-imidazo-phenanthroline ligands are ideally suitable for the construction of coordination polymers. Additionally, the easy synthetic access of aryl-imidazo-phenanthroline ligands offers the construction of perfect rods or dendrimers in coordination polymers. 1H-Imidazo[4,5-f][1,10]phenanthroline is one of the metal-ligand combination units that have been of particular importance for the construction of metallo-supramolecular polymers. During the process of light emission in the fully conjugated metallo-polymers, it was confirmed that the phenomenon of metal to ligand charge transfer (MLCT) occurred in 1H-imidazo[4,5-f][1,10]phenanthroline-Ru(II) moieties. A series of aryl-imidazo-phenanthrolines-Ru(II) metallo-polymers, including benzene[54b] and fused dithiophene[55] units as building blocks, were constructed by self-assembled

reactions. The transport of energy and electrons within nanoscale ordered materials is significant to optoelectronics. It needs to control over both of their physical and chemical properties in the self-assembled organization. Nanocomposite systems are that combine the favorable features of, for example, fullerenes and porphyrins as electron acceptors and donors, respectively.[49] They have received interest in the areas of light-induced electron-transfer chemistry and solar energy conversion.[56] Common electron donor-acceptor systems are based on covalent linkages. However, much less is, known about noncovalent electron donor-acceptor nanocomposites and the function of the intervening spacers.[54] Compared with other intermolecular forces, such as van der Waals, π-π stacking, or Coulombic interactions, hydrogen bonds are particularly attractive as they are directional and do not possess electronic energy levels that interfere with those in materials for organic electro-optical applications.[55-56] Therefore, that great efforts have been expended toward the preparation and characterization of photo- and electro-active noncovalent assemblies based on hydrogen bonds (H-bonds). Herein, we design H-bonded interactions between pyridyl surface-modified **ZnOpy** nanoparticles (**ZnOpy** as proton acceptors) and metallo-polymers (**P3**-**P4** as proton donors) (Fig. 1). Because supramolecular interactions (H-bonds) between **ZnOpy** and metallo-polymers turn the organic and inorganic interfaces into homogeneous dispersion, electron and hole separations are

improved to enhance electric translation and reduce electric recombination. The environmentally friendly and low-cost **ZnO** nanoparticles offer a new perspective candidate towards 'green electricity'. By mixing **ZnOpy** nanoparticles as proton acceptors, i.e., a substance with a higher affinity with the polymer, it is possible to break up the excitions by transferring the electrons from the metallo-polymers onto the electron acceptors.[102-105]

4.2 Experimental Section

4.2.1 Materials

All chemicals and solvents were used as received. The rubipyridine (Rupby), 1,10-phenanthroline-5,6-dione,[54] 2,5-bis(octyloxy)benzene-1,4-dialdehyde,[56] and 3,5-dihexyldithieno[3,2-*b*:2′3′-*d*]thiophene-2,6-dialdehyde[55] were prepared according themicals and o the reported literature procedure. The synthetic routes of ligands **L1-L2** and metallo-polymers **P1-P4** are shown in Scheme 1, and the synthetic procedures of their intermediates are described. Csolvents were reagent grades and purchased from Aldrich, ACROS, TCI, and Lancaster Chemical Co. Toluene, N,N-Dimethylformamide, and diethyl ether were distilled to keep anhydrous before use. Furthermore, **ZnO** nanoparticles were synthesized and surface-modified with pyridyl surfactants (**ZnOpy**) to be ca. 3-4 nm.[105]

4.2.2 Ligand synthesis

4.2.2.1.

2-(4-(1H-Imidazo[4,5-f][1,10]phenanthrolin-2-yl)-2,5-bis(octyloxy)phenyl)-1*H*-imidazo[4,5-*f*][1,10]phenanthroline (L1)

A mixture of 1,10-phenanthroline-5,6-dione (211.2 mg, 1.0 mmol), 2,5-bis(octyloxy)benzene-1,4-dialdehyde[18] (218.1 mg, 1.0 mmol), ammonium acetate (1557.3 mg, 20.2 mmol) and glacial acetic acid (30 mL) was refluxed for 2h, then cooled to room temperature. After dilution with water, a yellow precipitate was obtained. The crude product was washed with water and acetone. Yield: 81%. ^{1}H NMR (300 MHz, DMSO-d_6, δ): 9.01 (d, J = 6.01Hz, 4H), 8.91 (d, J = 6.81Hz, 4H), 8.17 (s, 2H), 7.81 (d, J = 3.81Hz, 4H), 4.30 (t, 4H), 1.91 (4H), 1.51 (d, 4H), 1.25 (m, 8H), 1.01 (m, 16H), 0.52 (m, 3H). ^{13}C NMR (75 MHz, DMSO-d_6) δ 152.91, 150.02, 146.32, 144.61, 136.44, 126.89, 123.51, 117.56, 112.53, 69.23, 31.91, 29.71, 29.41, 26.01, 22.81, 14.12. Mass spectrometry (MS): m/z 771.06 ($[M]^+$), found m/z 772.0. Element Anal. Calcd for $C_{44}H_{42}N_8O_2$: C, 68.63 H, 6.92 N, 13.67. Found: C, 68.55 H, 6. 68 N, 13.52.

4.2.2.2.

2-(4-(1H-Imidazo[4,5-f][1,10]phenanthrolin-2-yl)-3,5-(dihexyldithieno [3,2-*b*:2′3′-*d*]thioeno)-1*H*-imidazo[4,5-*f*][1,10]phenanthroline (L2)

A mixture of 1,10-phenanthroline-5,6-dione (215.3 mg, 1.0 mmol), 3,5-dihexyldithieno[3,2-*b*:2′3′-*d*]thiophene-2,6-dialdehyde (223.2 mg, 1.0 mmol), ammonium acetate (1568.9 mg, 20.4 mmol) and glacial acetic acid (30 mL) was refluxed for 2h. The reaction procedure was the same as that of **L1**. The crude product was washed with water and acetone. Yield: 65%. ^{1}H NMR (300 MHz, DMSO-d_6, δ 9.01 (d, 4H), 8.91 (d, 4H), 7.81 (d, 4H), 2.5(4H), 1.89 (4H), 1.32 (16H), 0.96 (m, 6H). ^{13}C NMR (75 MHz, DMSO-d_6) δ 154.11, 150.01, 148.01, 141.52, 138.32, 136.44, 135.21, 133.62, 130.21, 129.01, 12801, 127.49, 126.32, 125.78, 12421, 122.91, 121.51, 31.91, 29,01, 22.81, 21.31, 14.11. Mass spectrometry (MS): *m*/*z* 801.7 ([M]$^{+}$), found *m*/*z* 801.3. Element Anal. Calcd for $C_{46}H_{40}N_8S_3$: C, 68.97 H, 5.03 N, 13.99. Found: C, 68.82 H, 5.19 N, 14.02.

4.2.3. General Synthetic Procedure for Metallo-Polymers P1-P4

The synthetic routes and chemical structures of metallo-polymers are shown in Scheme 4.1 and Figure 4.1, respectively. All of the polymerization procedures were carried out through the metal-ligand coordination reactions.

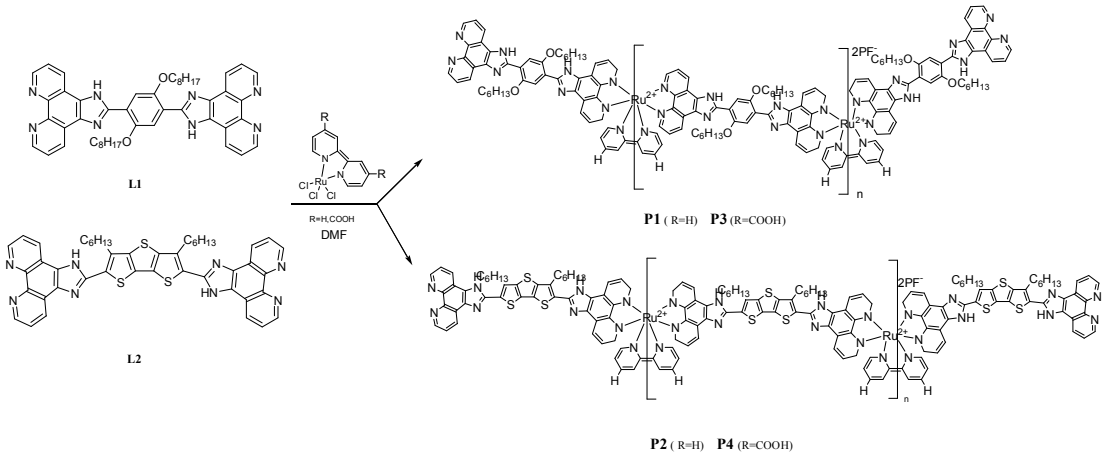

Scheme 4.1. Synthesis of ligands **L1-L2** and metallo-polymers **P1-P4**.

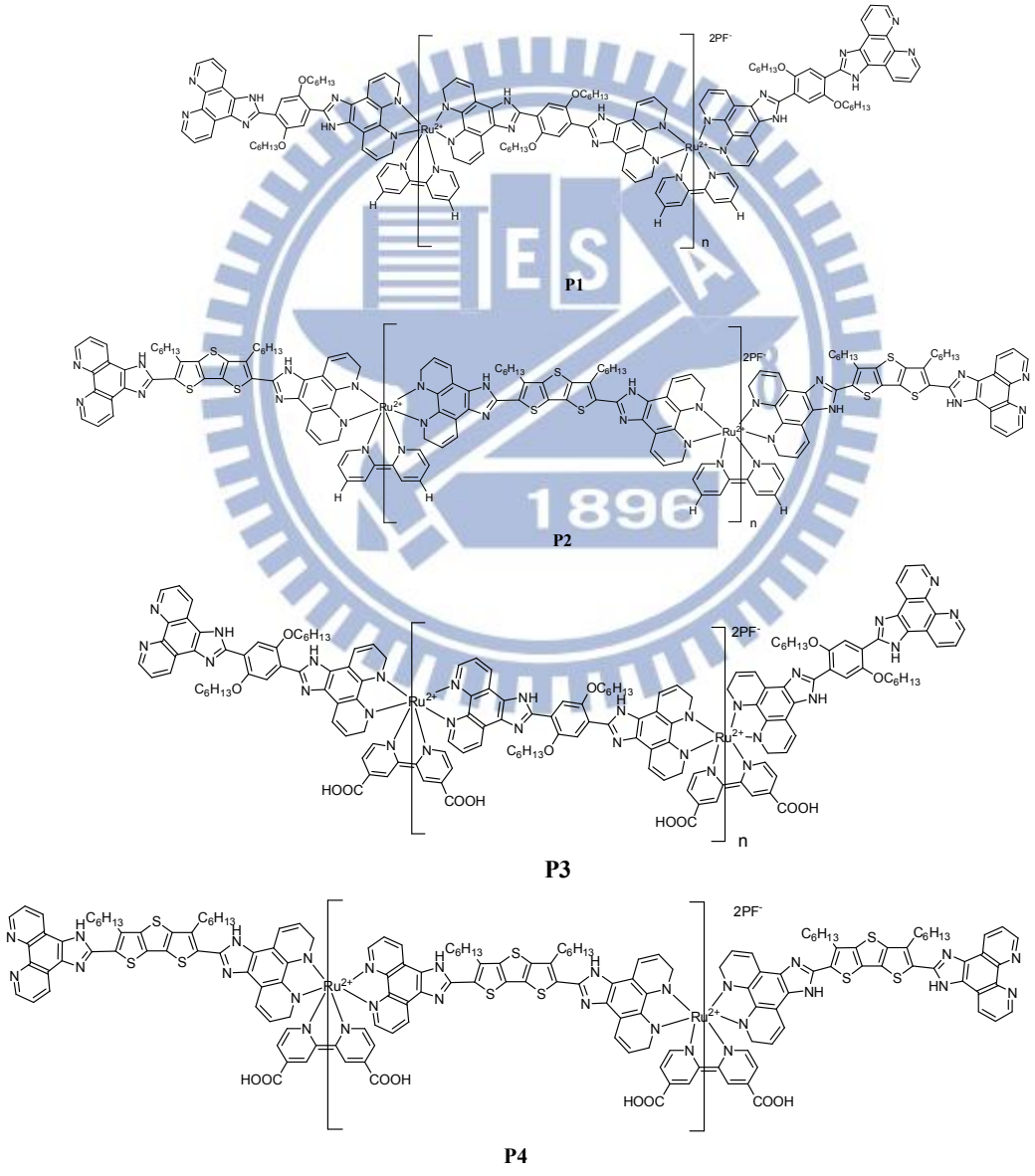

Figure 4.1 Chemical structures of metallo-polymers **P1-P4**.

4.2.3.1. P1

To a solution of ligand **L1** (1mmol) in 10 ml of DMF, Rubpy (1mmol) in DMF (10ml) was added. The resulting solution was heated to react at 100 °C under a nitrogen atmosphere. After stirring for 24 h, excess NH_4PF_6 was added into the hot solution. The resulting solution was poured into water and the precipitate obtained was purified by repeated precipitations using acetone and water. The polymer was dried under vacuum at 60 °C for 24 h and collected as black solids. Yield: 85%. ^{1}H NMR spectrum of metallo-polymer (**P1**) is similar to that of ligand (**L1**) but broader than peak of ligand. (see Figure 4.2) The phenomenon reveals a metallo-polymer (**P1**) was made. ^{1}H NMR (300 MHz, DMSO-d_6, δ): 9.01 (br, 4H), 8.91 (br, 4H), 8.17 (br, 2H), 7.81 (br, 4H), 4.30 (br, 4H), 1.91 (br, 4H), 1.51 (br, 4H), 1.25 (br, 8H), 1.01 (br, 16H), 0.52 (br, 3H).

4.2.3.2. P2

To a solution of ligand (**L2**) (1mmol) in 10 ml of DMF, Rubpy (1mmol) in DMF (10ml) was added. The resulting solution was heated to react at 100 °C under nitrogen. After stirring for 24 h, excess NH_4PF_6 was added into the hot solution. The resulting solution was poured into water and the precipitate obtained was purified by repeated precipitations using acetone and water. The polymer was dried under vacuum at 60

°C for 24 h and collected as black solids. Yield: 65%. ^{1}H NMR spectrum of metallo-polymer (**P2**) is similar to that of ligand (**L2**), but **P2** has broader peaks than ligand **L2** (see Figure 4.3), which reveals the formation of metallo-polymer **P2**. ^{1}H NMR (300 MHz, DMSO-d_6, δ): 9.01 (br, 4H), 8.91 (br, 4H), 7.81 (br, 4H)

4.2.3.3. P3

The procedure is analogous to that described for **P1**. Yield: 70%. ^{1}H NMR spectrum of metallo-polymer (**P3**) is similar to that of ligand (**L1**), but **P3** has broader peaks than ligand **L1** (see Figure 4.2), which reveals the formation of metallo-polymer **P3** with worse solubility due to the carboxylic acid pendants. ^{1}H NMR (300 MHz, DMSO-d_6, δ): 9.01 (br , 4H), 8.91 (br, 4H), 8.17 (br, 2H), 7.81 (br, 4H), 4.30 (br, 4H).

4.2.3.4. P4

The procedure is analogous to that described for **P2**. Yield: 54%. ^{1}H NMR spectrum of metallo-polymer (**P4**) is similar to that of ligand (**L2**), but **P4** has broader peaks than ligand **L2** (see Figure 4.3), which reveals the formation of metallo-polymer **P4** with worse solubility due to the carboxylic acid pendants. ^{1}H NMR (300 MHz, DMSO-d_6, δ): 9.01 (br, 4H), 8.91 (br, 4H), 7.81 (br, 4H).

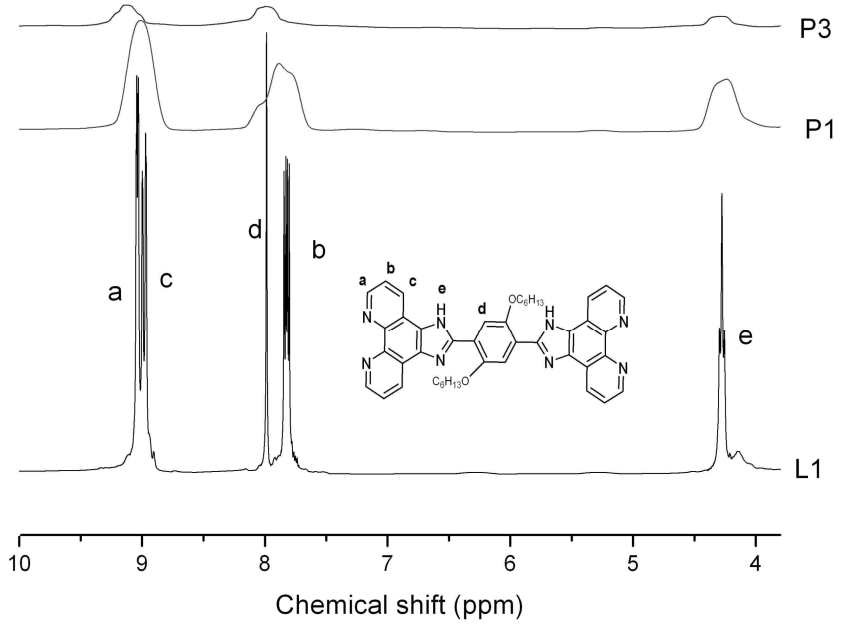

Figure 4.2 ^{1}H NMR spectra (aromatic region) of ligand **L1** and metallo-polymers **P1** and **P3** in DMSO-d_6.

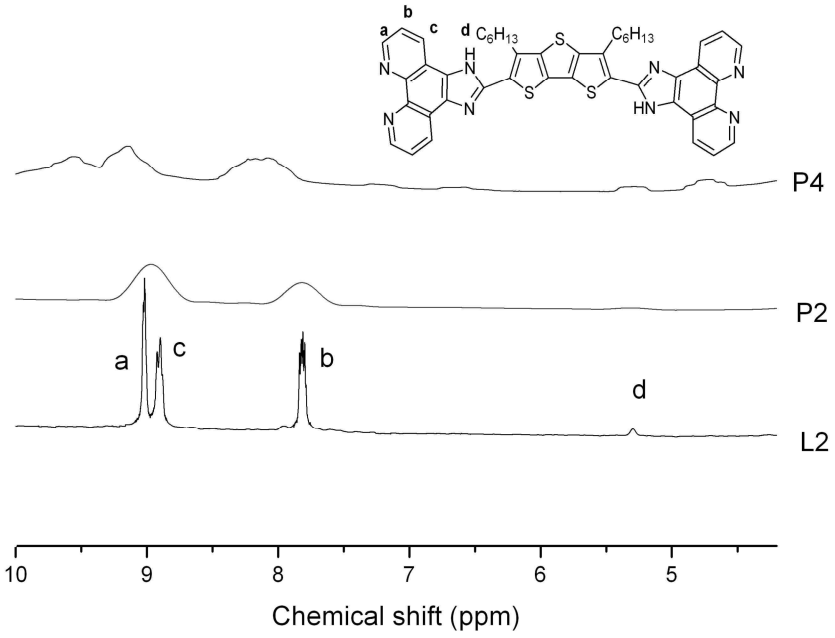

Figure 4.3 ^{1}H NMR spectra (aromatic region) of ligand **L2** and metallo-polymers **P2** and **P4** in DMSO-d_6.

4.2.4. Preparation of Nanocomposites Complexes

As shown in Figure 4.4, all nanocomposites **P1**/**ZnOpy**, **P2**/**ZnOpy**, **P3**/**ZnOpy**, and **P4**/**ZnOpy** were prepared by blending 1 mole **ZnOpy** nanoparticles (**ZnOpy** as proton acceptor) with 1 mole repeating units of metallo-polymers (**P1**-**P4** as proton donors) in the solutions of N,N-Dimethylformamide (DMF), which were self-assembled into supramolecules by evaporating solvents slowly. For example, metallo-polymer **P1** and pyridyl H-acceptor (**ZnOpy**) were dissolved in a DMF solvent and self-assembled into supramolecules by evaporating solvents slowly. When the solvent were evaporated completely, a brown nanocomposites of **P1**/**ZnOpy** was formed. A series of nanocomposites **P1**/**ZnOpy**, **P2**/**ZnOpy**, **P3**/**ZnOpy** and **P4**/**ZnOpy** were also provided.

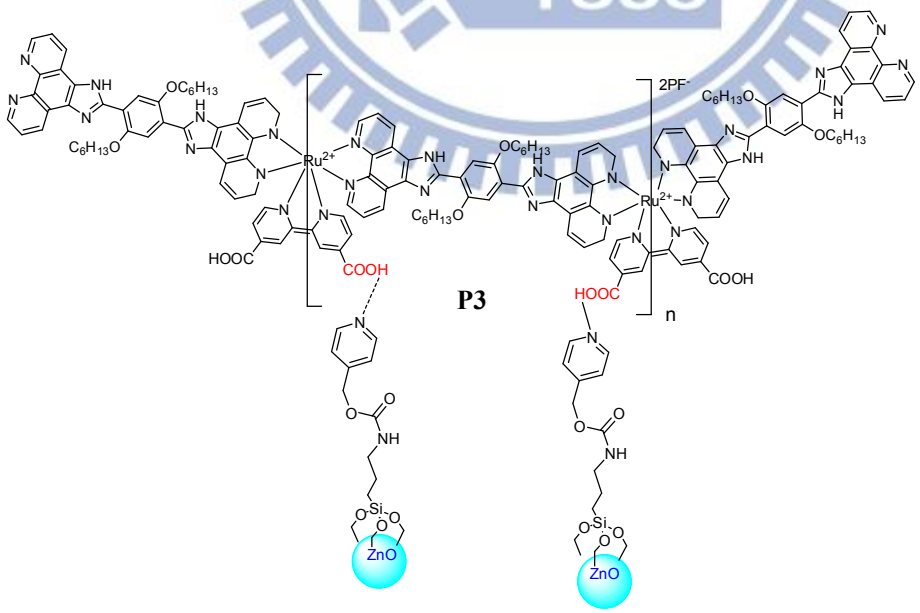

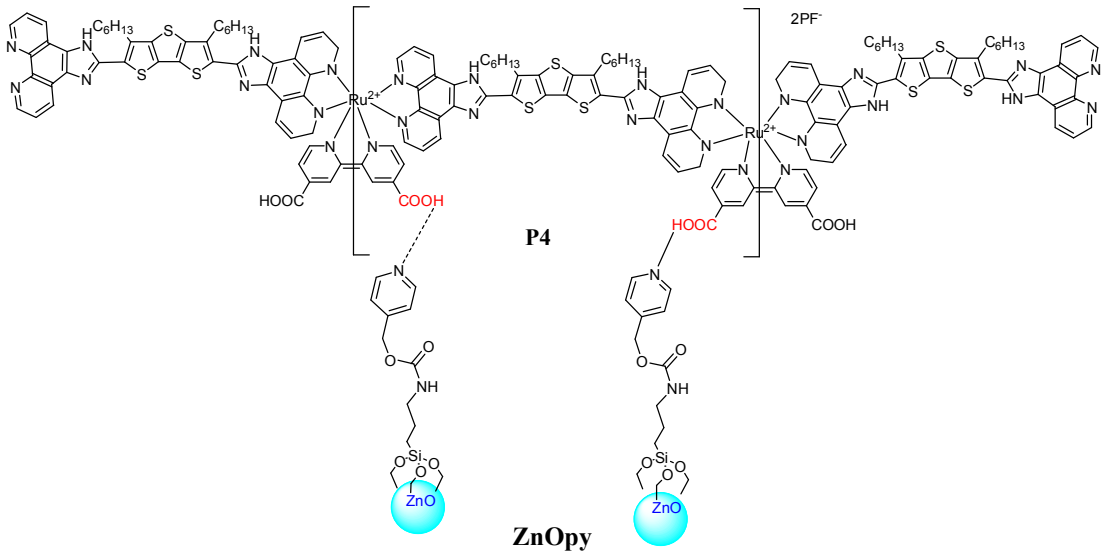

Figure 4.4 Supramolecular structures of H-bonded nanocomposites **P3/ZnOpy** and **P4/ZnOpy**.

4.2.5. Measurements and Characterization

^{1}H NMR spectra were recorded on a Varian Unity 300 MHz spectrometer using DMSO-*d6* solvents. Transition temperatures were determined by differential scanning calorimetry (DSC, Perkin-Elmer Pyris 7) with a heating and cooling rate of 10 °C/min. Thermogravimetric analyses (TGA) were conducted with a TA instrument Q500 at a heating rate of 10 °C/min under nitrogen. UV-visible absorption and photoluminescence (PL) spectra were recorded in dilute N,N-Dimethylformamide (DMF) solutions (10^{-5} M) on a HP G1103A and Hitachi F-4500 spectrophotometer, respectively. Solid films of UV-vis and PL measurements were spin-coated on a quartz substrate from DMF solutions with a concentration of 10 mg/mL. Cyclic voltammetry (CV) measurements were performed using a scanning rate of 100 mV/s

on a BAS 100 electrochemical analyzer, which was equipped with a standard three-electrode electrochemical cell in a 0.1 M tetra-n-butylammonium perchlorate (TCI) solution (in DMSO) at room temperature. A platinum wire as the counter electrode, and a silver wire as the quasi-reference electrode were used. Ag/AgCl (3M KCl) electrode was served as a reference electrode for all potentials quoted herein. During the CV measurements, the solutions were purged with nitrogen for 30s, and the redox couple ferrocene/ferrocenium ion (Fc/Fc^{+}) was used as an external standard. The corresponding HOMO levels in polymer solutions of **P1-P4** could be calculated from $E_{ox/onset}$ values of the electrochemical experiments (but no reduction curves, i.e., no $E_{red/onset}$ values and LUMO levels, were obtained in the CV measurements). Each onset potential in the CV measurements was defined by the intersection of two tangents drawn at the rising current and background current. Infrared spectra (FT-IR) were investigated by a Perkin-Elmer Spectrum 100 instrument. Synchrotron powder X-ray diffraction (XRD) measurements were performed at beamline BL13A of the National Synchrotron Radiation Research Center (NSRRC), Taiwan, where the wavelength of X-ray was 1.026503 Å. TEM studies were performed using a JEOL 2010 instrument under an accelerlation voltage of 200 kV. The samples were prepared by dispersing into DMF and then dropping the dispersion onto the TEM copper grids. UV-visible absorption and photoluminescence (PL) spectra were recorded in dilute

DMF solutions (10^{-6} M) on a HP G1103A and Hitachi F-4500 spectrophotometer, respectively. Time-resolved photoluminescence (TRPL) spectra were measured using a home-built single photon counting system. Excitation was performed using a 375 nm diode laser (Picoquant PDL-200, 50 ps fwhm, 2 MHz). The signals collected at the excitonic emissions of solutions (λ = 420 nm) were connected to a time-correlated single photon counting card (TCSPC, Picoquant Timeharp 200).

4.3 Results and Discussion

4.3.1. Syntheses and chemical characterization

Metallo-polymers **P1-P4** were prepared successfully via coordination with a mixture of ligands **L1** and **L2**. The integrated of ^{1}H NMR spectra reveal a facile result to distinguish the well-defined main-chain metallo-polymeric structures which were constructed by different ligands. Proton NMR spectra of ligands **L1-L2** and metallo-polymers **P1-P4** in DMSO are illustrated in Figures 4.2 and 4.3, which show proton peaks in the aromatic regions of ligands and metallo-polymers. As a result of metallo-polymerization, broadened signals of ligands were observed. Ligands **L1-L2** and metallo-polymers **P1-P4** were satisfactorily characterized by ^{1}H NMR spectra. The thermal stabilities of metallo-polymers **P1-P4** were characterized by thermogravimetric analyses (TGA) measurements under nitrogen atmosphere, and the thermal decomposition temperatures (T_d) are in the range of 320-380°C.

4.3.2. UV spectroscopic studies

The absorption spectral data of all metallo-polymers **P1-P4** and ligands **L1-L2** in DMF solutions (10^{-6} M) and solid films are summarized in Figure 4.5 and Table 4.1. The absorption wavelengths of metallo-polymers (**P1-P4**) in Figure 4.5 exhibit broad wavelength ranges from 270 nm to 650 nm. Similar to the absorption peaks of ligands (**L1-L2**) *ca.* 280 and 380 nm in Figure 4.5, all short absorption peaks of metallo-polymers (**P1-P4**) in the range of 270-490 nm were due to the $d\pi \rightarrow \pi^*$ transitions. These intramolecular charge transfer (ICT) results show that the maximum absorption wavelengths of **P2** (429 nm) and **P4** (407 nm) are longer than those of polymers **P1** (385 nm) and **P3** (343 nm), respectively, which reflects the longer effective conjugation lengths existing in the extended fused-thiophene-based polymers (**P2** and **P4**). Moreover, the characteristic absorption bands of metallo-polymers (**P1-P4**) in the range of 490 to 560 nm are attributed to the metal-to-ligand charge transfer (MLCT) transition. According Figure 4.5(b), the optical band gaps (in Table 4.1) can be estimated from the absorption spectra in solid films by using the equation of $E_g = 1240/\lambda_{edge}$. As shown in Table 4.1, the bandgaps of metallo-polymers (**P1-P4**) are compared to have the sequence of **P4 < P3** < **P2 < P1** and with the largest value in **P1** and the smallest value in **P4**. Therefore, the bandgaps of metallo-polymers can be reduced by the replacement of phenyl rings (**P1** and **P3**)

with thiophene rings (**P2** and **P4**), and the replacement of the H atoms (**P1** and **P2**) with the COOH groups (**P3** and **P4**).

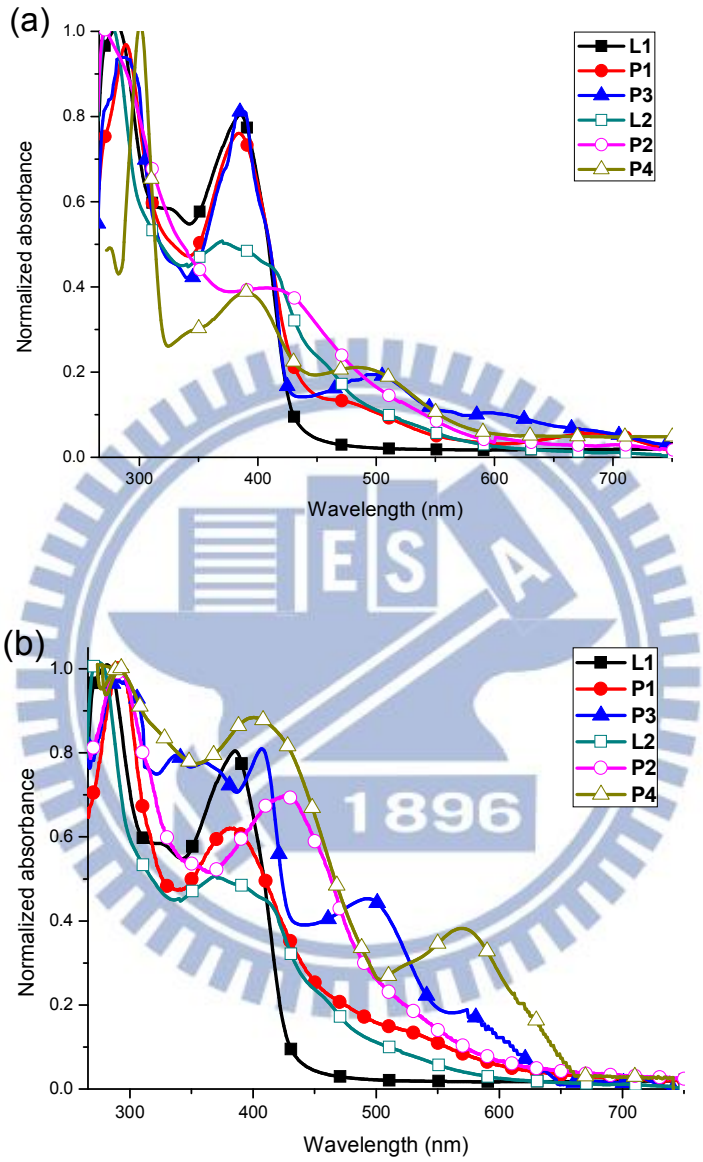

Figure 4.5 Normalized UV-vis spectra of ligands **L1-L2** and metallo-polymers **P1-P4** in (a) DMF solutions and (b) solid films.

Table 4.1

Photophysical Data in DMF Solutions and Solid Films and Electrochemical Potentials, Energy Levels, and Band Gap Energies of Metallo-Polymers **P1**-**P4**[a]

Samples	λ, UV (nm)		Energy level[b]	Energy level	
	Solution	Solid film[a]	E_{HOMO} (eV)[c]	E_{LUMO} (eV)[e]	$E_{g,opt}$ (eV)[d]
L1	285, 384,	281, 385	-	-	2.8
L2	281, 377	275, 378	-	-	2.1
P1	288, 387, 490	292, 385, 517	5.1	2.6	2.5
P2	276, 420, 516	289, 429, 517	5.93	3.93	2.0
P3	286, 385, 506	293, 343, 503	5.91	3.91	2.0
P4	298, 390, 490	286, 407, 572	5.7	3.8	1.9

[a] Spin-coated from DMF solution.

[b] Measured for in thin solid film using tetra-n-butylammonium perchlorate (TCI) as the supporting electrolyte at a scan rate of 100 mV/s.

[c] HOMO = $[-(E_{onset\ (vs\ Ag/AgCl)} - E_{onset\ (Fc/Fc+\ vs\ Ag/AgCl)})-4.8]$ eV where 4.8 eV is the energy level of ferrocene below the vacuum level and $E_{onset\ (Fc/Fc+\ vs\ Ag/AgCl)}$ = 0.4 eV.

[d] Optical band gaps were estimated from the absorption spectra in solid films by using the equation of $E_g = 1240/\lambda_{edge}$.

[e] $E_{LUMO} = E_{HOMO} + E_{g,opt}$.

4.3.3. Electrochemical characterization

The electronic states, i.e. energy levels of the highest occupied molecular orbital (HOMO) and lowest unoccupied molecular orbital (LUMO), of the metallo-polymers were investigated by cyclic voltammetry (CV) in order to understand the charge injection processes in these metallo-polymers. The electrochemical responses of Ru(II) polypyridyl complexes were usually observed due to a metal-centered oxidation, and thus to induce the electrochromic behavior.[106] The oxidation cyclic voltammograms

and corresponding electrochromic photos of metallo-polymers **P1**-**P4** in solid films are displayed in Figure 4.6. The formal potentials, onset potentials, and band gaps, along with the estimated positions of the upper edges of the valence band (HOMO) obtained from the electrochemical measurements are summarized in Table 4.1. The ligands (**L1, L2**) showed no detectable oxidation and reduction behavior, implying that the electrons are difficult to be injected into both ligands (**L1**, **L2**). As shown in Figure 4.6, metallo-polymers **P1**-**P4** showed one irreversible oxidation process but no detectable reduction behavior. Therefore, the HOMO energy levels of **P1**-**P4** can be decided by their irreversible oxidation peaks correspondingly. Due to the lack of their reduction peaks, the LUMO energy levels of **P1**-**P4** can not be determined, but the LUMO levels can be elucidated by subtracting the optical bandgaps from the HOMO energy levels of **P1**-**P4**. As the potential was gradually increased to +2.0 V, the color of the film changed from deep-yellow to charcoal gray during the oxidation process, where the electrochromic behavior was induced by one-electron metal-centered oxidation. However, only irreversible electrochromic behavior could be observed in the oxidation process due to the lack of the reversible oxidation process. Moreover, no electrochromic behavior can be detected for the lack of the reduction process in metallo-polymers **P1**-**P4**.

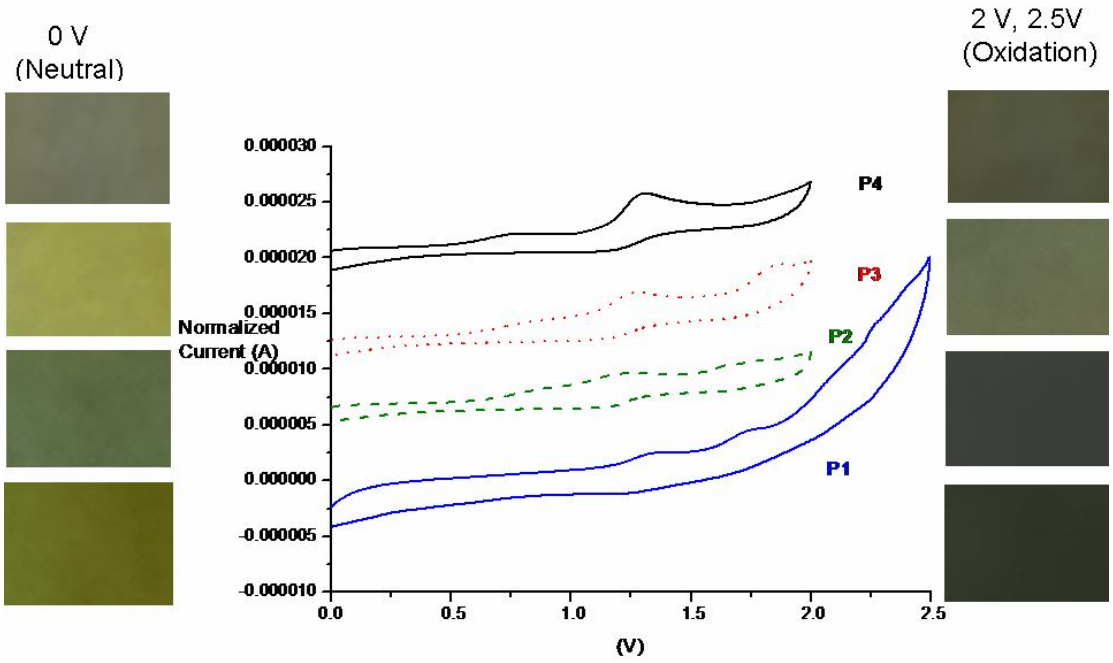

Figure 4.6 Cyclic voltammagrams and electrochromic photos of metallo-polymers **P1-P4** in solid films.

4.3.4. FT-IR spectroscopic studies

The molecular structures of metallo-polymers **P1-P4** could also be confirmed by the FT-IR spectra. For instance, the absorption stretching mode of the carboxylic group in the polymers, which typically appeared at 1710, 1642 cm^{-1}, respectively, was absent in the spectra of metallo-polymers **P3-P4**. H-bonded effects in H-donor metallo-polymers (**P3-P4**) blended with H-acceptor **ZnOpy** nanoparticles were confirmed by FT-IR spectroscopy. The IR spectra of H-acceptor **ZnOpy**, H-donor metallo-polymers **P3-P4**, and their H-bonded nanocomposites **P3-P4**/**ZnOpy**, shown in Figure 4.7, were compared to analyze the formation of H-bonds. In contrast to the

O-H bands at 2665 and 2620 cm^{-1} of pure H-donor polymers **P3** and **P4**, weaker O-H bands were observed at 2513, 2500 cm^{-1} and 1921, 1935 cm^{-1} in H-bonded nanocomposites **P3**/**ZnOpy** and **P4**/**ZnOpy**, respectively. These results are indicative of stronger H-bonds formed between pyridyl groups of H-acceptor **ZnOpy** and acid groups of H-donor metallo-polymers **P3**-**P4** in their H-bonded nanocomposites **P3**-**P4**/**ZnOpy**. On the other hand, C=O stretching vibrations at 1710 and 1642 cm^{-1} in pure metallo-polymers **P3** and **P4** appeared as shoulders at 1736 and 1635 cm^{-1} for H-bonded nanocomposites **P3**-**P4**/**ZnOpy**, respectively. This shows that the carbonyl group is in a more associated state than that in the pure H-donor metallo-polymers **P3**-**P4**, which contains a weaker C=O stretching vibration appeared (at 1710 and 1642 cm^{-1}). All results suggest that H-bonds were generated in the solid state of H-bonded nanocomposites **P3**/**ZnOpy** and **P4**/**ZnOpy**, which is similar to our previous report.[107]

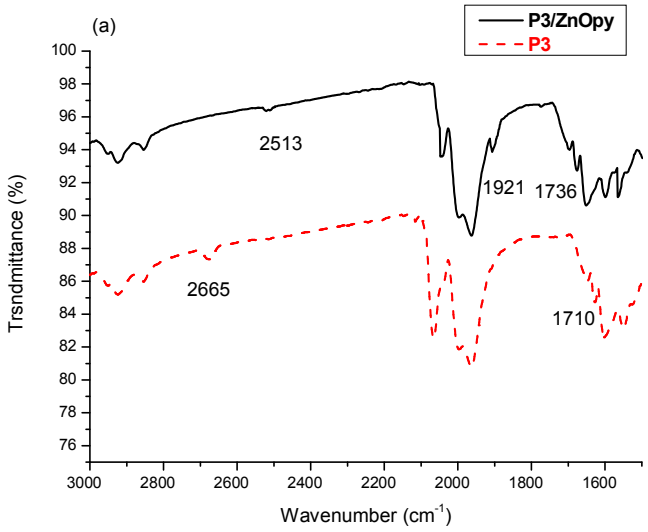

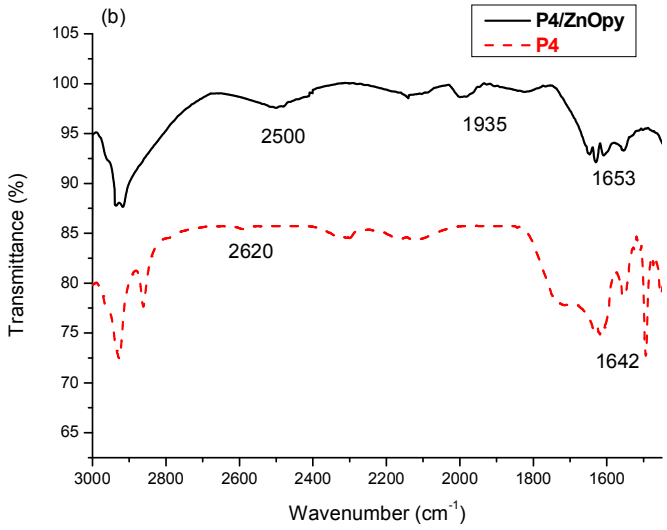

Figure 4.7 FTIR spectra of metallo-polymers (**P3** and **P4**) and nanocomposites (**P3/ZnOpy** and **P4/ZnOpy**).

4.3.5. Time-resolved PL spectroscopic studies

As shown in Figure 4.8, the photoluminescence (PL) spectra of metallo-polymers **P1-P4** and H-bonded nanocomposites **P1-P4/ZnOpy** in solid films were excited at an incident wavelength of 420 nm. Their PL emissions show broad and weak absorptions from 420 to 650 nm which covered all PL ranges of metallo-polymers **P1-P4** and nanoparticle **ZnOpy**. Time-resolved photoluminescence (PL) measurements (i.e., ultrafast emission dynamics), monitored at the wavelength above 420 nm, were performed to give additional information on the charge-transfer dynamics in nanocomposites **P1-P4/ZnOpy** by measuring the fluorescence lifetimes using time-correlated single-photon counting (TCSPC) methodology (Figure 4.9). The apparatus for the TCSPC measurements was described in the literature.[108] As

illustrated in Table 4.2, the measurements revealed that the luminescence lifetime values of nanocomposites **P1-P4/ZnOpy** (Figure 4.9(b)) were 3.8, 5.0, 1.6, and 2.3 ns, respectively, and those of metallo-polymers **P1-P4** were 7.1, 6.9, 7.0, and 7.0 ns, respectively (Figure 4.10a). The faster PL decay of nanocomposites **P1-P4/ZnOpy** than those of metallo-polymers **P1-P4** can be attributed to the quenching behavior from nanoparticle **ZnOpy**. More importantly, improving interfacial contacts by H-bonds between polymers and nanoparticle **ZnOpy**, H-bonded nanocomposites **P3/ZnOpy** and **P4/ZnOpy** have shorter lifetime values (1.6, and 2.3 ns) than nanocomposites **P1/ZnOpy** and **P2/ZnOpy** (3.8, and 5.0 ns) respectively. These results suggest that the excitons are easier to be quenched via the H-bonded interfaces of polymers and nanoparticles, which were also reported as a more rapid charge transfer process from P3HT to CdSe with a surface modification.[109]

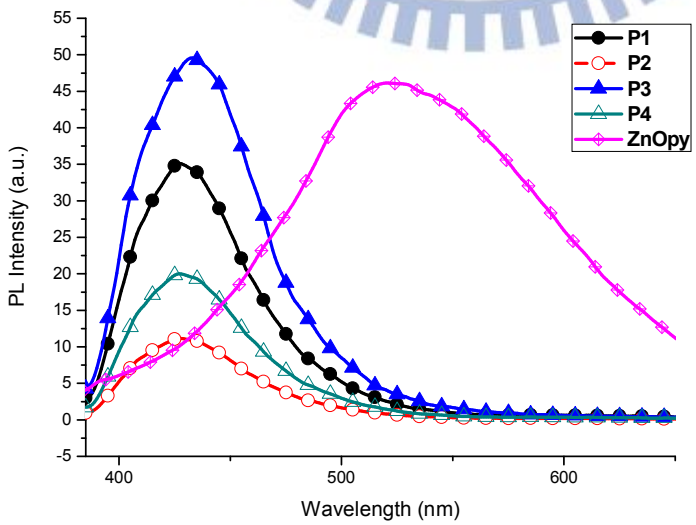

Figure 4.8 PL spectra of metallo-polymers **P1-P4** and nanoparticle **ZnOpy**.

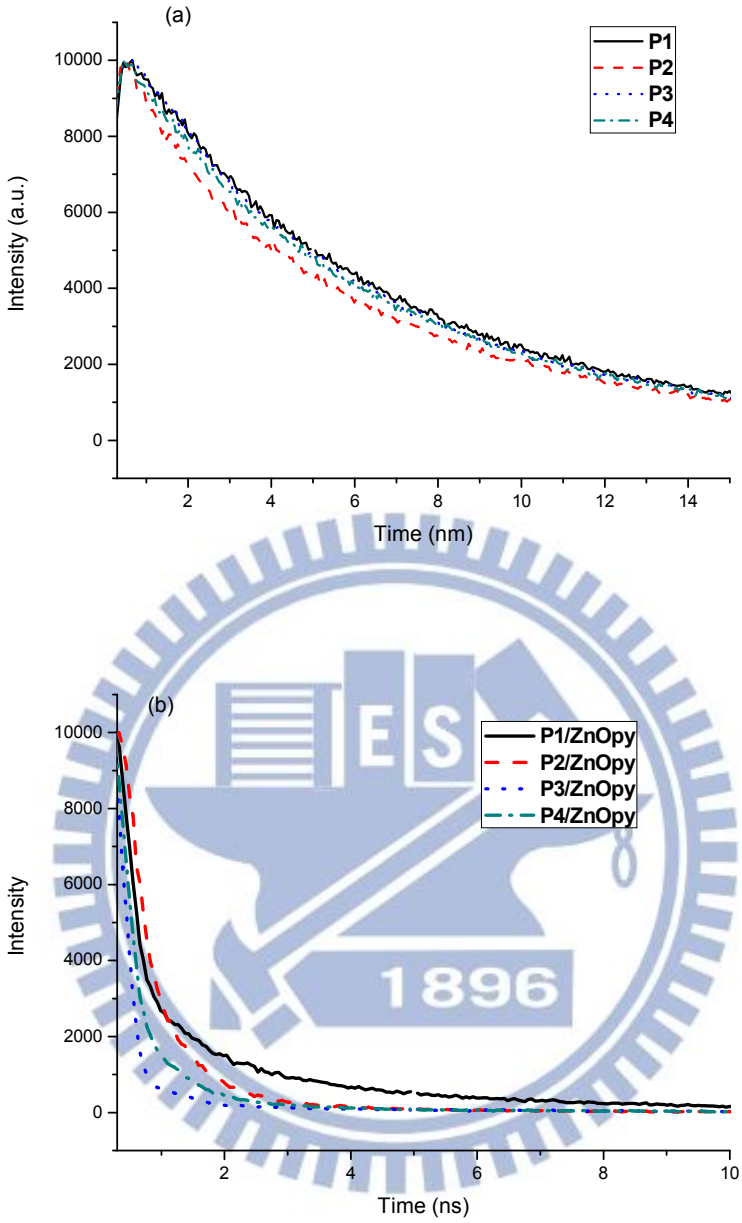

Figure 4.9 Normalized time-resolved photoluminescence decays of (a) metallo-polymers **P1-P4** and (b) nanocomposites **P1/ZnOpy, P2/ZnOpy, P3/ZnOpy**, and **P4/ZnOpy**.

Table 4.2

Fluorescence Lifetimes of Metallo-Polymers **P1-P4** and its Nanocomposites

Sample	**P1**	**P2**	**P3**	**P4**	**P1/ZnOpy**	**P2/ZnOpy**	**P3/ZnOpy**	**P4/ZnOpy**
τ (ns)	7.1	6.9	7.0	7.0	3.8	5.0	1.6	2.3

4.3.6. X-ray diffraction (XRD) analyses

In order to investigate the microstructural orders and molecular arrangements of nanocomposites **P1-P4/ZnOpy** (with or without H-bonded interactions) in solids, X-ray diffraction (XRD) measurements were also performed on powder samples of metallo-polymers **P1-P4** and nanoparticle **ZnOpy**, and all powder XRD spectra are illustrated in Figure 4.10. The annealed **P3/ZnOpy** (Figure 4.10(c)) and **P4/ZnOpy** (Figure 4.10(d)) films exhibited substantially a primary diffraction feature at $2\theta = 5.0°$ (corresponding to a smaller *d*-spacing value of 12.0 Å).[110] Compared with the amorphous halos of metallo-polymers **P3-P4**, the much stronger (100) reflection characteristic peaks of metallo-polymers **P3-P4** in nanocomposites **P3-P4/ZnOpy** (with H-bonds) were observed. However, only weaker or no (100) reflection characteristic peaks of metallo-polymers **P1-P2** in nanocomposites **P1-P2/ZnOpy** (without H-bonds) were detected. The characteristic peaks were assigned to a distance between the conjugated backbones separated by the long side chains as reported for other similar π-conjugated polymers with long pendants.[111-112] The XRD data demonstrate the existence of the H-bonded interactions between metallo-polymers

P3-**P4** and nanoparticle **ZnOpy**. In other words, the crystallinities of metallo-polymers **P3**-**P4** were enhanced upon addition of nanoparticle **ZnOpy**. The similar result was also reported that the crystallinity of P3HT polymer was increased upon addition of BT4T (a small organic molecule), which, in turn, enhanced the photovoltaic properties of the solar cell device.[113] For metallo-polymers **P1**-**P4**, the broad peaks in the wide angle region of the diffraction features at 2θ = 13.7°, corresponding to the *d*-spacing values between 4.1 and 4.4 Å, and it is reasonable to assign them to the distance between disordered alkyl chains, although the peaks may also contain contributions from the layer-to-layer π-π stacking of the polymer planes.[114] The broad XRD halos indicated that the layer-to-layer π-π stacking in the polymers occurs only in very small areas, and the polymers mainly show amorphous structure.[115-117] The possible packing motifs (side-view) and the proposed model can explain the possible structural arrangements of the polymer chains in nanocomposites **P3**-**P4**/**ZnOpy**, where the alkyl side chains stack as bi-layered packings and may have trivial interdigitated arrangements, and their schematic packings are demonstrated in Figure 4.11. Overall, based on the observation, it reveals that metallo-polymers **P3**-**P4** form higher crystallinity upon addition of **ZnOpy** in nanocomposites **P3**-**P4**/**ZnOpy** (with H-bonds) in contrast to amorphous **P3**-**P4**.

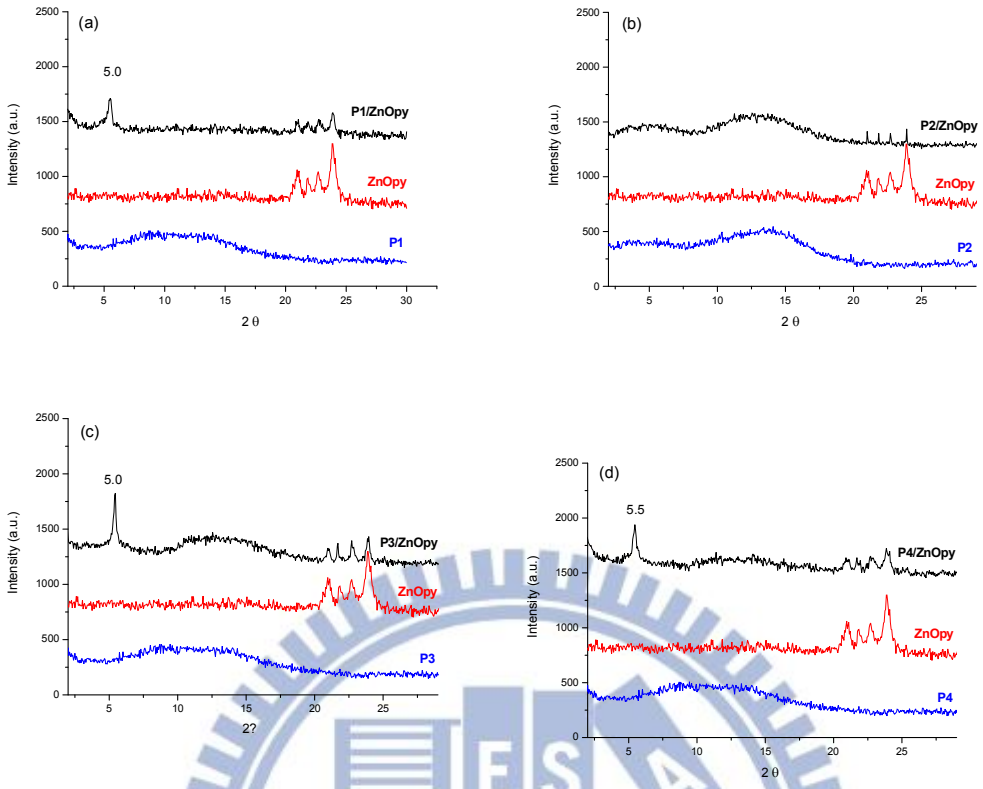

Figure 4.10 Powder X-ray diffraction spectra of nanocomposites (a) **P1/ZnOpy**, (b) **P2/ZnOpy**, (c) **P3/ZnOpy**, and (d) **P4/ZnOpy**.

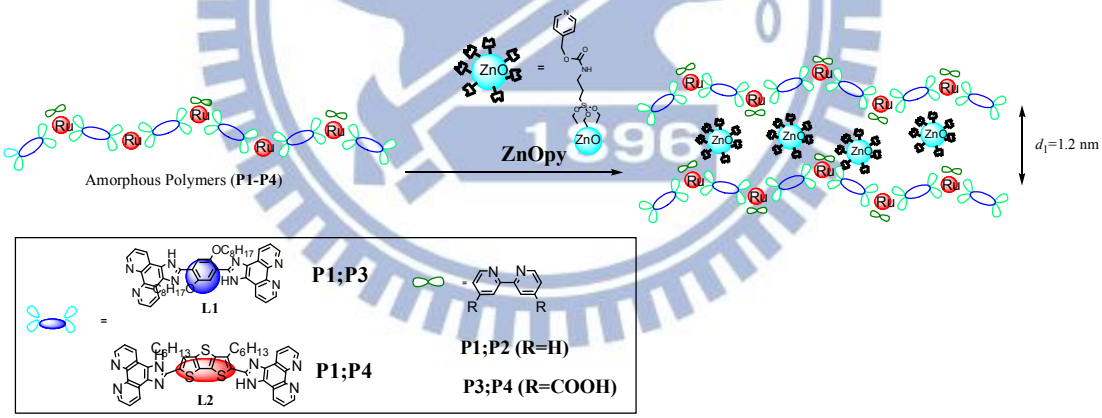

Figure 4.11 Schematic illustrations of possible structural arrangements for polymer chains in nanocomposites by powder X-ray diffractions.

4.3.7. Transmission electron microscopy studies

Transmission electron microscopy (TEM) analyses were carried out on nanocomposites **P1-P4/ZnOpy** (with or without H-bonded interactions) in solids,

which were prepared from DMF solutions of **P1**-**P4**/**ZnOpy** drop-cast onto TEM grids. This provides a further insight into the morphology of the nanoparticle aggregation. Compared with nanocomposite **P3**/**ZnOpy** (with H-bonds) in Figure 4.12(c), nanocomposite **P1**/**ZnOpy** (without H-bonds) had a more distinct aggregated structure in Figure 4.12(a). This was due to the pyridyl H-acceptors of **ZnO** self-assembled with H-donors of metallo-polymer **P3**. This result is similar to a previous report in CdSe-L2,[118] where a conjugated polymer was functionalized via the introduction of appropriate anchoring groups to avoid the phase separation.[119] On the other hand, as **ZnOpy** nanoparticles were blended with metallo-polymer **P4**, the carboxylic acid surfactants from metallo-polymer **P4** were H-bonded with the pyridyl H-acceptor groups of **ZnOpy**. Therefore, in contrast to **P2**/**ZnOpy** (without H-bonds) in Figure 4.12(b) **ZnOpy** nanoparticles were well distributed among metallo-polymer **P4** in Figure 4.12(d). Hence, the TEM morphologies of H-bonded architectures in nanocomposites **P3**-**P4**/**ZnOpy** (with H-bonds) demonstrate the versatility of the self-assembled processes by the supramolecular interactions of H-donor metallo-polymers **P3**-**P4** and H-acceptor nanoparticle **ZnOpy**.

(a) (b)

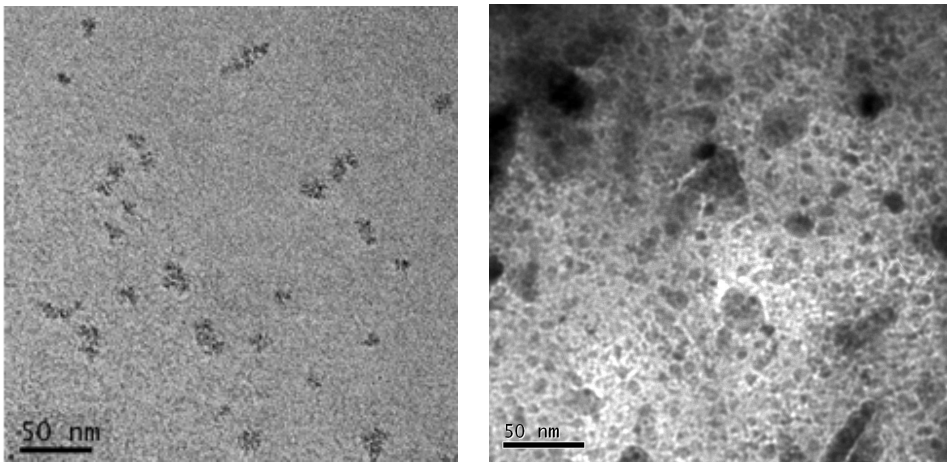

(c) (d)

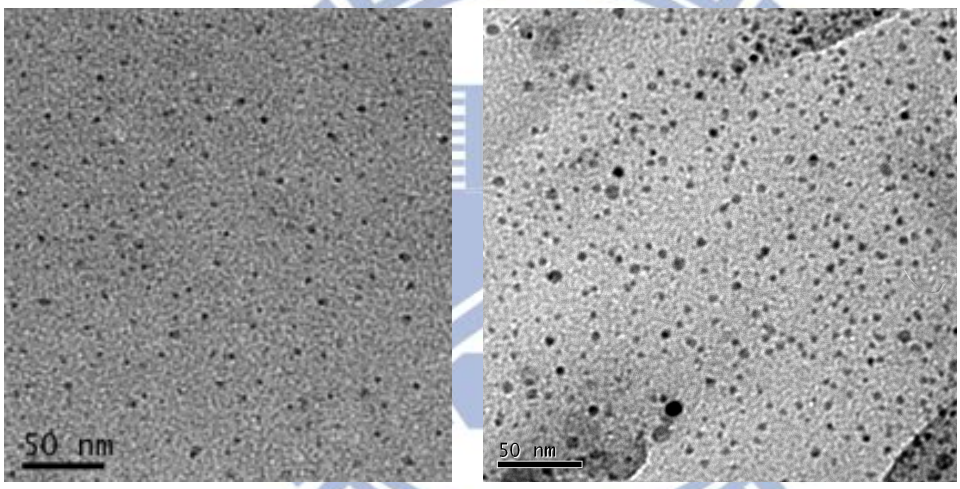

Figure 4.12 TEM images of nanocomposites (a) **P1/ZnOpy**, (b) **P2/ZnOpy**, (c) **P3/ZnOpy**, and (d) **P4/ZnOpy**.

4.4 Conclusions

We synthesized a series of metallo-polymers (**P1-P4**) with aryl-imidazo-phenanthrolines (AIP) units (incorporated with phenyl and fused dithienothiophene groups in different donor spacers) to study for their electrochemical and electrochromic properties. In order to investigate the energy transfers between

metallo-polymers (**P1-P4**) and nanoparticle **ZnOpy**, novel supramolecular nanocomposites **P3-P4/ZnOpy** were constructed by complexation of proton donor (H-donor) metallo-polymers **P3-P4**, consisting of carboxylic acid groups, with proton accepter (H-accepter) **ZnOpy**. They were compared with nanocomposites **P1-P2/ZnOpy** containing metallo-polymers **P1-P2** without carboxylic acid groups to have no H-bonded interactions with nanoparticle **ZnOpy**. In contrast to amorphous metallo-polymers **P3-P4** from XRD measurements, supramolecular nanocomposites **P3-P4/ZnOpy** exhibited obvious diffraction features (originated from metallo-polymers **P3-P4**) indicating the increased crystallinities of **P3-P4** upon addition of **ZnOpy**, due to the supramolecular (H-bonded) interactions. TEM morphologies also proved that the supramolecular (H-bonded) interactions between **ZnOpy** and polymers **P3-P4** induce nanoparticles to be homogeneously dispersed in nanocomposites **P3-P4/ZnOpy**.

Chapter 5

Synthesis of Metal-Free Organic Dyes Containing Tris(dodecyloxy)phenyl and Dithienothiophenyl Units and a Study of Their Mesomorphic and Photovoltaic Properties

In this study we synthesized three metal-free organic dyes (**Cpd11**, **Cpd16**, and **Cpd22**) featuring 3,4,5-tris(dodecyloxy)phenyl and cyanoacrylic acid moieties as electron-donor and electron-acceptor/anchoring units, respectively, linked through various dithienothiophenyl conjugated spacers. **Cpd16** exhibits mesomorphic properties, confirmed through polarizing optical microscopy, differential scanning calorimetry, and X-ray diffraction (XRD), due to the appropriate ratio of the lengths of its flexible chain to its rigid core. Molecular modeling of **Cpd16**, and its *d*-spacing determined from XRD data, verified the existence of a tilt angle in the SmC phase. Among these metal-free organic dyes, a dye-sensitized solar cell incorporating **Cpd16** exhibited the best performance, presumably because of its better packing and its mesomorphic properties; the power conversion efficiency was 3.72% (V_{oc} = 0.58 V; J_{sc} = 9.98 mA cm^{-2}; FF = 0.65) under simulated AM 1.5 irradiation (100 mW cm^{-2}).

5.1 Introduction

The development of novel materials for use in organic optoelectronic devices, such as dye-sensitized solar cells (DSSCs),[15] has become a popular research topic in the quest for low-cost, green materials for sustainable use and a decrease in demand for fossil fuels and nuclear power. DSSCs based on Ru-photosensitizers,[16-17] such as cis-bis(isothiocyanato)bis(2,2′-bipyridyl-4,4′-dicarboxylato)-ruthenium(II) (**N3**)[18] and related derivatives, have been applied very successfully with high power conversion efficiencies (PCEs) of 9–12%.[19-23] Recently, it has been demonstrated that DSSCs can also be constructed from metal-free organic dyes.[14] Because of the high cost of rare Ru metal and the relatively low molar extinction coefficients and tedious purification of Ru-photosensitizes,[20] metal-free organic sensitizers have become increasingly attractive and widely developed.[24,25] Nevertheless, the ability to reach higher efficiencies when using metal-free organic dyes remains a challenge, although great progress has been made in this field.[26-29] The key characteristics for a dye to be used in a DSSC are high absorption over a wide range of the solar spectrum with high molar extinction coefficients, efficient charge separation, redox stability, andsuitable functional groups to interact with the electron sink (TiO_2). Metal-free organic dyes featuring a donor/acceptor structural design were synthesized have particularly wide absorption ranges for DSSC applications.[24-32] Liquid-crystalline (or mesomorphic)

properties can be introduced to organic dyes when 3,4,5-tris(dodecyloxy)phenyl segments are incorporated, resulting in potential applications in flexible electronic materials.[33-34,120-123] Kato et al.[34] reported conjugated oligothiophene-based polycatenar liquid crystal materials exhibiting electrochromism upon applying an oxidative potential, with layered smectic and columnar structures capable of enhancing hole mobilities up to 0.01 cm^2 V^{-1} s^{-1} Park et al.[120] also reported that the mesomorphic organization of a dicyanodistyrylbenzene-based molecule could improve its fluorescence-emitting and semiconducting properties. Therefore, great efforts have been taken toward the preparation and characterization of photo- and electro-active structures based on mesogenic units. The use of various aromatic segments (e.g., fluorene,[124-125] thiophene[126-127]) as spacers in organic dyes can improve the photocurrent generation and intramolecular charge separation. Dithieno[3,2-*b*:2′,3′-*d*]thiophene (DTT)–conjugated dyes have also exhibited excellent DSSC efficiencies.[128] In addition, the DTT unit–a sulfur-rich (three S atoms) and electron-rich building block–increases the planarity of the dye, resulting in longer π-conjugation.[129-130] Because of restricted intramolecular rotation in fused-ring structures such as DTT, π-orbital overlap in such conjugate molecules could be maximized to enhance intermolecular charge transport.[131-132] In this study, we prepared dyes featuring a 3,4,5-tris(dodecyloxy)phenyl unit[34] and a cyanoacrylic acid

as electron donor and acceptor units, respectively, with various spacers inserted as the conjugated bridge (Figure 5.1). For example, we introduced a fused-DTT unit as a conjugated spacer through which electrons could be transferred efficiently from the donor to the acceptor. In addition to the DTT unit (as a main structure of the conjugated spacer), we also employed bithiophene and bithiazole units to extend the conjugated lengths and, thereby, affect the electron mobilities and absorption spectra. Furthermore, bithiophene unit enhanced the liquid crystallinity of the dye. To increase solubility, we inserted alkyl chains onto bithiazole heterocyclic rings. We were aware, however, that the presence of thiophene rings in the electron-rich segment might not result in sufficient separation between the highest occupied molecular orbital (HOMO) and lowest unoccupied molecular orbital (LUMO); in addition, too many alkyl chains would affect the packing between the layers the molecule, induce molecular aggregation, increase steric hindrance, and decrease charge transfer. If the structure had too many rigid rings, however, its solubility would be impacted, making it harder to dissolve in common solvents with low boiling points and, thereby, complicating device fabrication. Therefore, we also compared the effects of bithiophene[133-137] and bithiazole[136] units. The design of the conjugated system can not only affect the absorption range but also further influence the electron transfer from the excited state to the TiO_2. In this study, we suspected that better molecular arrangements and

stacking would result if the donor/acceptor molecules exhibited enhanced liquid crystallinity Therefore, we prepared series of metal-free organic dyes containing DTT[137] units with good coplanarity and investigated their mesomorphic and photovoltaic properties.

5.2 Experimental

5.2.1 Materials

Chemicals and solvents were reagent grades and purchased from Aldrich, ACROS, TCI, and Lancaster Chemical Co. Toluene, tetrahydrofuran (THF), Dimethylformamide (DMF) and dichloromethane (DCM) were distilled to keep anhydrous before use. N-Bromosuccinimide was recrystallized from distilled water and dried under vacuum. The other chemicals were used without further purification. The synthetic routes and detailed procedures of all dyes are shown in Scheme 5.1. 5-bromo-1,2,3-tris-n-dodecyloxybenzene[28] (**1**), tri-n-butyl-(dithieno[3,2-*b*:2′,3′-*d*]thiophen-2-yl)-stannane[125] (**2**), 5-(5-bromothiophen-2-yl)thiophene-2-carbaldehyde[125] (**6**), 2-(5-bromo-4-hexylthiazol-2-yl)-4-hexylthiazole-5-carbaldehyde[124,141] (**7**) were synthesized by literature.

5.2.2. Synthesis

5.2.2.1. 2-(3,4,5-Tris-n-dodecyloxyphenyl)-dithithieno[3,2-*b*:2′,3′-*d*]thiophene (**3**)

To a 100 ml, three-neck, round-bottom flask were added 5-bromo-1,2,3-tris-n-dodecyloxybenzene (**1**) (1 mmol, 2.34 g), tri-n-butyl-(dithieno[3,2-*b*:2′,3′-*d*]thiophen-2-yl)-stannane (**2**), (3.29 mmol, 1.6 g), and dry toluene (50ml). The mixture was deoxygenated with nitrogen for 30 min. $Pd(PPh_3)_4$ (0.02 mmol, 110mg) was added, and the mixture was heated to 110 ℃ for 2 days. The organic layer was extracted with DCM, and the extracts were dried over anhydrous magenesium sulfate ($MgSO_4$). Column chromatography on silica gel hexanes/CH_2Cl_2 (3:1). Yield: 55.6%. ^{1}H NMR（$CDCl_3$, 300 MHz）: δ 7.41 (s, 1H), 7.35 (d, *J*= 5.2 Hz, 1H), 7.28 (d, *J*= 5.2 Hz, 1H), 6.81 (s, 2H), 4.06-3.96 (m, 6H), 1.88-1.73 (m, 6H), 1.56-1.47 (m, 6H), 1.26 (br., 48H), 0.94 (m , 9H). ^{13}C NMR (100 MHz, $CDCl_3$): δ 161.2, 153.5, 145.3, 141.9, 140.8, 138.4, 129.7, 125.7, 120.7, 116.2, 104.6, 73.5, 69.2, 31.9, 30.3, 29.7, 29.6, 29.3, 29.1, 26.0, 22.7, 14.1. MS (FAB): *m/z* 824 (M^+). Anal. Calcd. for $C_{50}H_{80}O_3S_3$: C, 72.76; H, 9.77. Found : C, 72.54; H, 9.82.

5.2.2. 6-[1,2,3-tris(dodecyloxy)phenyl]dithieno[3,2-*b*:2′,3′-*a*]thiophene-2-carb-

aldehyde (**4**) Compound **4** was synthesized by Vilsmeier formylation from Compound **3**. A 250-mL three-necked flask containing 0.1 mL (1 mmol) of anhydrous DMF was cooled in an ice bath. To the solution, 0.1ml (1.5 mmol) of phosphorus chloride ($POCl_3$) was added dropwisely for 30 min. 2-(3,4,5-Tris-n-dodecyloxyphenyl)-dithithieno[3,2-*b*:2′,3′-*d*]thiophene (**3**) (0.82 g) in

30 ml of 1,2-dichloroethane was added to the above solution and heated to 90 °C for 1 days. This solution was cooled to room temperature, poured into ice water, and neutralized to pH 6-7 by dropwise addition of saturated aqueous sodium hydroxide solution. The mixture was extracted with Ch_2Cl_2/water. The organic layer was dried with anhydrous $MgSO_4$ and then concentrated under reduced pressure. The crude product was purified by column chromatography with CH_2Cl_2/hexane (1:1) to get 0.7 g of yellow solids. Yield: 82%. ^{1}H NMR（$CDCl_3$, 300 MHz）: δ 9.95 (s, 1H), 7.95 (s, 1H), 7.45 (s, 1H), 6.82 (s, 2H), 4.05-3.97 (m, 6H), 1.86-1.73 (m, 6H), 1.49-1.42 (m, 6H), 1.26 (br, 48H), 0.87 (m, 9H). ^{13}C NMR (100 MHz, $CDCl_3$): δ 147.8, 143.5, 138.3, 136.7, 136.2, 135.6, 126.6, 125.3, 122.8, 121.9, 103.6, 69.2, 31.9, 29.7, 29.4, 26.0, 22.8, 14.1. MS (FAB): *m/z* 852.5 (M^+). Anal. Calcd. for $C_{51}H_{80}O_4S_3$: C, 71.76; H, 9.47. Found : C, 71.54; H, 9.42.

5.2.2.3. 6-[1,2,3-tris(dodecyloxy)phenyl] -2-tributylstannyl dithieno[3,2-*b*:2′,3′-*a*]thio -phene (**5**). 2-(3,4,5-Tris-n-dodecyloxyphenyl)-dithithieno[3,2-*b*:2′,3′-*d*]thiophene (**3**) (0.83 g, 0.1 mmol) in a 250 ml flask was placed in dry THF (20 ml), to which n-BuLi (0.59 mL, 2.5 M in hexane, 1.5 mmol) was added at -78 °C under stirring for 1 hr. Thereafter, the mixture was warmed up slowly to room temperature in an ambient environment with stirring for 1 hr. After the mixture was cooled down to -78 °C again, an amount of Bu_3SnCl (0.53 mL, 1.2 mmol) was added slowly. The mixture

was then stirred at ambient temperature for 18 hrs, followed by the addition of water (100ml). Finally, the aqueous layer was extracted with dichloromethane (200ml) while the combined organic layer was dried with anhydrous $MgSO_4$ and concentrated under a reduced pressure to give a crude product. The crude product was purified by column chromatography with CH_2Cl_2/hexane (2:5) to get a pale yellow oil. ^{1}H NMR （$CDCl_3$, 300 MHz）: δ 7.00 (s, 2H), 6.44 (s, 2H), 3.94 (m, 6H), 1.71 (m, 6H), 1.33 (br, 24H), 1.29 (br, 48H), 0.96 (m, 18H). ^{13}C NMR (100 MHz, $CDCl_3$): δ 147.8, 138.3, 136.2, 127, 126.6, 126.0, 125.3, 122.8, 121.9, 121.1, 103.6, 69.2, 31.9, 29.4, 28.8, 27.3, 22.8, 14.1, 13.8. MS (FAB): *m/z* 1114.4 (M^+). Anal. Calcd. for $C_{62}H_{106}O_3S_3Sn$: C, 66.82; H, 9.59. Found : C, 66.84; H, 9.52.

5.2.2.4. 5-(5-6-[1,2,3-tris(dodecyloxy)phenyl] dithieno[3,2-*b*:2′,3′-*a*]thiophylthiophen -2-yl)thiophene-2-carbaldehyde (**8**). A 250 ml two-necked flask containing 6-[1,2,3-tris(dodecyloxy)phenyl] -2-tributylstannyl dithieno[3,2-*b*:2′,3′-*a*]thio -phene (**5**)(1.1 mmol, 0.85 g), 5-(5-bromothiophen-2-yl)thiophene-2-carbaldehyde (**6**) (0.77 mmol, 0.21 g), and $Pd(PPh_3)_4$ (0.03 mmol, 0.026g), in 15 ml of tolulene was added to the above solution and heated to 90 °C for 1 day. The mixture was extracted with CH_2Cl_2/water. The organic layer was dried with anhydrous $MgSO_4$ and concentrated under a reduced pressure. The crude product was purified by column chromatography with CH_2Cl_2/hexane (1:1) to get 0.5g, of red-orange solids. Yield:

64.5 %. ^{1}H NMR（$CDCl_3$, 300 MHz）: δ 9.86 (s, 1H), 7.68 (d, 1H), 7.41 (s, 2H), 7.30 (d, 1H), 7.25 (d, 1H), 7.17 (d, 1H), 6.81 (s, 2H), 4.05-3.96 (m, 6H), 1. 86-1.73 (m, 6H), 1.49-1.42 (m, 6H), 1.26 (br, 48H), 0.87 (m , 9H). ^{13}C NMR (100 MHz, $CDCl_3$): δ 182.5, 147.8, 143.5, 138.3, 136.2, 129.4, 126.6, 125.3, 122.8, 121.9, 103.6, 69.2, 31.9, 29.7, 29.4, 26.0, 22.8, 14.1. MS (FAB): *m/z* 1017.5 (M^+). Anal. Calcd. for $C_{59}H_{84}O_4S_3$: C, 69.64; H, 8.32. Found : C, 69.54; H,8.42.

5.2.2.5. 5-(5-6-[1,2,3-tris(dodecyloxy)phenyl] dithieno[3,2-*b*:2′,3′-*a*]thiophyl-2-(4-hexylthiazol-2-yl)-4-hexylthiazole -2-carbaldehyde (**9**)

A 250 ml two-necked flask containing 6-[1,2,3-tris(dodecyloxy)phenyl] -2-tributylstannyl dithieno[3,2-*b*: 2′,3′-*a*]thiophene (**5**) (1.1 mmol, 0.85 g), 2-(5-bromo-4-hexylthiazol-2-yl)-4-hexylthiazole-5-carbaldehyde (**7**) (0.77 mmol, 0.21g), and $Pd(PPh_3)_4$ (0.03 mmol, 0.026g), in 15 ml of tolulene was added to the above solution and heated to 90 °C for 1 day. The mixture was extracted with CH_2Cl_2/water. The organic layer was dried with anhydrous $MgSO_4$ and concentrated under a reduced pressure. The crude product was purified by column chromatography with EA/hexane (1:10) to get 0.5g, of red-orange solids. Yield: 64.5 %. ^{1}H NMR（$CDCl_3$, 300 MHz）: δ 10.1 (s, 1H), 7.43 (s, 1H), 7.39(s, 1H), 6.82(s, 2H), 4.01(t, 6H), 3.05 (t, 4H), 1.83 (m, 10H), 1.47-1.26 (m, 66H), 0.88 (m, 15H)。^{13}C NMR (100 MHz, $CDCl_3$): δ 160.0, 153.0, 147.8, 138.3, 137.0, 136.2, 126.6, 125.3, 122.8, 121.9,

114.0, 69.5, 69.2, 31.9, 31.3, 31.0, 29.7, 29.4, 29.0, 26.4, 26.0, 22.8, 14.1. MS (FAB): *m/z* 1186.9 (M^+). Anal. Calcd. for $C_{69}H_{106}N_2O_4S_3$: C, 69.79; H, 8.99. Found : C, 69.54; H,9.02.

5.2.2.6. 3-{6-[1,2,3-tris(dodecyloxy)phenyl]dithieno[3,2-*b*:2′,3′-*a*]thiophene-2-yl}-2-cyanoacrylic acid (**Cpd11**)

6-[1,2,3-tris(dodecyloxy)phenyl]dithieno[3,2-*b*:2′,3′-*a*]thiophene-2'- carbaldehyde (**4**) (0.70 g)、cyanoacetic acid (0.12 g), ammonium acetate (0.063 g), and glacial acetic acid (60 mL) were mixed together and heated at 110 °C with efficient stirring for overnight. The red solution was cooled to induce precipitation. The precipitate formed was filtered and thoroughly washed with water and methanol. A red solid was obtained. Yield: 79.8%. ^{1}H NMR（d-THF, 300 MHz）: δ 8.41 (s, 1H), 8.14 (s, 1H), 7.68(s, 1H), 6.93(s, 2H), 4.07-3.94 (m, 6H), 1.87-1.72 (m, 6H), 1.54-1.51(m, 6H), 1.30 (br, 48H), 0.88 (m, 9H). MS (FAB): *m/z* 920 (M^+). Anal. Calcd. for $C_{54}H_{81}NO_5S_3$: C, 70.47; H, 8.87 ; N, 1.52. Found : C, 70.36; H, 8.74 ; N, 1.15.

5.2.2.7. 3-{5-(5-6-[1,2,3-tris(dodecyloxy)phenyl] dithieno[3,2-*b*:2′,3′-*a*]thiophylthio -phen -2-yl)thiophyl}-2-cyanoacrylic acid (**Cpd16**). The **Cpd16** dye was synthesized by the same procedue as **Cpd11**, afforded dark brown solid. Yield: 73.2 %. ^{1}H NMR（d-THF, 300 MHz）: δ 8.34 (s, 1H), 7.80 (d, 1H), 7.66 (s, 1H), 7.63 (s, 1H), 7.49 (d, 1H), 7.41 (d, 1H) 7.33 (d, 1H), 6.91 (s, 2H), 4.07-3.93 (m, 6H), 1.86-1.73 (m, 6H),

1.49-1.42(m, 6H), 1.26 (br, 48H), 0.87 (m, 9H). MS (FAB): m/z 1084 (M^+). Anal. Calcd. for $C_{62}H_{85}NO_5S_5$: C, 68.65; H, 7.90 ; N, 1.29. Found : C, 68.47; H, 8.23 ; N, 1.05.

5.2.2.8. 3-{5-(5-6-[1,2,3-tris(dodecyloxy)phenyl] dithieno[3,2-*b*:2′,3′-*a*]thiophyl }-2-(4- hexylthiazol-2-yl)-4-hexylthiazole -2-cyanoacrylic acid (**Cpd22**). The cpd16 dye was synthesized by the same procedue as **Cpd11**, afforded dark brown solid. Yield: 73.2 %. ^{1}H NMR（$CDCl_3$, 300 MHz）: δ 8.35 (s, 1H), 7.43 (s, 1H), 7.39 (s, 1H), 6.82 (s, 2H), 4.01 (t, 6H), 3.05 (t, 4H), 1.83 (m, 10H), 1.47-1.26 (m, 66H), 0.88 (m, 15H). MS (FAB): m/z 1254 (M^+). Anal. Calcd. for $C_{72}H_{107}N_3O_5S_5$: C, 68.91; H, 8.59 ; N, 3.35. Found : C, 69.12; H, 8.41 ; N, 3.53.

5.3 Measurement and Characterizations

^{1}H NMR spectra were recorded on a Varian unity 300 MHz spectrometer using d_6-DMSO and *d*-$CHCl_3$ as solvents. Elemental analyses were performed on a HERAEUS CHN-OS RAPID elemental analyzer. UV-visible absorption spectra were recorded in dilute THF solutions (10^{-5} M) on a HP G1103A spectrophotometer, and photoluminescence (PL) spectra were obtained on a Hitachi F-4500 spectrophotometer. Cyclic voltammetry (CV) measurements were performed using a BAS 100 electrochemical analyzer with a standard three-electrode electrochemical cell in a 0.1 M tetrabutylammonium hexafluorophosphate ($TBAPF_6$) solution (in THF)

at room temperature with a scanning rate of 100 mV/s. During the CV measurements, the solutions were purged with nitrogen for 30s. In each case, a carbon coating rod as the working electrode, a platinum wire as the counter electrode, and a silver wire as the quasi-reference electrode were used, and Ag/AgCl (3 M KCl) electrode was served as the reference electrode for all potentials quoted herein. The redox couple of ferrocene/ferrocenium ion (Fc/Fc^{+}) was used as an external standard. The corresponding HOMO and LUMO levels were calculated from the onset oxidation potential ($E_{ox/onset}$) and UV-vis absorption edge (Eg^{opt}), respectively. Mesophasic textures were characterized by polarizing optical microscopy (POM) using a Leica DMLP equipped with a hot stage.

5.3.1. X-ray Diffraction Characterization. Synchrotron powder X-ray diffraction (XRD) measurements were performed at beamline BL17A of the National Synchrotron Radiation Research Center (NSRRC), Taiwan, where the wavelength of X-ray was 1.33366 Å. The powder samples were packed into a capillary tube and heated by a heat gun, whose temperature controller is programmable by a PC with a PID feedback system. The scattering angle theta was calibrated by a mixture of silver behenate and silicon.

5.3.2. TiO_2 Paste Preparation. The preparation of TiO_2 precursor and the electrode fabrication were carried out based on previous report[34] with an autoclaved

temperature of 240°C. The precursor solution was made according to the following procedure: 430 mL of 0.1 M nitric acid solution under vigorous stirring was slowly combined with 72 mL $Ti(C_3H_7O)_4$ to form a mixture. After the hydrolysis, the mixture was heated at 85°C in a water bath and stirred vigorously for 8 h in order to achieve the peptization. When the mixture was cooled down to room temperature, the resultant colloid was filtered, and the filtrate was then heated in an autoclave at a temperature of 240°C for 12 h to grow the TiO_2 particles. When the colloid was cooled to room temperature, it was ultrasonically vibrated for 10 min. The TiO_2 colloid was concentrated to 13 wt%, followed by the addition of 30 wt% (with respect to TiO_2 weight) of poly (ethylene glycol) (PEG, MW = 20000 g/mol) to prevent the film from cracking while drying.

5.3.3. Device Fabrication. The TiO_2 paste was then deposited on a FTO glass substrate by the glass rod method with a dimension of 0.5×0.5 cm^2. The polyester tape (3M) was used as an adhesive on two edges of a FTO glass. The tape was removed after the TiO_2 paste was spread on the FTO by a glass rod and the TiO_2 paste was dried in the air at room temperature for 1 h. The TiO_2-coated FTO was heated to 500°C at a heating rate of 10°C /min and maintained for 30 min before cooled to room temperature. After repeating the same procedure described above to control the thickness of a TiO_2 film, the final coating was carried out with TiO_2 pastes containing

different sizes (300 nm and 20 nm with weight percentages of 30 and 70, respectively) of light scattering TiO_2 particles and then heated to 500°C. The thicknesses of TiO_2 films were measured by a profilometer (Dektak3, Veeco/Sloan Instruments, Inc.). The adsorbed density of each dye was calculated from the concentration difference of each solution before and after TiO_2 film immersion. The TiO_2 electrode with a geometric area of 0.25 cm^2 was immersed in a acetonitrile/tert-butanol mixture (volume ratio 1:1) containing 3×10^{-4} M cis-di(thiocyanato)bis(2,2'-bipyridyl- 4,4'-dicarboxylato) ruthenium(II) bis(tetrabutylammonium) (N719, Solaronix SA) or in the THF solutions containing 3×10^{-4} M organic sensitizers for overnight. A thermally platinized FTO was used as a counter electrode and was controlled to have an active area of 0.36 cm^2 by adhered polyester tape with a thickness of 60 μm. After rinsing with CH_3CN or THF, the photoanode was placed on top of the counter electrode and tightly clipping them together to form a cell. Electrolyte was then injected into the space and then sealing the cell with the Torr Seal cement (Varian, Inc.). The electrolyte was composed of 0.5 M lithium iodide (LiI), 0.05 M iodine (I_2), and 0.5 M 4-tert-butylpyridine (TBP) dissolved in acetonitrile. The photovoltage transients of assembled devices were recorded with a digital oscilloscope (LeCroy, WaveSurfer 24Xs). Pulsed laser excitation was applied by a Q-switched Nd:YAG laser (Continuum, model Minilite II) with 1 Hz repetition rate at 532 nm and a 5 ns pulse

width at half-height. The beam size was slightly larger than 0.5 × 0.5 cm^2 to cover the area of the device. The photovoltage of each device was adjusted by incident pulse energy to be 40 mV.

5.3.4. Device measurements. A 0.6×0.6 cm^2 cardboard mask was clipped onto the device to constrain the illumination area. The photoelectrochemical characterizations on the solar cells were carried out by using an Oriel Class A solar simulator (Oriel 91195A, Newport Corp.). Photocurrent-voltage characteristics of the DSSCs were recorded with a potentiostat/galvanostat (CHI650B, CH Instruments, Inc.) at a light intensity of 1.0 sun calibrated by an Oriel reference solar cell (Oriel 91150, Newport Corp.). The monochromatic quantum efficiency was recorded through a monochromator (Oriel 74100, Newport Corp.) at short circuit condition. The intensity of each wavelength was in the range of 1 to 3 mW/cm^2.

5.3 Results and Discussion

5.3.1. Optical properties

Figure 5.2 displays the UV–Vis absorption and normalized photoluminescence (PL) spectra of **Cpd11**, **Cpd16**, and **Cpd22** as solutions in THF (10^{-5} M); Table 5.1 lists their corresponding data. The absorption spectra reveal that the signals for **Cpd16** and **Cpd22** were red-shifted relative to those of **Cpd11** after the insertion of the bithiophene and bithiazole units, respectively, to lengthen the conjugated linking structures. The maximum absorption peaks for **Cpd11**, **Cpd16**, and **Cpd22** at 443, 476, and 473 nm, respectively, resulted from intramolecular charge transfer (ICT); that is, for the transition from the 3,4,5- tris(dodecyloxy)benzene donor to the cyanoacrylic acid acceptor. The spectra of the dyes **Cpd16** and **Cpd22** both featured weak π–π* transition bands, at 386 and 374 nm, respectively, whereas that of **Cpd11** featured only a single intense band at 443 nm (see Table 5.1). As expected, the elongated π-conjugations in **Cpd16** and **Cpd22** resulted in narrower π–π* energy gaps and spectral red shifts for the π–π* transitions. Because the inserted bithiophene and bithiazole units extended the conjugation lengths in **Cpd16** and **Cpd22**, both dyes exhibited red-shifted and broader absorptions than those of **Cpd11**.[138] Since **Cpd11** had the narrowest absorption wavelength (Figure 5.2a), it also displayed the worst photovoltaic performance among the tested dyes. The molar extinction coefficients of

Cpd16 (476 nm; ε = 7.50 × 10^4 M^{-1} cm^{-1}) and **Cpd22** (473 nm; ε = 7.70 × 10^4 M^{-1} cm^{-1}) at their maximum absorptions are lower than that of **Cpd11** (443 nm; ε = 9.90 × 10^4 M^{-1} cm^{-1}), because the inserted bithiophene and bithiazole units decreased the coplanarity of the acceptor and donor moieties and, therefore, decreased the degree of charge transfer.[139-140] Furthermore, in comparison with conventional ruthenium complexes (e.g., **N3**; ε = 1.52 × 10^4 M^{-1} cm^{-1}),[18] the molar extinction coefficients of the dyes are relatively large, indicating that they have good light harvesting ability. The bathochromic shifts upon proceeding from **Cpd11** to **Cpd16** (33 nm) and from **Cpd11** to **Cpd22** (30 nm) presumably resulted from the extended π-conjugations. Figure 5.2b reveals that when THF solutions of **Cpd11**, **Cpd16**, and **Cpd22** were excited at 443, 475, and 475 nm, respectively, the resulting PL spectra featured weak emissions with Stokes shifts in the range 114–148 nm, with the PL emissions of dyes following similar trends to those in their absorption spectra.

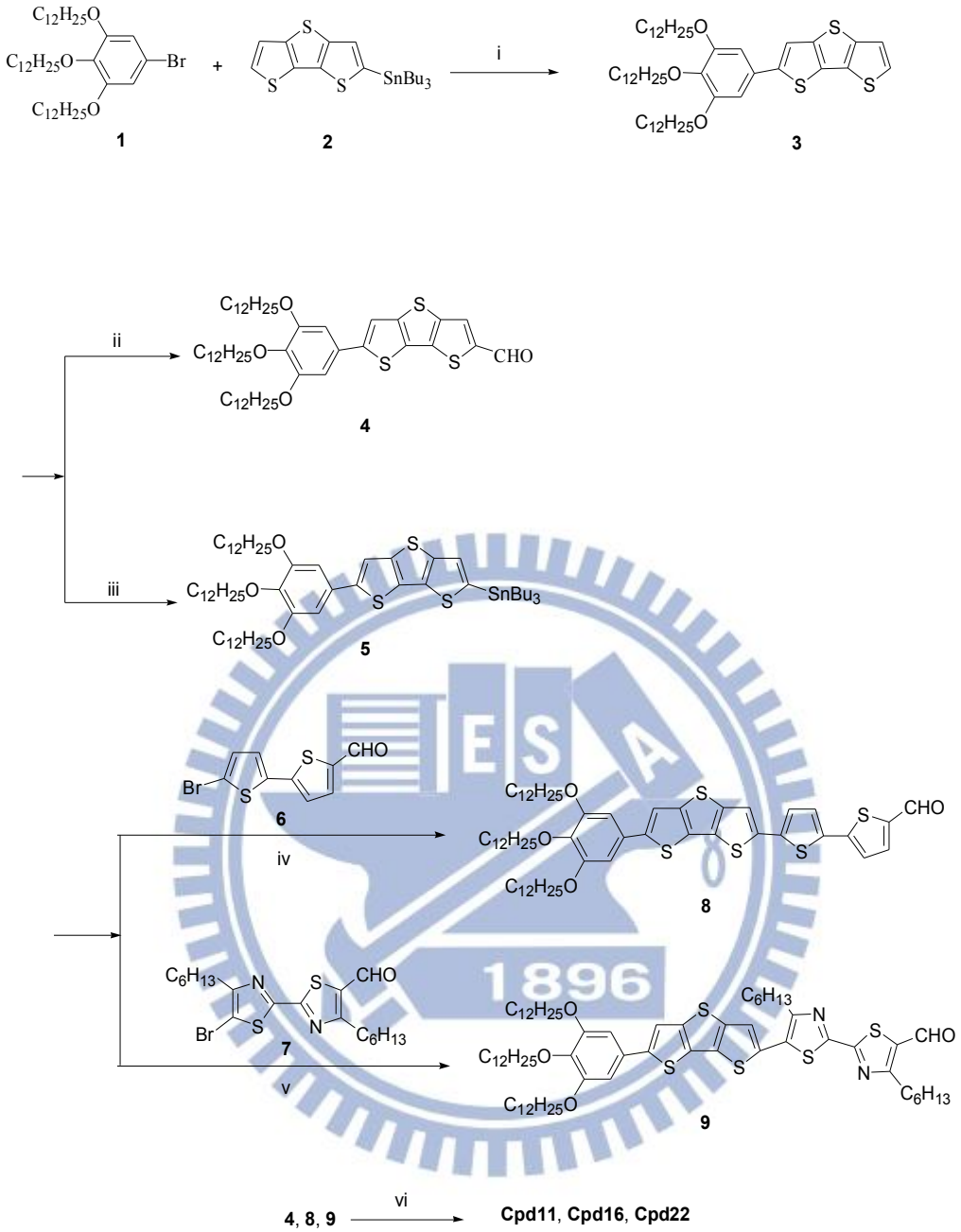

Scheme 5.1 Synthetic Route of Dyes. (i) (iv) (v) $Pd(PPh_3)_4$, toluene, reflux. (ii) $POCl_3$, DMF, DCE. (iii) n-BuLi, THF, -78°C, $SnBu_3Cl$. (vi) $CNCH_2COOH$, NH_4OAc,CH_3COOH.

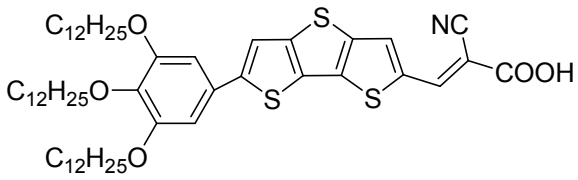

Cpd11

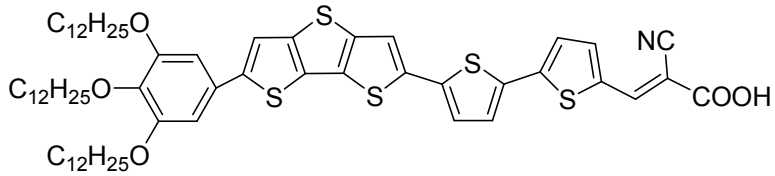

Cpd16

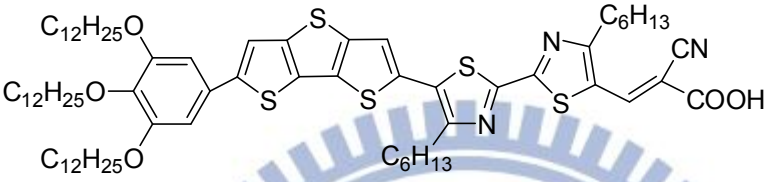

Cpd22

Figure 5.1 Chemical structures of dyes **Cpd11**, **Cpd16**, and **Cpd22**.

Table 5.1 Absorption, emission, and electrochemical properties of dyes

Dyes	λ_{abs} nm [a] (ε, $M^{-1}cm^{-1}$)	λ_{PL} [a] (nm)	Stokes Shift[b] (nm)	E_g[c] (eV)	E_{ox}[d] (V)	HOMO[e] (eV)	LUMO[f] (eV)
Cpd11	443 (99000)	557	114	2.45	1.15	-5.70	-3.25
Cpd16	386 (35700), 476 (75000)	624	148	2.19	0.71	-5.26	-3.07
Cpd22	374 (58000), 473 (77000)	610	137	2.15	0.77	-5.32	-3.17

[a] The absorption and PL emission wavelength recorded in dilute THF solution(10^{-5} M) at room temperature.

[b] Stokes shift has been calculated from the difference between λ_{abs} and λ_{PL}.

[c] The optical band gap was obtained from the equation $E_g^{opt} = 1240/\lambda_{onset}$

[d] E_{ox} was the oxidation potential.

[e] E_{HOMO} = [-(E_{ox} - 0.25) - 4.8] eV where 0.25 V is the value for ferrocene vs. Ag/Ag^+ and 4.8 eV is the energy level of ferrocene below the vacuum.

[f] $E_{LUMO} = E_{HOMO} - E_g$

(a)

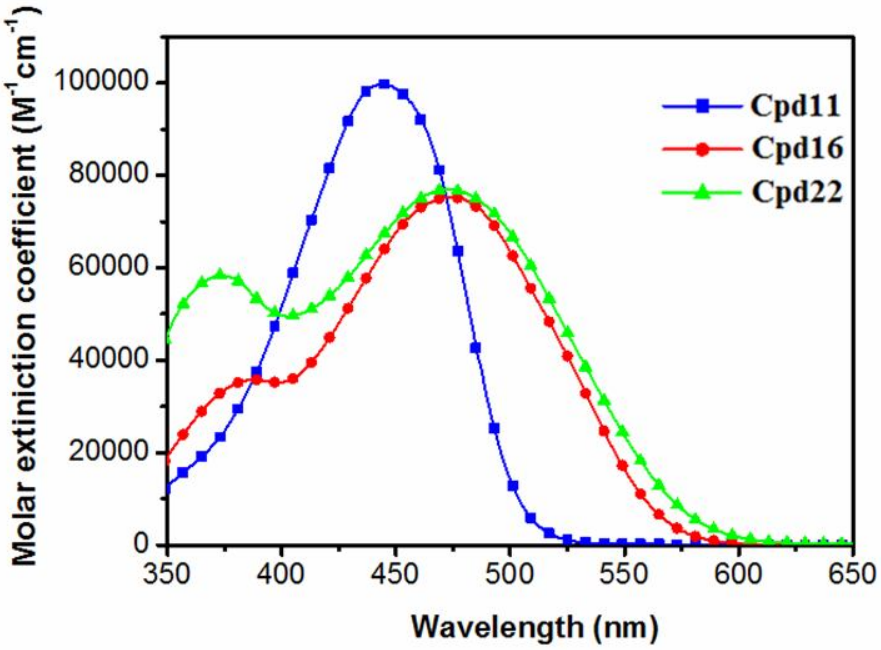

(b)

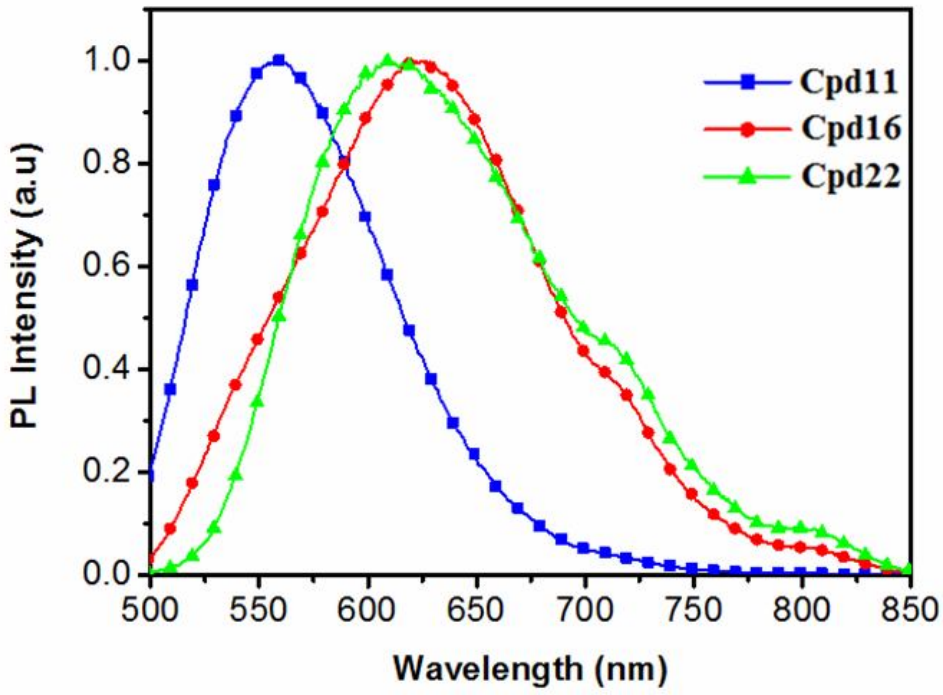

Figure 5.2 (a) UV-vis absorption spectra of metal-free organic dyes in THF solutions (10^{-5} M) and (b) Normalized photoluminescence (PL) spectra of metal-free organic dyes in THF solutions (10^{-5} M).

5.3.2. Electrochemical properties

The electrochemical properties of dyes can be obtained using cyclic voltammetry (CV); Table 5.1 and Figure 5.3 present the relevant CV data and representative cyclic voltammograms, respectively, for **Cpd11**, **Cpd16**, and **Cpd22**. We determined the HOMO energy levels of these dyes from their corresponding irreversible oxidation peaks. The cyclic voltammograms of the dyes **Cpd11**, **Cpd16**, and **Cpd22** featured irreversible oxidation waves with oxidation potentials of 1.15, 0.71, and 0.77 V, respectively (Figure 5.3). The HOMO energy level of a dye must be more positive (>0.3 eV) than the electrolyte iodine redox potential if it is to accept electrons effectively.[141-146] The HOMO energy levels of our dyes were in the range from –5.70 to –5.26 eV with respect to the I^-/I_3^- redox couple (–4.60 eV vs. vacuum). Because of the absence of reduction peaks, we could not determine the LUMO energy levels of these dyes from the CV traces, but we could elucidate them by subtracting the optical band gaps from the HOMO energy levels. The resulting LUMO energy levels, in the range from –3.07 to –3.25 eV, are higher than the conduction band edge (–4.0 eV vs. vacuum); therefore, the electron injection process is energetically favorable. Relative to **Cpd11** (containing only a simple fused dithienothiophene spacer), the dyes **Cpd16** (with one more bithiophene unit) and **Cpd22** (with one more bithiazole unit) both had smaller oxidation potentials (E_{ox}). Therefore, the shortest spacer in **Cpd11** (possessing

the shortest conjugation length) resulted in it having the highest oxidation potential and the largest optical band gap (E_g) among our tested dyes. The optical bandgaps of **Cpd11**, **Cpd16**, and **Cpd22** were 2.45, 2.19, and 2.15 eV, respectively, which suggested that **Cpd22** possibly might have a higher PCE value. However, in contrast to **Cpd11** (without a donor bithiophene linkage) and **Cpd22** (with an acceptor bithiazole linkage), the improved electron injection of **Cpd16** might be arisen from the donor bithiophene linkage and hence to achieve a higher PCE value. On the other hand, since the HOMO and LUMO levels of **Cpd16** obtained from CV measurements were found to be higher than those of **Cpd11** and **Cpd22** in Table 5.3, and hence a greater electron injection process was favorable to obtain a higher PCE efficiency in later photovoltaic measurements.

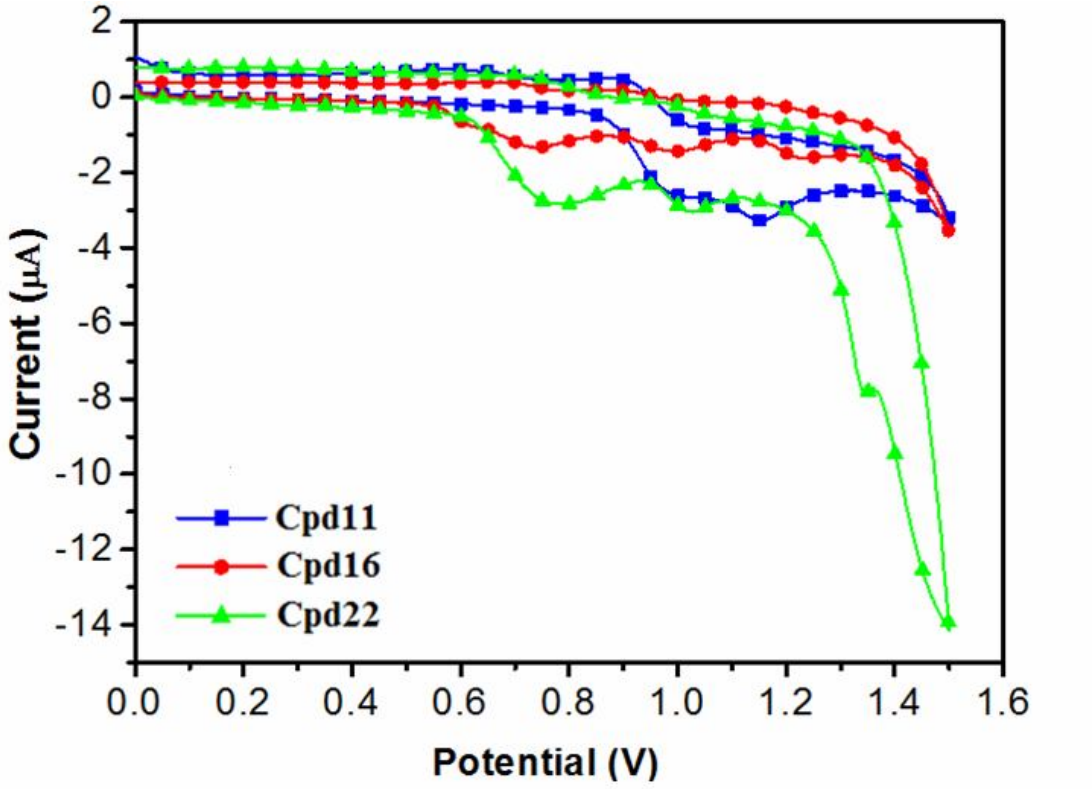

Figure 5.3 Cyclic voltammograms of dyes (in THF) at a scan rate of 100 mV/s.

5.3.3. Mesomorphic properties

Table 5.2 lists the phase transition temperatures and enthalpies of the dyes **Cpd11**, **Cpd16**, and **Cpd22**, as characterized using differential scanning calorimetry (DSC). The polarizing optical microscopy (POM) image in Figure 5.4 reveals that **Cpd16** possessed a tilted smectic (SmC) phase, with a broken focal conic fan texture at 225 °C. The mesomorphic properties of **Cpd16** were confirmed using powder X-ray diffraction (XRD); after thermal annealing at 225 °C for 10 min, **Cpd16** exhibited a primary diffraction feature in the low angle region of Figure 5.4, with a sharp peak at a value of 2θ of 1.3° (corresponding to a *d*-spacing of 50.6 Å). Figure 5.5 presents a

possible packing motif (side-view) for **Cpd16**; this model suggests that the dye molecules stacked with bilayer packing and may have trivial interdigitated arrangements as a result of hydrogen bonding interactions between terminal carboxyl (COOH) units. Using Chemdraw software for simulation, we calculated the theoretical molecular length of **Cpd16** to be 38.44 Å; its hydrogen-bonded dimer would, therefore, have a length of ~75 Å. The *d*-spacing of 50.6 Å for **Cpd16**, determined using XRD, suggested a tilted smectic molecular arrangement (e.g., SmC phase) in Figure 5.5. The broad peak in the wide angle region at a value of 2θ of 15° in Figure 5.4 corresponds to a *d*-spacing of 4.6 Å, which we assign to the lateral distance between the conjugated backbones, as has been reported for other similar π-conjugated polymers presenting long pendants,[145-147] although this broad peak might also have contained some contributions from the lateral π–π stacking of the dye planes.[148] The broad XRD halos in Figure 5.4 suggest, however, that π–π stacking in **Cpd16** occurred only in very small areas; that is, it mainly possessed an amorphous structure.[149]

Table 5.2 Phase transition temperatures and enthalpies of the dyes **Cpd11**, **Cpd16**, and **Cpd22**

		Phase transition (°C, [ΔH (J g^{-1})])[a,b]
Cpd11	Heating	$Cr_1$105.83[3.67] $Cr_2$155.7[6.01] $Cr_3$165.65[8.3]Iso
	Cooling	Iso146.21[7.88] $Cr_3$130.46[1.9] $Cr_2$87.83[3.17] Cr_1
Cpd16	Heating	$Cr_1$182.99[4.9]$Cr_2$218.12[19.34]SmC242.52[2.01]Iso
	Cooling	Iso[c]235.2 SmC175.10[2.04] $Cr_2$142.78[1.54] Cr_1
Cpd22	Heating	Cr202.91[4.7]Iso
	Cooling	Iso194.97[3.3] Cr

[a] Data determined through DSC from second heating/first cooling run at a scanning rate of 5 °C min^{-1}.

[b] Abbreviations: Cr_{1-3}, different crystalline modifications; SmC, tilted smectic phase; Iso, isotropic liquid state.

[c] Isotropic temperature determined through POM.

(a)

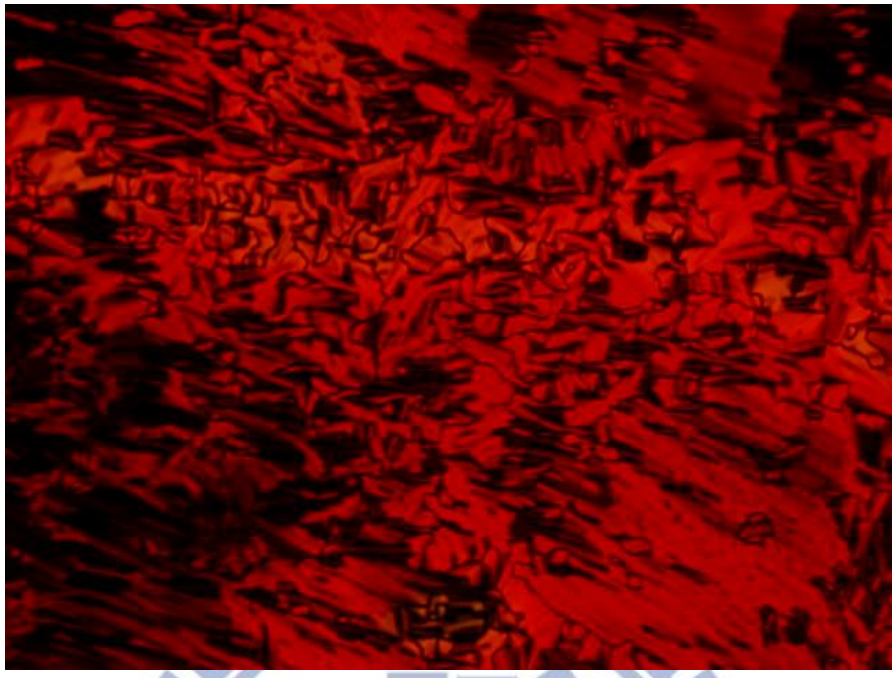

(b)

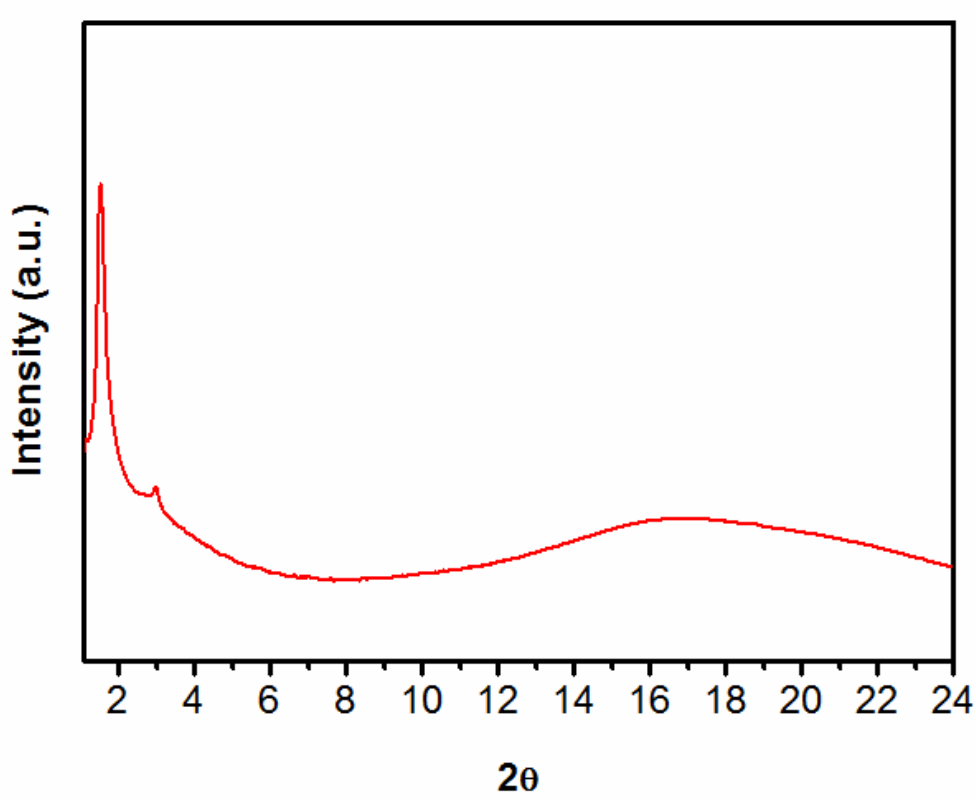

Figure 5.4 (a) Optical texture of the nematic phase in dye **Cpd16** observed by POM at 225 °C (cooling) and (b) XRD intensity against angle profiles obtained from dye **Cpd16** at 225 °C.

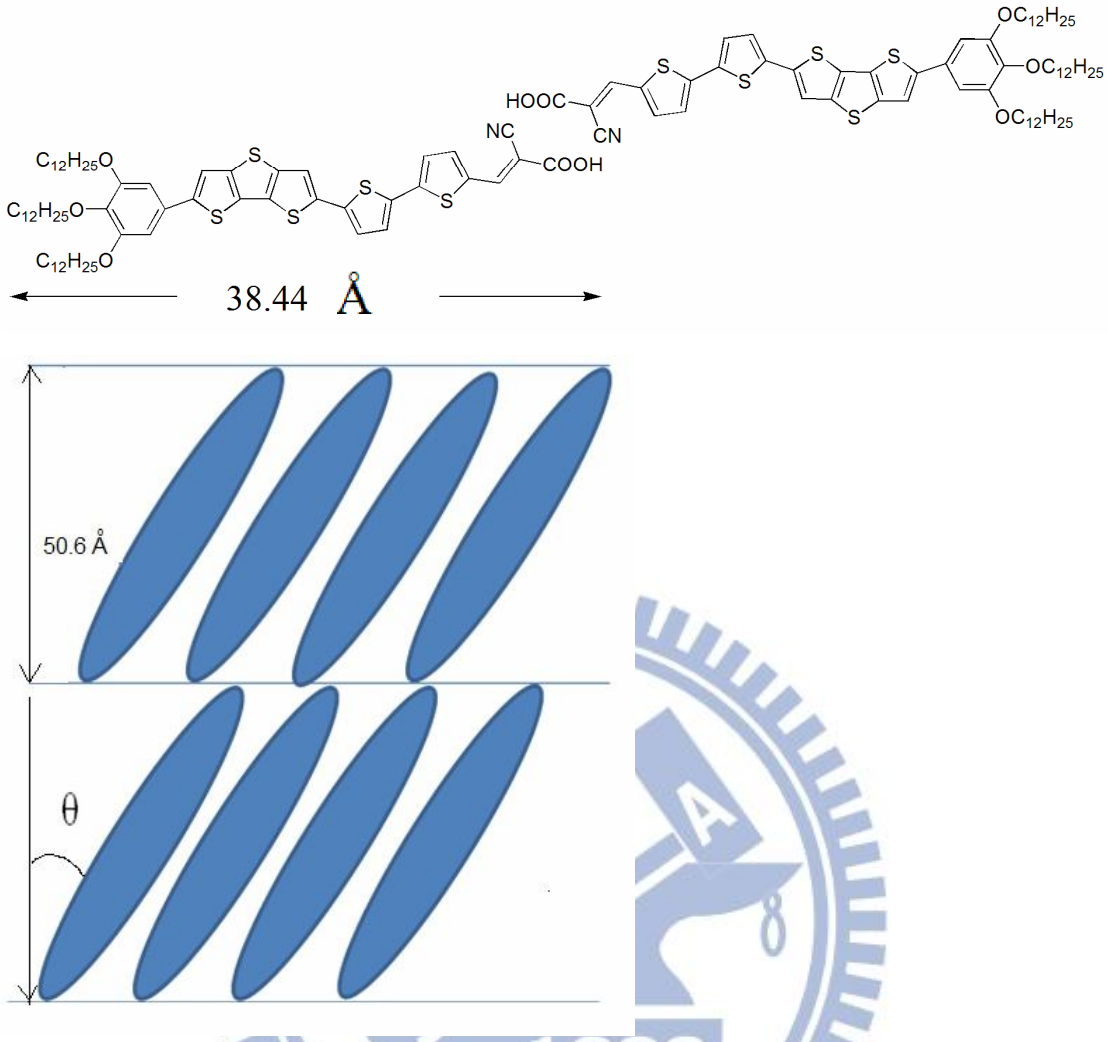

Figure 5. 5 Molecular modeling of dye **Cpd16**.

5.3.4. Photovoltaic properties of DSSCs

Figure 5.6 displays incident photon-to-current conversion efficiency (IPCE) and photocurrent–voltage (*I–V*) curves of DSSCs based on the dyes **Cpd11**, **Cpd16**, **Cpd22**, and N719. From Figure 5.6b, we characterized the photovoltaic parameters of the DSSCs (Table 5.3), namely their open-circuit photovoltages (V_{OC}), short-circuit photocurrent densities (J_{SC}), fill factors (FFs), and solar-to-electrical energy conversion efficiencies (η). The power conversion efficiencies (PCEs, i.e., η) followed the trend **Cpd16** (η = 3.72) > **Cpd22** (η = 2.82) > **Cpd11** (η = 2.69). The highest PCE was that of the DSSC incorporating **Cpd16**, mainly because it had the highest short current density (J_{sc} = 9.98 mA cm^{-2}), which reveals more electrons were transferred from the excited state of the dye and injected into the conduction band of TiO_2; the DSSCs incorporating the three dyes each had similar values of V_{oc} and FF. The IPCE spectrum of **Cpd16** (Figur 5.6a) featured the broadest response in the range 300–750 nm with a maximum IPCE value of 64%; this behavior is consistent with its DSSC having the highest PCE (η = 3.72; with V_{OC} = 0.58 V; J_{SC} = 9.98 mA cm^{-2}; and FF = 0.65). Thus, the highest PCE (η = 3.72) for the device incorporating **Cpd16** resulted from its high short current intensity (J_{sc} = 9.98 mA cm^{-2}) and broadest and most-intense IPCE spectrum (toward the longer wavelength region), both of which presumably resulted from the longer conjugated structure induced by this dye's

additional bithiophene linker. The different PCE values of **Cpd11**, **Cpd16**, and **Cpd22** may be attributed to the following reasons; (i) **Cpd16** and **Cpd22** were bridged through a donor bithiophene linkage and an acceptor bithiazole linkage, respectively, in contrast to **Cpd11**; (ii) The steric effect induced by the lateral alkyl chains of the bithiazole unit might affect the conjugation of **Cpd22**; (iii) As noticed in Fig. 4, the greater packing nature of **Cpd16** enhanced the electron injection to TiO_2 and also enhanced J_{SC} to obtain a higher PCE value.

Table 5.3 Cell performance of **Cpd11**, **Cpd16**, **Cpd22**, and **N719**-sensitized solar cells

DSSC	V_{oc} (V)	J_{sc} (mA cm^{-2})	FF (%)	η (%)
Cpd11	0.57	–6.85	0.70	2.69
Cpd16	0.58	–9.98	0.65	3.72
Cpd22	0.60	–6.77	0.70	2.82
N719	0.70	–15.41	0.65	7.04

[a] Measured under AM 1.5 irradiation, 100 mW cm^{-2}.

(a)

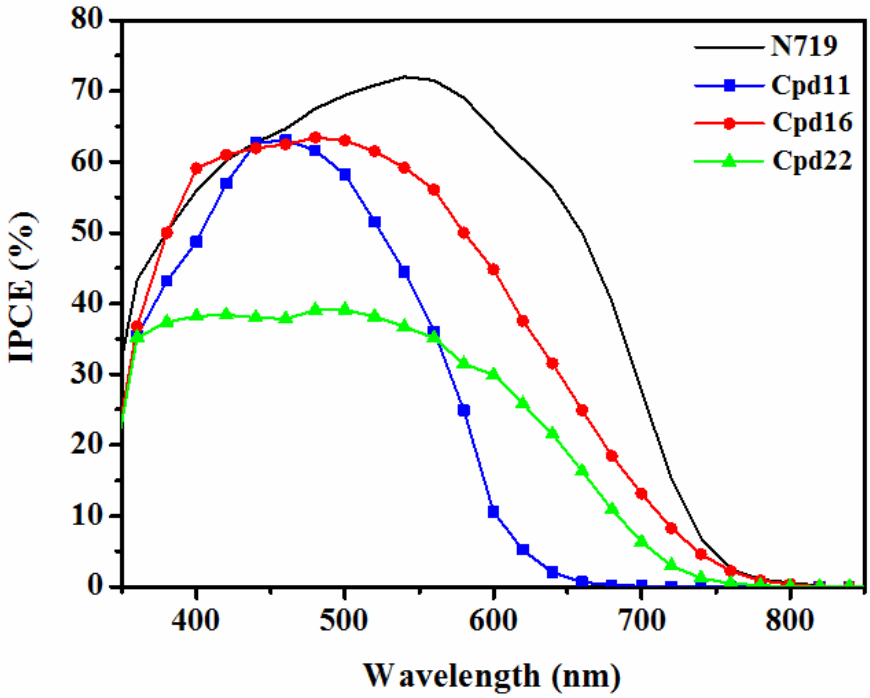

(b)

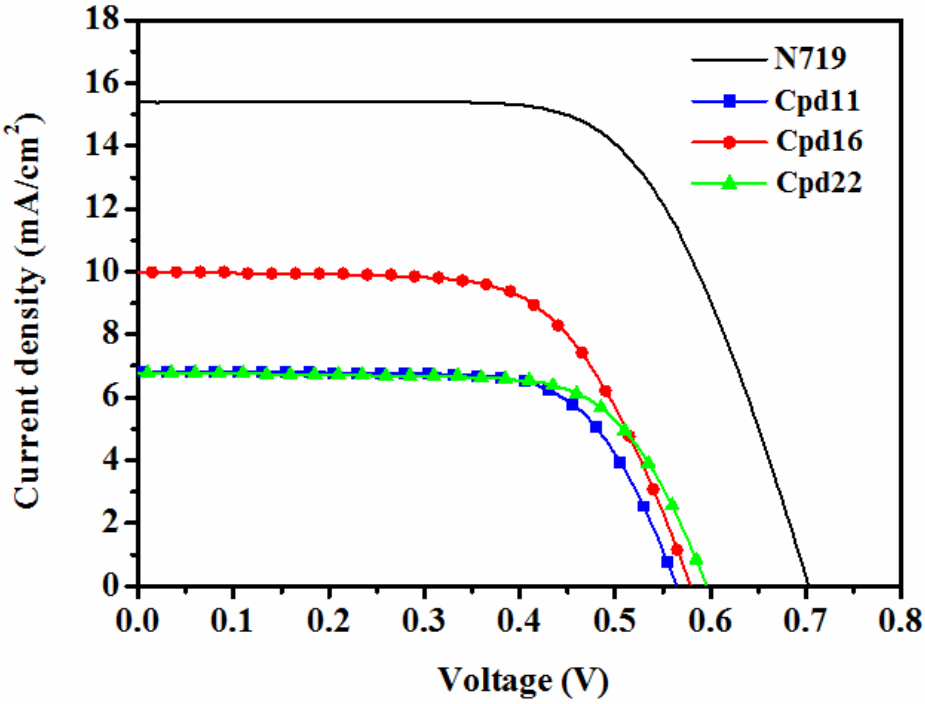

Figure 5.6 (a) IPCE plots of DSSCs fabricated using dyes **Cpd11, Cpd16, Cpd22**, and **N719**. **(b)** I-V curves of DSSCs based on dyes **Cpd11, Cpd16, Cpd22**, and **N719**.

5.4 Conclusions

We have synthesized three new metal-free organic dyes (**Cpd11**, **Cpd16**, and **Cpd22**), each featuring a tris(dodecyloxy)phenyl moiety (a common unit in liquid crystalline structures) as an electron donor, a cyanoacrylic acid moiety as an electron acceptor/anchoring group, and a DTT-based spacer to bridge the donor and acceptor moieties. To extend the length of conjugation, we appended a bithiophene or bithiazole moiety to the DTT unit to enhance the capacity for charge transfer and increase the range of absorption. The dye **Cpd16** exhibited mesomorphic properties, resulting from the appropriate ratio of the lengths of its flexible chain to its rigid core; molecular modeling of **Cpd16**, and its *d*-spacing value determined using XRD, verified the existence of a tilt angle in the SmC phase. In addition, among the tested dyes, the DSSC exhibiting the best performance was that incorporating **Cpd16**, presumably because of its superior packing as a result of its mesomorphic properties. This DSSC exhibited a maximum PCE of 3.72% (V_{oc} = 0.58 V; J_{sc} = 9.98 mA cm^{-2}; FF = 0.65) under simulated AM 1.5 irradiation (100 mW cm^{-2}).

Chapter 6

Conclusion

First, the concept of supermolecular interactions, such as H-bonds formed between conjugated polymers (**PCA** and **PCB**) and surface-modified nanoparticles ZnO (**ZnOpy**), has been introduced by the syntheses of **ZnOpy** nanoparticles and two fused dithienothiophene/carbazole-based polymers. The band gaps and the HOMO/LUMO energy levels of these resulting copolymers can be finely tuned as demonstrated by the investigation of optical absorption properties and electrochemical studies. The pyridyl surfactants of **ZnOpy** nanoparticles (as electron acceptors to partially replace expensive electron acceptor PCBM) not only induce supramolecular interactions with benzoic acid pendants of polymer **PCB** via H-bonds, but also enhance the homogeneous dispersions of **ZnOpy** nanoparticles in polymer **PCB**. Thus, the PSC device containing ternary components of polymer **PCB** blended with **ZnOpy** and PCBM acceptors (**PCB**:**ZnOpy**:PCBM=1:0.05:1) had the power conversion efficiency of up to 0.55%, which gave the best performance with the values of I_{sc}=2.11mA/cm^2, FF=29.4%, and V_{oc}=0.88 V.Second, We have successfully synthesized three dithienothiophene/ carbazole-based conjugated polymers (**PCC**, **PCA** and **PCB**) by Suzuki coupling reaction. Interestingly, **PCC**, **PCA** and **PCB** exhibited reversible electrochromism during the oxidation processes of cyclic

voltammogram studies. Among **PCC**, **PCA** and **PCB**, polymer **PCB** (with H-bonds) revealed the best electrochromic property with the most noticeable color change. In powder X-ray diffraction (XRD) measurements, these polymers exhibited obvious diffraction features indicating distinct bilayered packings between polymer backbones and similar p-p stacking between layers in the solid state. Compared with the XRD data of **PCA** (without H-bands), H-bonds of **PCB** induced a higher crystallinity in the small angle region (corresponding to a higher ordered bilayered packings between polymer backbones), but with a similar crystallinity in the wide angle region indicating a comparable π–π stacking distance between layers. The potential applications of **PCC**, **PCA** and **PCB** in bulk heterojunction photovoltaic solar cells (PSCs) were further investigated, where the PSC device containing **PCB** blended with PCBM (by a weight ratio of 1:1) had the optimum power conversion efficiency (PCE) up to 0.61% (with J_{sc} = 2.26 mA/cm^2, FF = 29.8%, and V_{oc} = 0.90 V). Due to the H-bonded effects, polymer **PCB** possessed higher thermal decomposition temperature (T_d), glass transition temperature (T_g), RMS smoothness, open circuit voltage (V_{oc}), and PCE value than **PCA**. These polymers demonstrate a novel family of conjugated polymers along the path toward achieving the electrochromic and PSC applications.

Third, We synthesized a series of metallo-polymers (**P1-P4**) with aryl-imidazo-phenanthrolines (AIP) units (incorporated with phenyl and fused

dithienothiophene groups in different donor spacers) to study for their electrochemical and electrochromic properties. In order to investigate the energy transfers between metallo-polymers (**P1-P4**) and nanoparticle **ZnOpy**, novel supramolecular nanocomposites **P3-P4**/**ZnOpy** were constructed by complexation of proton donor (H-donor) metallo-polymers **P3-P4**, consisting of carboxylic acid groups, with proton accepter (H-accepter) **ZnOpy**. They were compared with nanocomposites **P1-P2**/**ZnOpy** containing metallo-polymers **P1-P2** without carboxylic acid groups to have no H-bonded interactions with nanoparticle **ZnOpy**. In contrast to amorphous metallo-polymers **P3-P4** from XRD measurements, supramolecular nanocomposites **P3-P4**/**ZnOpy** exhibited obvious diffraction features (originated from metallo-polymers **P3-P4**) indicating the increased crystallinities of **P3-P4** upon addition of **ZnOpy**, due to the supramolecular (H-bonded) interactions. TEM morphologies also proved that the supramolecular (H-bonded) interactions between **ZnOpy** and polymers **P3-P4** induce nanoparticles to be homogeneously dispersed in nanocomposites **P3-P4**/**ZnOpy**.

Finally, We have synthesized three new metal-free organic dyes (**Cpd11**, **Cpd16**, and **Cpd22**), each featuring a tris(dodecyloxy)phenyl moiety (a common unit in liquid crystalline structures) as an electron donor, a cyanoacrylic acid moiety as an electron acceptor/anchoring group, and a DTT-based spacer to bridge the donor and acceptor

moieties. To extend the length of conjugation, we appended a bithiophene or bithiazole moiety to the DTT unit to enhance the capacity for charge transfer and increase the range of absorption. The dye **Cpd16** exhibited mesomorphic properties, resulting from the appropriate ratio of the lengths of its flexible chain to its rigid core; molecular modeling of **Cpd16**, and its *d*-spacing value determined using XRD, verified the existence of a tilt angle in the SmC phase. In addition, among the tested dyes, the DSSC exhibiting the best performance was that incorporating **Cpd16**, presumably because of its superior packing as a result of its mesomorphic properties. This DSSC exhibited a maximum PCE of 3.72% (V_{oc} = 0.58 V; J_{sc} = 9.98 mA cm^{-2}; FF = 0.65) under simulated AM 1.5 irradiation (100 mW cm^{-2}).

References

1. Gunes, S.; Neugebauer, H.; Sariciftci, N. S. *Chem. Rev.* **2007**, 107, 1324.

2 Yu, G.; Gao, J.; Hummelen, J. C.; Wudl, F.; Heeger, A. J. *Science* **1995**, 270, 1789.

3 Thompson, B. C. ; Fréchet, J. M. J. *Angew. Chem. Int. Ed.* **2008**, *47*, 58.

4 Coffey, D. C.; Reid, O. G.; Rodovsky, D. B.; Bartholomew, G. P.; Ginger, D. S. *Nano Lett.* **2007**, *7*, 738.

5 (a) Moule, A. J.; Meerholz, K. *Adv. Mater.***2008**, *20*, 240. (b) Li, L.; Lu, G. H.; Yang, X. *J. Mater. Chem.* **2008**, *18*, 1984. (c) Chang, Y. M.; Wang, L. J. Phys. Chem. C **2008**, *112*, 17716. (d) Yao, Y.; Hou, J. H.; Xu, Z.; Li, G.; Yang, Y. *Adv. Funct. Mater.* **2008**, *18*, 1783.

6 (a) Liang, Y.; Feng, D.; Wu, Y.; Tsai, S. T.; Li, G.; Ray, C.; Yu, L. *J. Am. Chem. Soc.* **2009**, *131*, 7792. (b) Hou, J.; Chen, H. Y.; Zhang, S.; Chen, R. I.; Yang, Y.; Wu, Y.; Li, G. *J. Am. Chem. Soc.* **2009**, *131*, 15586. (c) Park, S. H.; Roy, A.; Beaupre, S.; Cho, S.; Coates, N.; Moon, J. S.; Moses, D.; Leclerc, M.; Lee, K.; Heeger, A. J. *Nat. Photonics* **2009**, *3*, 297. (d) Liang, Y.; Xu, Z.; Xia, J.; Tsai, S. T.; Wu, Y.; Li, G.; Ray, C.; Yu, L. *Adv. Mater.* **2010**, *22*, 135. (e) Chen, H. Y.; Hou, J.; Zhang, S.; Liang, Y.; Yang, G.; Yang, Y.; Yu, L.; Wu, Y.; Li, G. *Nat. Photonics* **2009**, *3*, 649.

7 (a) Scharber, M. C.; Muhlbacher, D.; Koppe, M.; Denk, P.; Waldauf, C.; Heeger, A.

J.; Brabec, C. J. *Adv. Mater.* **2006**, *18*, 789. (b) Gunes, S.; Neugebauer, H.; Sariciftci, N. S. *Chem. Rev.* **2007**, *107*, 1324.

8 Beek, W. J. E.; Wienk, M. M.; Janssen, R. A. J. *Adv. Mater.* **2004**, *16*, 1009.

9 Koster, L. J. A.; Strien, W. J. V.; Beek, W. J. E.; Blom, P.W. M. *Adv. Funct. Mater.* **2007**, *17*, 1297.

10 Freitas, J. N. D.; Grova, I. R.; Akcelrud, L. C.; Arici, E.; Sariciftcic, N. S.; Nogueira, A. F. *J. Mater. Chem.* **2010**, *20*, 4845.

11 Bonifazi, D.; Kiebele, A.; Stöhr, M.; Cheng, F.; Jung, T.; Diederich, F.; Spillmann, H. Adv. Funct. Mater. **2007**,*17*,1051.

12 (a) Wurthner, F.; Chen, Z.; Hoeben, F. J. M.; Osswald, P.; You, C. C.; Jonkheijm, P. *J. Am. Chem. Soc.* **2004**, *126*, 10611. (b) Hoeben, F. J. M.; Zhang, J.; Lee, C. C.; Pouderoijen, M. J.; Wolffs, M.; Wurthner, F. *Chem. Eur. J.* **2008**, *14*, 8579. (c) El-ghayoury, A.; Schenning, A. P. H. J.; Hal, P. A. V.; Duren, J. K. J. V.; Janssen, R. A. J.; Meijer, E. W. *Angew. Chem. Int. Ed. Engl.* **2001**, *40*, 3660. (d) Jonkheijm, P.; Duren, J. K. J. V.; Kemerink, M.; Janssen, R. A. J.; Schenning, A. P. H. J.; Meijer, E. W. *Macromolecules* **2006**, *39*, 784. (e) Moulé, A. J.; Tsami, A.; Bünnagel, T.W.; Forster, M.; Kronenberg, N. M.; Scharber, M.; Koppe, M.; Morana, M.; Brabec, C. J.; Meerholz, K.; Scherf, U. *Chem. Mater.* **2008**, 20, 4045.

13 Liu, Y.; Xiao, S.; Li, H.; Li, Y.; Liu, H.; Lu, F.; Zhuang, J.; Zhu, D. *J. Phys. Chem. B* **2004**, *108*, 6256.

14 Mishra, A.; Fischer, M. K. R.; Bäuerle, P. *Angew. Chem. Int. Ed*. **2009**, *48*, 2474.

15 Chen, C. Y.; Chen, J. G.; Wu, S. J.; Li, J. Y.; Wu, C. G.; Ho, K. C. *Angew. Chem. Int. Ed*. **2008**, *47*, 7342.

16 O'Regan, B.; Grätzel, M. *Nature* **1991**, *353*, 737.

17 Grätzel, M. *Nature* **2001**, *414*, 338.

18 Abbotto, A.; Barolo, C.; Bellotto, L.; De Angelis, F.; Grätzel, M.; Manfredi, N.; Marinzi, C.; Fantacci, S.; Yum, J. H.; Nazeeruddin, M. K.; *Chem. Commun*. **2008**, 5318.

19 Kim, H.; Kim, S.; Park, C.; Jang, S. H.; Kim, C. J.; Kim, K.; Park, N. G.; Kim, C. *Chem. Comm*. **2010**, *46*, 1335.

20 Tang, J.; Wu, W.; Hua, J.; Li, J.; Li, X.; Tian, H. *Energy Environ. Sci*. **2009**, *2*, 982.

21 Yin, J. F.; Chen, J. G.; Lu, Z. Z.; Ho, K. C.; Lin, H. C.; Lu, K. L. *Chem. Mater*. **2010**, *22*, 4392.

22 Yin, J. F.; Bhattacharya, D.; Hsu, Y. C.; Tsai, C. C.; Lu, K. L.; Lin, H. C.; Chen, J. G. ; Ho, K. C. *J. Mater. Chem*. **2009**, *19*, 7036.

23 Wang, Z. S.; Cui, Y.; Dan-oh, Y.; Kasada, C.; Shinpo, A.; Hara, K. *J. Phys. Chem. C* **2007**, *111*, 7224.

24 Horiuchi, T.; Miura, H.; Uchid, S. *Chem. Commun*. **2003**, 3036.

25 Clifford, J. N.; Martı´nez-Ferrero, E.; Viterisi, A.; Palomares, E. *Chem. Soc. Rev.* **2011**, *40*, 1635.

26 Hagfeldt, A.; Boschloo, G.; Sun, L. C.; Kloo, L.; Pettersson, H. *Chem. Rev.* **2010**, *110,* 6595.

27 Do, K.; Kim, D.; Cho, N.; Paek, S. H.; Song, K. Y.; Ko, J. J. *Org. Lett*. **2012**, *14*, 222.

28 Guo, K. P.; Yan, K. Y.; Lu, X. Q. ; Qiu, Y. C.; Liu, Z.; Sun, J. W. ; Yan, F.; Guo, W. Y.; Yang, S.; *Org. Lett*. **2012**, *14*, 2214.

29 Lu, X. F.; Feng, Q. Y.; Lan, T.; Zhou, G.; Wang, Z. S. *Chem. Mater*. **2012**, *24*, 3179.

30 Sahu, D.; Padhy, H.; Patra, D.; Yin, J. F.; Hsu, Y. C.; Lin, J. T.; Lu, K. L.; Wei, K. H.; Lin, H.C. *Tetrahedron* **2011**, *67*, 303.

31 Zhou, H. P.; Xue, P. C.; Zhang, Y.; Zhao, X.; Jia, J. H.; Zhang, X. F.; Liu, X. L.; Lu, R. *Tetrahedron* **2011**, *67*, 8477.

32 Li, Y. T.; Chen, C. L.; Hsu, Y. Y.; Hsu, H. C.; Chi, Y.; Chen, B. S.; Liu, W. H.; Lai, C. H.; Lin, T. Y.; Chou, P. T. *Tetrahedron* **2010**, *66*, 4223.

33 Whittell, G. R.; Hager, M. D.; Schubert, U. S.; Manners, I. *Nature Materials* **2011**, *10*, 176.

34 Guo, M.; Diao, P.; Ren, Y. J.; Meng, F.; Tian, H.; Cai, S. M.; *Sol. Energy Mater. Sol. Cells* **2005**, *88*, 23.

35 Yasuda, T.; Ooi, H.; Morita, J.; Akama, Y.; Minoura, K.; Funahashi, M.; Shimomura, T.; Kato, T. *Adv. Funct. Mater*. **2009**, *19*, 411.

36 Shunmugam, R.; Gabriel, G. J.; Aamer, K. A.; Tew, G. N. *Macromol. Rapid Commun.***2010,** *31*, 784.

37 Wojtecki, R. J.; Meador, M. A.; Rowan, S. J. *Nature Mater.* **2011**, *10*, 14.

38 Astruc, D.; Chardac, F. *Chem. Rev.* **2001**, *101*, 2991.

39 Astruc, D.; Boisselier, E.; Ornelas, C. *Chem. Rev.* **2010**, *110*, 1857.

40 (a) Gong, D. R.; Wang, B. L.; Bai, C. X.; Bi, J. F.; Wang, F.; Dong, W. M.; Zhang, X. Q.; Jiang, L. S. Polymer **2009**, *50*, 6259. (b) Zhao, X.; Luo, X. X.; Li, B.; Song, H. B.; Xu, S. S.; Wang, B. Q. Eur. Polym. J. **2008**, *44*, 3264.

41 (a) Zhu, X. J.; Holliday, B. J. Macromol. Rapid Commun. **2010**, *3*, 904. (b) Guchhait, A.; Rath, A. K.; Pal, A. J. Chem. Mater. **2009**, *21*, 5292. (c) Skompska, M. Synth. Met. **2010**, *160*, 1.

42 (a) Chan, H. T.; Mak, C. S. K.; Djurisic, A. B.; Chan, W. K. Macromol. Chem. Phys. **2011**, *212*, 774. (b) Cheung, W. K.; Mak, C. S. K.; Chan, W. K. Macromol.

Rapid Commun. **2012**, *33*, 585.

43 (a) Burnworth, M.; Mendez, J. D.; Schroeter, M.; Rowan, S. J.; Weder, C. Macromolecules **2008**, *41*, 2157. (b) Pefkianakis, E. K.; Tzanetos, N. P.; Kallitsis, J. K. Chem. Mater. **2008**, *20*, 6254. (c) Happ, B.; Friebe, C.; Winter, A.; Hager, M. D.; Schubert, U. S. Eur. Polym. J. **2009**, *45*, 3433. (d) Sun, T. X.; Wang, Q.; Fan, Z. Q. Polymer **2010**, *51*, 3091.

44 (a) Dong, T. Y.; Lin, M. C.; Chang, S. W.; Ho, C. C.; Lin, S. F.; Lee, L. J. Org. Chem. **2007**, *692*, 2324. (b) Winter, A.; Friebe, C.; Chiper, M.; Hager, M. D.; Schubert, U. S. J. Polym. Sci., Part A: Polym. Chem. **2009**, *47*, 4083.

45 (a) Schulz, G. L.; Holdcroft, S. Chem. Mater. **2008**, *20*, 5351. (b) Williams, K. A.; Boydston, A. J.; Bielawski, C. W. Chem. Soc. Rev. **2007**, *36*, 729. (c)Yd, M. M.; Kaya, I. M. Polymer **2009**, *50*, 5653.

46 (a) Schlutter, F.; Wild, A.; Winter, A.; Hager, M. D.; Baumgaertel, A.; Friebe, C.; Schubert, U. S. Macromolecules **2010**, *43*, 2759. (b) Qi, S. L.; Wu, Z. P.; Wu, D. H.; Yang, W. T.; Jin, R. G. Polymer **2009**, *50*, 845.

47 (a) Padhy, H.; Sahu, D.; Chiang, I. H.; Patra, D.; Kekuda, D.; Chu, C.W.; Lin, H. C. J. Mater. Chem. **2011**, *21*, 1196. (b) Ramiro, P.; GarcFresnadillo, D.; Orellana, G. Tetrahedron **2005**, *61*, 9478. (c) Lee, C. H.; Zhang, Y. Y.; Romayanantakit, A.; Galoppini, E. Tetrahedron **2010**, *66*, 3897.

48 Yao, C. J.; Zhong, Y.W.; Nie, H. J.; Abruna, H. D.; Yao, J. J. Am. Chem. Soc. **2011**, *133*, 20720.

49 (a) Milum, K. M.; Kim, Y. N.; Holliday, B. J. Chem. Mater. **2010**, *22*, 2414. (b) Zhuang, J. P.; Zhou, W. D.; Li, X. F.; Li, Y. J.; Wang, N.; He, X. R.; Liu, H. B.; Li, Y. L.; Jiang, L.; Huang, C. S.; Cui, S.; Wang, S.; Zhu, D. B. Tetrahedron **2005**, 61,8686. (c) Eda, Y.; Itoh, K.; Ito, Y. N.; Kawato, T. Tetrahedron **2009**, 65, 282.

50 (a) Constable, E. C. Chem. Soc. Rev. **2007**, 36, 246. (b) Kim, B. S.; Basavaraja, C.; Jo, E. A.; Kim, D. G.; Huh, D. S. Polymer **2010**, 51, 3365.

51 (a) Miyashita, N.; Kurth, D. G. J. Mater. Chem. **2008**, *23*, 2636. (b) Batista, R. M. F.; Costa, S. P. G.; Belsley, M.; Lodeiro, C.; Raposo, M. M. M. Tetrahedron **2008**, *64*, 9230.

52 (a) He, M.; Zhang, F. J. Org. Chem. **2007**, *72*, 442. (b) Fang, H. P.; Lin, J. W.; Chiang, I. H.; Chu, C. W.; Wei, K. H.; Lin, H. C. J. Polym. Sci. Part A: Polym. Chem., **2012**, *50*, 5011.

53 (a) Chan, W. K. Coord. Chem. Rev. **2007**, *251*, 2104. (b) Torres, T.; Gouloumis, A.; Garcia, D. S.; Jayawickramarajah, J.; Seitz, W.; Guldi, D. M.; Sessler, J. L. Chem. Commun. **2007**, 292. (c) Chen, B. K.; Zhong, H. Z.; Li, R.; Zhou, Y.; Ding, Y. Q.; Li, Y. F.; Zou, B. S. Sci. Adv. Mater. **2012**, *4*, 342.

54 Wessendorf, F.; Gnichwitz, J. F.; Sarova, G. H.; Hager, K.; Hartnagel, U.; Guldi, D.

M.; Hirsch, A. *J. Am. Chem. Soc.* **2007**, *129*, 16057.

55 (a) Koster, L. J. A.; Strien, W. J. V.; Beek, W. J. E.; Blom, P. W. M. *Adv. Funct. Mater.* **2007**, *17*, 1297.

(b) Chu, C. C.; Raffy, G.; Ray, D.; Guerzo, A. D.; Kauffmann, B.; Wantz, G.; Hirsch, L.; Bassani, D. M. *J. Am. Chem. Soc.* **2010**, *132*, 12717.

56 Sahu, D.; Padhy, H.; Patra, D.; Yin, J.F.; Hsu, Y. C.; Lin, J. T.; Lu, K. L.; Wei, K. H.; Lin, H. C. *Tetrahedron* **2011**,*67*, 303.

57 Uhrich, C.; Schueppel, R.; Petrich, A.; Pfeiffer, M.; Leo, K.; Brier, E.; Kilickiran, P.; Baeuerle, P. Adv. Funct. Mater. **2007**, *17*, 2991.

58 Moet, D. J. D.; Koster, L. J. A.; Boer, B. de; Blom, P. W. M. Chem. Mater. **2007**, *19*, 5856.

59 Freitas, J. N. D.; Grova, I. R.; Akcelrud, L. C.; Arici, E.; Sariciftcic, N. S.; Nogueira, A. F. J. Mater. Chem. **2010**, *20*, 4845.

60 Blouin, N. ; Michaud, A. ; Leclerc, M. Adv. Mater. **2007**, *19*, 2295.

61 Li, J.; Dierschke, F.; J. Wu, A. C.; Grimsdale, K.; Müllen, J. Mater. Chem. **2006**, *16*, 96.

62 Morin, J. F.; Leclerc, M.; Adès, D.; Siove, A. Macromol. Rapid Commun. **2005**, *26*, 761.

63 Drolet, N.; Morin, J. F.; Leclerc, N.; Wakim, S.; Tao, Y.; Leclerc, M. Adv. Funct.

Mater. **2005**, *15*, 1671.

64 Leclerc, N.; Michaud, A. ; Sirois, K. ; Morin, J. F. ; Leclerc, M. Adv. Funct. Mater. **2006**, *16*, 1694.

65 Shiming, Z.; Haijun, F.; Yao, L.; Guangjin, Z.; Qikai, L.; Li, Y. F.,; Z., X. W., J. Polym. Sci. Part A: Polym. Chem. **2009**, *47*, 2843.

66 Li, K. C.; Huang, J. H.; Hsu, Y. C.; Huang, P. J.; Chu, C. W.; Lin, J. T.; Ho, K. C.; Wei, K. H.; Lin, H. C. Macromolecules **2009**, 42, 3681.

67 Li, J.; Qin, F.; Li, C. M.; Bao, Q. L.; Chan-Park, M. B.; Zhang, W.; Qin, J. G.; Ong, B. S. Chem. Mater. **2008**, *20*, 2057.

68 He, M.; Zhang, F. J. Org. Chem. **2007**, *72*, 442.

69 Dennler, G.; Scharber, M. C.; Brabec, C. J. Adv. Mater. **2009**, 21, 1323.

70 Hung, C. H.; Whang, W.T. J. Mater. Chem. **2005**, *15*, 267.

71 Mihailetchi, V. D.; Duren, J. K. J.; Blom, P. W. M.; Hummelen, J. C.; Janssen, R. A. J.; Kroon, J. M.; Rispens, M. T.; Verhees, W. J. H.; Wienk, M. M. Adv. Funct. Mater. **2003**, 13, 43.

72 Brabec, C. J.; Sariciftci, N. S.; Hummelen, J. C. Adv. Funct. Mater. **2001**, *11*, 15.

73 Shahid, M.; Ashraf, R. S.; Klemm, E.; Sensfuss, S. Macromolecules **2006**, *39*, 7844.

74 Hoppe, H.; Niggemann, M.; Winder, C.; Kraut, J.; Hiesgen, R.; Hinsch, A.;

Meissner, D.; Sariciftci, N. S. Adv. Funct. Mater. **2004**, *14*, 1005.

75 Yang, X.; Loos, J.; Veenstra, S. C.; Verhees, W. J. H. Wienk, M. M.; J. M.; Kroon, Michels, M. A. J.; Janssen, R. A. J. Nano Lett. **2005**, *5*, 579.

76 Hoppe, H.; Sariciftci, N.S. J. Mater. Chem. **2006**,*16*, 45.

77 (a) Liang, Y.; Feng, D.; Wu, Y.; Tsai, S. T.; Li, G.; Ray, C.; Yu, L. J. Am. Chem. Soc. **2009**, *131*, 7792. (b) Hou, J.; Chen, H. Y.; Zhang, S.; Chen, R. I.; Yang, Y.; Wu, Y.; Li, G. J. Am. Chem. Soc. **2009**, *131*, 15586. (c) Park, S. H.; Roy, A.; Beaupre, S.; Cho, S.; Coates, N.; Moon, J. S.; Moses, D.; Leclerc, M.; Lee, K.; Heeger, A. J. Nat. Photonics **2009**, *3*, 297. (d) Liang, Y.; Xu, Z.; Xia, J.; Tsai, S. T.; Wu, Y.; Li, G.; Ray, C.; Yu, L. Adv. Mater. **2010**, *22*, 135. (e) Chen, H. Y.; Hou, J.; Zhang, S.; Liang, Y.; Yang, G.; Yang, Y.; Yu, L.; Wu, Y.; Li, G. Nat. Photonics **2009**, *3*, 649.

78 (a) Scharber, M. C.; Muhlbacher, D.; Koppe, M.; Denk, P.; Waldauf, C.; Heeger, A. J.; Brabec, C. J. Adv. Mater. **2006**, 18, 789. (b) Gunes, S.; Neugebauer, H.; Sariciftci, N. S. Chem. Rev. **2007**, 107, 1324.

79 (a) Lia, J.; Grimsdale, A. C. Chem. Soc. Rev. **2010**, 39, 2399. (b) Tamura, K.; Shiotsuki, M.; Kobayashi, N.; Masuda, T.; Sanda, F. J. Polym. Sci. Part A: Polym. Chem. **2009**, 47, 3506. (c) Blouin, N.; Michaud, A.; Leclerc, M. Adv. Mater. **2007**, 19, 2295.

80 Fu, Y.; Kim, J.; Siva, A.; Shin, W. S.; Moon, S. J.; Park, T. J. Polym. Sci. Part A: Polym. Chem. **2011**, 49, 4368.

81 (a) Blouin, N.; Michaud, A.; Gendron, D.; Wakim, S.; Blair, E.; Neaguplesu, R.; Belletete, M.; Durocher, G.; Tao, Y.; Leclerc, M. J. Am. Chem. Soc. **2008**, *130*, 732. (b) Zou, Y.; Gendron, D.; Aich, R. B.; Najari, A.; Tao, Y.; Leclerc, M. Macromolecules **2009**, 42, 2891. (c) Qin, R. P.; Li, W. W.; Li, C. H.; Du, C.; Veit, C.; Schleiermacher, H. F.; Andersson, M.; Bo, Z. S.; Liu, Z. P.; Inganas, O.; Wuerfel, U.; Zhang, F. L. J. Am. Chem. Soc. **2009**, 131, 14612. (d) Zhang, M.; Fan, H.; Guo, X.; He, Y.; Zhang, Z.; Min, J.; Zhang, J.; Zhao, G.; Zhan, X.; Li, Y. Macromolecules **2010**, 43, 5706.

82 Ku, S. Y.; Liman, C. D.; Burke, D. J.; Treat, N. D.; Cochran, J. E.; Amir, E.; Perez, L. A.; Chabinyc, M. L.; Hawker, C. J. Macromolecules **2011**, 44, 9533.

83 Zhang, S. M.; Guo,Y. L.; Fan, H. J.; Liu, Y.; Chen, H. Y.;Yang, G. W.; Zhan, X. W.; Liu, Y. Q.; Li, Y. F.; Yang, Y. J. Polym. Sci. Part A: Polym. Chem. **2009**, 47, 5498.

84 (a) Gong, C.; Song, Q. L.; Yang, H. B.; Li, J.; Li, C. M. Sol. Energy Mater. Sol. Cells **2009**, 93, 1928. (b) Millefiorini, S.; Kozma, E.; Catellani, M.; Luzzati, S. Thin Solid Films **2008**, 516, 7205.

85 Zhan, X. W.; Tan, Z. A.; Domercq, B.; An, Z. S.; Zhang, X.; Barlow, S. J. Am.

Chem. Soc. **2007**, 129, 7246. (b) Tan, Z. A.; Zhou, E. J.; Zhan, X. W.; Wang, X.; Li, Y. F.; Barlow, S. Appl. Phys. Lett. **2008**, 93, 073309.

86 Huang, X. B.; Zhu, C. L.; Zhang, S. M.; Li, W. W.; Guo, Y. L.; Zhan, X. W. Macromolecules **2008**, 41, 6895.

87 Kim, K. H.; Chung, D. S.; Park, C. E.; Choi, D. H. J. Polym. Sci. Part A: Polym. Chem. **2011**, 49, 55.

88 Bae, W. J.; Scilla, C.; Duzhko, V. V.; Jo, W. H.; Coughlin, E. B. J. Polym. Sci. Part A: Polym. Chem. **2011**, 49, 3260.

89 Li, K. C.; Huang, J. H.; Hsu, Y. C.; Huang, P. J.; Chu, C. W.; Lin, J. T.; Ho, K. C.; Wei, K. H.; Lin, H. C. Macromolecules **2009**, 42, 3681.

90 Dennler, G.; Scharber, M. C.; Brabec, C. J. Adv. Mater. **2009**, *21*, 1323.

91 (a) Wu, C. W.; Tsai, C. M. Macromolecules **2006**, 39, 4298. (b) Wu, C. W.; Lin, H. C. Macromolecules **2006**, 39, 7232.

92 Coppo, P.; Cupertino, D. C.; Yeates, S. G.; Turner, M. L. Macromolecules **2003**, 36, 2705.

93 Brabec, C. J.; Sariciftci, N. S.; Hummelen. J. C. Adv. Funct. Mater. **2001**, 11, 15.

94 Shahid, M.; Ashraf, R. S.; Klemm, E.; Sensfuss, S. Macromolecules **2006**, 39, 7844.

95 Al-Ibrahima, M.; Rotha, H. K.; Zhokhavetsb, U. Sol. Energy Mater. Sol. Cells

2005, *85*, 13.

96 Mihailetchi, V. D.; Duren, J. K. J. V.; Blom, P. W. M.; Hummelen, J. C.; Janssen, R. A. J.; Kroon, J. M.; Rispens, M. T.; Verhees, W. J. H.; Wienk, M. M. Adv. Funct. Mater. **2003**, *13*, 43.

97 (a) Lu, G.; Usta, H.; Risko, C.; Wang, L.; Facchetti, A.; Ratner, M. A.; Marks, T. J. J. Am. Chem. Soc. **2008**, *130*, 7670. (b) Yasuda, T.; Sakai, Y.; Aramaki, S.; Yamamoto, T. Chem. Mater. **2005**, *17*, 6060. (c) Watanabe, K.; Osaka, I.; Yorozuya, S.; Akagi, K. Chem. Mater. **2012**, *24*, 1011.

98 (a) Patra, D.; Ramesh, M.; Sahu, D.; Padhy, H.; Chu, C. W.; Wei, K. H.; Lin, H. C. Polymer **201**2, 53, 1219. (b) Liang, T. C.; Lin, H. C. J. Polym. Sci. Part A: Polym. Chem. **2009**, 47, 2734. (c) Liang, T. C.; Lin, H. C. J. Mater. Chem. **2009**, 19, 4753.

99 (a) Kokubo, H.; Sato, T.; Yamamoto, T. Macromolecules **2006**, 39, 3959. (b) Yamamoto, T.; Arai, M.; Kokubo, H.; Sasaki, S. Macromolecules **2003**, 36, 7986.

100 (a) Wild, A.; Schlutter, F.; Pavlov, G. M.; Friebe, C.; Festag, G.; Winter, A.; Hager, M. D.; Cimrova V.; Schubert, U. S. Macromol. Rapid Commun. **2010**, 31, 868. (b) Banjoko, V.; Xu, Y. Q.; Mintz, E.; Pang, Y. Polymer **2009**, 50, 2001.

101 Wild, A.; Friebe, C.; Winter, A.; Hager, M. D.; Grummt, U.W.; Schubert, U. S.

Eur. J. Org. Chem. **2010**, 10, 1859.

102 Wessendorf, F.; Gnichwitz, J. F.; Sarova, G. H.; Hager, K.; Hartnagel, U.; Guldi, D. M.; Hirsch, A. J. Am. Chem. Soc. **2007**, *129*, 16057.

103 (a) Koster, L. J. A.; Strien, W. J. V.; Beek, W. J. E.; Blom, P.W. M. Adv. Funct. Mater. **2007**, *17*, 1297. (b) Chu, C. C.; Raffy, G.; Ray, D.; Guerzo, A. D.; Kauffmann, B.;Wantz, G.; Hirsch, L.; Bassani, D. M. J. Am. Chem. Soc. **2010**, *132*, 12717.

104 Sahu, D.; Padhy, H.; Patra, D.; Yin, J. F.; Hsu, Y. C.; Lin, J. T.; Lu, K. L.; Wei, K. H.; Lin, H. C. Tetrahedron **2011**, 67, 303.

105 (a) Fang, H. P.; Chiang, I. H.; Chu, C. W.; Yang, C. C.; Lin, H. C. Thin Solid Films **2011**, 519, 5212. (b) Jiu, T. G.; Liu, H. B.; Fu, L. M.; He, X. R.;Wang, N.; Li, Y. L.; Ai, X. C.; Zhu, D. B. Chem. Phys. Lett. **2004**, *398*, 113. (c) Liu, H. B.; Zuo, Z. C.; Guo, Y. B.; Li, Y. J.; Li, Y. L. Angew. Chem., Int. Ed. **2010**, *49*, 2705.

106 (a) Puodziukynaite, E.; Oberst, J. L.; Dyer, A. L.; Reynolds, J. R. J. Am. Chem. Soc. **2012**, 134, 968.

107 (a) Wang, L. Y.; Tsai, H. Y.; Lin, H. C. Macromolecules **2010**, *43*, 1277. (b) Cheng, K. W.; Mak, C. S. C.; Chan, W. K.; Ng, A. M. C.; Djurisic, A. B. J. Polym. Sci., Part A: Polym. Chem. **2008**, *46*, 1305.

108 Herrikhuyzen, V.; Herrikhuyzen, J. V.; George, S. J.; Vos, M. R. J.; Sommerdijk, A. J. M.; Ajayaghosh, A.; Meskers, S. C. J.; Schenning, A. P. H. J. Angew. Chem., Int. Ed. **2007**, *19*, 1825.

109 Xu, J.; Wang, J.; Mitchell, M.; Mukherjee, P.; Jeffries-EL, M.; Petrich, J. W.; Lin, Z. J. Am. Chem. Soc. **2007**, *129*, 12828.

110 Motaung, D. E.; Malgas, G. F.; Arendse, C. J. J. Mater. Sci. **2010**, *45*, 3276.

111 Koppe, M.; Scharber, M.; Brabec, C.; Duffy, W.; Heeney, M.; McCulloch, I. Adv. Funct. Mater. **2007**, *17*, 1371.

112 Li, K. C.; Huang, J. H.; Hsu, Y. C.; Huang, P. J.; Chu, C. W.; Lin, J. T.; Ho, K. C.; Wei, K. H.; Lin, H. C. Macromolecules **2009**, 42, 3681.

113 Lim, E.; Lee, S.; Lee, K. K. Chem. Commun. **2011**, 914.

114 Li, H.; Jiang, P.; Yi, C.; Li, C.; Liu, S. X.; Tan, S. T.; Zhao, B.; Braun, J.; Meier, W.; Wandlowski, T.; Decurtins, S. Macromolecules **2010**, 43, 8058.

115 Zhang, M.; Fan, H.; Guo, X.; He, Y.; Zhang, Z.; Min, J.; Zhang, J.; Zhao, G.; Zhan, X. W.; Li, Y. F. Macromolecules **2010**, 43, 5706.

116 Zou, Y.; Najari, A.; Berrouard, P.; Beaupre, S.; A?ch, B. R.; Tao, Y.; Leclerc, M. J. Am. Chem. Soc. **2010**, *132*, 5330.

117 Li, Y. F.; Zou, Y. P. Adv. Mater. **2008**, *20*, 2952.

118 Pokrop, R.; Pamu1a, K.; Drogomirecka, S. D.; Zagorska, M.; Borysiuk, J.; Reiss,

P.; Pron, A. J. Phys. Chem. C **2009**, *113*, 3487.

119 Lai, C. H.; Lee, W. F.; Wu, I. C.; Kang, C. C.; Chen, D. Y.; Chen, L. J.; Chou, P. T. J. Mater. Chem. **2009**, *19*, 7284.

120 Yoon, S. J.; Kim, J. H.; Kim, K. S.; Chung, J. W.; Heinrich, B.; F.; Mathevet, P. Kim,; Donnio, B.; Attias, A. J.; Kim, D.; Park, S. Y. *Adv. Funct. Mater.* **2012**, *22*, 61.

121 Barberá, J.; Godoy, M. A.; Hidalgo, P. I.; Parra, M. L.; Ulloa, J. A.; Vergara, J. M. *Liquid Crystals* **2011**, *38*, 679.

122 Rajan, Y. C.; Shellaiah, M.; Huang, C. T.; Lin, H. C.; Lin, H. C. *Tetrahedron* **2012**, *68*, 7926.

123 Steckler,T. T.; Zhang, X.; Hwang, J.; Honeyager, R.; Ohira, S.; Zhang, X. H.; Grant, A.; Ellinger, S.; Odom, S. A.; Sweat, D.; Tanner, D. B.; Rinzler, A. G.; Barlow, S.; Bredas, J. L.; Kippelen, B.; Marder, S. R.; Reynolds, J. R. *J. Am. Chem. Soc*. **2009**, *131*, 2824.

124 Chen, C. H.; Hsu, Y. C.; Chou, H. H.; Thomas, K. R. J.; Lin, J. T.; Hsu, C. P. *Chem. Eur. J*. **2010**, *16*, 3184.

125 Heredia, D.; Natera, J.; Gervaldo, M.; Otero, L.; Fungo, F.; Lin, C. Y.; Wong, K. T. *Org. Lett*. **2010**, *12*, 12.

126 Yang, H. Y.; Yen, Y. S.; Hsu, Y. C.; Chou, H. H.; Lin, J. T. *Org. Lett*. **2010**, *12*, 16.

127 Huang, J. H.; Ho, Z. Y.; Kekuda, D.; Chang, Y.; Chu, C. W.; Ho, K. C. *Nanotechnology* **2009**, *20*, 025202.

128 Ozturk, T.; Ertasb, E.; Mertc, O. *Tetrahedron* **2005** , *61*,11055-11077,

129 Qin, H.; Wenger, S.; Xu, M. F.; Gao, F. F.; Jing, X. Y.; Wang, P.; Zakeeruddin, S. M.; Grätzel, M. *J. Am. Chem. Soc*. **2008**, *130*, 9202.

130 Zhang, S. M.; Guo,Y. L.; Fan, H. J.; Liu, Y.; Chen, H. Y.; Yang, G.W.; Zhan, X. W.; Liu, Y. Q.; Li, Y. F.; Yang, Y. *J. Polymer Sci. Part A: Polymer Chem.* **2009**, *47*, 5498.

131 Li, K. C.; Huang, J. H.; Hsu, Y. C.; Huang, P. J.; Chu, C.W.; Lin, J. T.; Ho, K. C.; Wei, K. H.; Lin, H. C. *Macromolecules* **2009**, *42*, 3681.

132 Wang, L.; Chen, Q.; Pan, G. B.; Wan, L. J.; Zhang, S.; Zhan, X.; Northrop, B. H.; Stang, P. J. *J. Am. Chem. Soc*. **2008**, *130*, 13433.

133 Huo, L.; Hou, J.; Zhang, S.; Chen, H. Y.; Yang, Y. Angew. Chem. Int. Ed. **2010**, *8*, 1500.

134 Li, W. S.; Yamamoto, Y.; Fukushima, T.; Saeki, A.; Seki, S.; Tagawa, S.; Masunaga, H.; Sasaki, S.; Takata, M.; Aida, T. *J. Am. Chem. Soc*. **2008**, *130*, 8886.

135 Zhang, S. M.; Guo, Y. L.; Wang, L.; Li, Q. K.; Zheng, K.; Zhan, X. W.; Liu, Y. Q.; Liu, R. Q.; Wan, L. J. *J. Phys. Chem. C* **2009**, *113*, 16232-16237.

136 He, J. X.; Wu, W. J.; Hua, J. L.; Jiang, Y. H.; Qu, S. Y.; Li, J.; Long, Y. T.; Tian, H. *J. Mater. Chem*. **2011**, *21*, 6054.

137 Mann, J. R.; Gannon, M. K.; Fitzgibbons, T. C.; Detty, M. R.; Watson, D. F. *J. Phys. Chem. C* **2008**, *112*, 13057.

138 Chen, K. F.; Hsu, Y. C.; Wu, Q.; Yeh, M. C. P.; Sun, S. S. *Org. Lett*. **2009**, *11*, 377.

139 Baheti, A.; Tyagi, P.; Thomas, K. R. J.; Hsu, Y. C.; Lin, J. T. *J. Phys. Chem. C* **2009** , *113*, 8541.

140 Chaurasia, S.; Chen, Y. C.; Chou, H. H.; Wen, Y. S.; Lin, J. T. *Tetrahedron* **2012**, *68*, 7755.

141 Tian, H.; Yang, X.; Chen, R.; Zhang, R.; Hagfeldt, A.; Sun, L. J. Phys. Chem. C **2008**, *112*, 11023.

142 Lin, L. Y.; Tsai, C. H.; Lin, F.; Huang, T. W.; Chou, S. H.; Wu, C. C.; Wong, K. T. *Tetrahedron* **2012**, *68*, 7509.

143 Higashijima, S.; Miura, H.; Fujita, T.; Kubota, Y.; Funabiki, K.; Yoshida, T.; Matsui, M. *Tetrahedron*, **2011**, *34*, 6289.

144 Cho, N.; Choi, H.; Kim, D.; Song, K.; Kang, M. S.; Kang, S. O.; Ko, J. *Tetrahedron* **2009**, *31*, 6236.

145 Lu, G.; Usta, H.; Risko, C.; Wang, L.; Facchetti, A.; Ratner, M.; Marks, T. J. *J. Am. Chem. Soc*. **2008**, *130*, 7670.

146 Koppe, M.; Scharber, M.; Brabec, C.; Duffy, W.; Heeney, M.; McCulloch, I. *Adv. Funct. Mater*. **2007**, *17*, 1371.

147 Huang, C. Y.; Hsu, Y. C.; Chen, J. G.; Suryanarayanan, V.; Lee, K. M.; Ho, K. C. *Sol. Energy Mater. Sol. Cells*. **2006**, *90*, 2391.

148 Li, H.; Jiang, P.; Yi, C.; Li, C.; Liu, S. X.; Tan, S. T.; Zhao, B.; Braun, J.; Meier, W.; Wandlowski, T.; Decurtins, S. *Macromolecules* **2010**, *43*, 8058.

149 Zhang, M.; Fan, H.; Guo, X.; He, Y.; Zhang, Z.; Min, J.; Zhang, J.; Zhao, G.; Zhan, X. W.; Li, Y. F. Macromolecules **2010**, *43*, 5706.

Publication

1. Hsiao-Ping Fang, I-Hung Chiang, Chih-Wei Chu, Chang-Chung Yang, Hong-Cheu Lin* **"Applications of novel dithienothiophene- and 2,7-carbazole-based conjugated polymers with surface-modified ZnO nanoparticles for organic photovoltaic cells"**, *Thin Solid Films* **2011**, 519, 5212-5218.

2. Hsiao-Ping Fang, Jia-Wei Lin, I-Hung Chiang, Chih-Wei Chu, Kung-Hwa Wei, Hong-Cheu Lin. **" Synthesis of Novel Dithienothiophene- and 2,7-Carbazole-Based Conjugated Polymers and H-Bonded Effects on Electrochromic and Photovoltaic Properties"** *J. of Polymer Sci. Part A: Polymer Chem.* **2012**, 50, 5011-5022.
3. Hsiao-Ping Fang, Yen-Hsing Wu, and Hong-Cheu Lin **" Synthesis and study of novel supramolecular nanocomposites containing aryl-imidazo-phenanthroline-based metallo-polymers (H-donors) and surface-modified ZnO nanoparticles (H-acceptors) "** *Tetrahedron* **2013,** 69, 293-301.
4. Muthaiah Shellaiah, Hsiao-Ping Fang, Ying-Ling Lin,Ying-Chan Hsu, Jiann-T'suen Lin, and Hong-Cheu Lin **"Synthesis of Metal-Free Organic Dyes Containing Tris(dodecyloxy)phenyl and Dithienothiophenyl Units and a Study of Their Mesomorphic and Photovoltaic Properties"** *Tetrahedron* **2012,** in press.